EFFECTS OF Ca AND Ce ON THE MICROSTRUCTURE AND MECHANICAL PROPERTIES OF Mg-Zn ALLOYS

by

Brian Langelier

A thesis
presented to the University of Waterloo
in fulfilment of the
thesis requirement for the degree of
Doctor of Philosophy
in
Mechanical Engineering

Waterloo, Ontario, Canada, 2013

Author's Declaration

I hereby declare that I am the sole author of this thesis. This is a true copy of the thesis, including any required final revisions, as accepted by my examiners. I understand that my thesis may be made electronically available to the public.

Abstract

The effects of Ca and Ce on the precipitation behaviour and microstructural characteristics of Mg-Zn based alloys are investigated by comprehensive multi-scale characterization and analysis. The elements Ca and Ce are chosen for their potential to enhance (a) precipitation hardening and (b) alloy texture and ductility, and are examined at both alloying and microalloying (< 0.5 wt%) levels. When added individually to Mg-Zn, Ca is found to enhance precipitation, but Ce produces a generally adverse effect on the hardening response. A pre-ageing strategy is proposed to alleviate this negative effect of Ce. The highlight of this work is the double microalloying addition of Ce-Ca to Mg-Zn, as this combination and quantity proves to be the most effective at increasing the age-hardening response, and enhancing microstructural characteristics for improved ductility. Transmission electron microscopy analysis reveals the hardening increase to originate from a refined precipitate microstructure, and the formation of fine-scale basal plate precipitates. These fine precipitates form during early ageing as monolayer GP zones consisting of Ca and Zn. The formation of these GP zones is facilitated by the atomic size difference between those two solutes, and their observed tendency to co-cluster. The monolayer GP zones evolve to multi-layered forms in the peak-aged condition. These precipitates are observed to be uniformly distributed, even where apparent precipitate-free zones are observed for the Mg-Zn type phases in the grain boundary regions. Notably, the size of these precipitate-free zones for the Mg-Zn phases is also reduced in the Ce-Ca microalloyed samples, compared to the binary alloy. The Ce-Ca microalloying additions also promote grain refinement and a weakening of the basal textures, typical of conventional Mg-based alloys, compared to both Mg-Zn and Mg-Zn-Ce. As a result, the tensile behaviour of the alloys with Ce-Ca is similarly enhanced. Considering both the precipitation hardening capability and microstructural characteristics, it is concluded that the double microalloying additions of Ce-Ca can be considered as a new alloy design strategy to successfully achieve improvement in both the strength and ductility of Mg-Zn alloys.

Acknowledgements

I would like to acknowledge and sincerely thank the numerous people whose contributions of time, effort, and expertise made it possible to accomplish this work.

First and foremost I would like to thank my supervisor, Dr. Shahrzad Esmaeili, for her guidance, assistance, and support, both professionally and personally over the past several years, and during this research effort.

I would also like to gratefully acknowledge my direct collaborators: Dr. Gang Sha, Dr. Patricia Donnadieu, Dr. Xiang Wang, Dr. Simon Ringer, Ghazal Nayyeri, Dr. Michael Gharghouri, and Dr. Soo Yeol Lee for their invaluable contributions to this work.

This work would also not be possible without assistance from many other researchers, as well as countless technical and research staff. In particular, I would like to thank Dr. Yuquan Ding, Dr. Lin Xiao, Mark Griffett, Norval Wilhelm, Masroor Hasan, Dr. Warren Poole, Dr. Mary Wells, Debbie Burgess, Martin Van Oosten, Dr. Hatem Zurob, Jim Garrett, Dr. Xiaogang Li, Dr. Andreas Korinek, Wen He Gong, Dr. Carmen Andrei, Fred Pearson, Dr. Ross Marceau, Dr. Aimen Gheribi, and Dr. Youn-Bae Kang. I would also like to thank the rest of the staff and researchers at the University of Waterloo, McMaster University, the Canadian Centre for Electron Microscopy, the Australian Centre for Microscopy and Microanalysis, and CNRS-Grenoble, for their assistance.

I would also like to acknowledge the financial support of this work from the Natural Sciences and Engineering Research Council of Canada in the Framework of Strategic Magnesium Network Program (MagNET).

I would also like to thank my fellow researchers for their many discussions and which have helped me with this work, including Panthea Sepehrband, Li Hua Liao, Vahid Fallah, Nasim Bakhshi Zadeh, Dan Cluff, Phil Tomlinson, and Liam Huber.

I would like to thank all my friends and family for being always being there for me. In particular, I owe special thanks to my close friends Brock Watson, Peter Christensen, Jill Redman, Jason Fice, Derrick Hambly, Ryan George, Malwina Mencel, Farnoud Kazem-Zadeh, Niki Kazem-Zadeh, Scott Stirling, and most of all Leia Lane. Finally, but most importantly, I would like to thank my family, and especially my parents - I dedicate this work to you.

Table of Contents

Author's Declaration ii

Abstract iii

Acknowledgements iv

Table of Contents v

List of Tables ix

List of Figures x

1 Introduction 1

- 1.1 General Properties and Application of Magnesium Alloys 1
- 1.2 Strength and Precipitation Hardening of Magnesium Alloys 2
- 1.3 Deformation and Texture of Magnesium Alloys 4
- 1.4 Objectives and Scope 7

2 Literature Review 10

- 2.1 General Precipitation Hardening in Magnesium Alloys 10
- 2.2 Precipitation Hardening of Binary Mg-Zn Alloys 16
- 2.3 Precipitation Hardening of Mg-Zn-Ca Alloys 21
- 2.4 Precipitation Hardening of Mg-Zn-Ce Alloys 27
- 2.5 Effect of Ce and Ca Additions on the Ductility and Texture of Magnesium Alloys 29
- 2.6 Summary 32

3 General Methodology 34

- 3.1 Material Preparation 34
- 3.2 Thermal-Mechanical Processing 36

3.3 Mechanical Testing 38

3.3.1 Hardness Testing 38

3.3.2 Tensile Testing 38

3.4 Microscopy & Microstructure Characterization 39

3.4.1 Optical Microscopy 39

3.4.2 Scanning Electron Microscopy 39

3.4.3 Transmission Electron Microscopy 40

3.4.4 Electron Backscatter Diffraction 41

3.4.5 Neutron Diffraction 42

3.4.6 Atom Probe Tomography 42

3.5 Calorimetry 43

3.6 Thermodynamic Calculations 43

3.7 Acknowledgement of Assistance with Experiments 44

4 Precipitation and Phase Evolution in Mg-Zn-Ca Alloys with High-Ca Content 45

4.1 Introduction 45

4.2 Experimental Methodology 46

4.3 Results and Discussion 46

4.3.1 Isothermal Ageing of XZ21 and XZ22 Alloys 46

4.3.2 Experimental Analysis of Precipitate Evolution in XZ21 49

4.3.3 De-Convolution of DSC Data for Precipitate Evolution in XZ21 55

4.4 Summary 59

5 Effects of Ce Additions on the Precipitation Hardening of Mg-Zn Alloys 60

5.1 Introduction 60

5.2 Experimental Methodology 61

5.3 Results 61

5.4 Discussion 67

5.5 Summary 75

6 Precipitation Hardening of Mg-Zn Alloys with Ce-Ca Microalloying Additions 76

6.1 Introduction 76

6.2 Experimental Methodology 77

6.3 Results and Discussion 78

6.3.1 Precipitation Hardening Behaviour 78

6.3.2 Peak-Aged Microstructure Of The ZEX400 Alloy 81

6.3.3 Precipitates in the ZEX400 Alloy 88

6.3.4 Precipitation Sequence in the ZEX400 Alloy 101

6.4 Summary 111

7 Evaluation of Grain Boundary Precipitation and Solute Segregation in an Mg-Zn Alloy with Ce-Ca Microalloying Element Additions 114

7.1 Introduction 114

7.2 Experimental Methodology 115

7.3 Results 116

7.4 Discussion 123

7.5 Summary 127

8 Improving Microstructure and Mechanical Properties of Mg-Zn Alloys by Ce-Ca Microalloying Element Additions 129

8.1 Introduction 129

8.2 Experimental Methodology 131

8.3 Results 132

8.3.1 Microstructure 132

8.3.2 Mechanical Properties 143

8.4 Discussion 145

8.5 Summary 157

9 Conclusions, and Recommendations for Future Work 159

9.1 Conclusions 159

9.2 Recommendations for Future Work 162

References 165

List of Tables

Table 2-1: Precipitate phases and precipitation sequences at various ageing temperatures for Mg-2.8Zn (at%), as reported by Buha [18]. All directions and planes are given with respect to the HCP-Mg lattice....................................... 19

Table 2-2: Summary of reported precipitates in Mg-Zn-Ca alloys. Note: SADP analysis included as TEM.. 25

Table 3-1: Compositions of experimental alloys, in wt% (at%)... 35

Table 3-2: Homogenizing, rolling/annealing, and solutionizing heat treatment parameters for experimental alloys... 37

Table 6-1: List of experimental alloys investigated and test conducted related to chapter 6. 78

Table 6-2: Composition data for the APT results shown in Figure 6-5.................................. 89

Table 6-3: Cluster composition data calculated from the APT results shown in Figure 6-13.. 102

Table 7-1: Calculated element concentrations in the APT analysis volume, and resultant Gibbs interfacial excess values.. 122

Table 7-2: Solute supersaturation levels in HCP-Mg for ZEX400, calculated according to methodology described in section 3.6.. 124

Table 8-1: List of experimental alloys investigated and test conducted related to chapter 8. 132

Table 8-2: Tensile properties of experimental alloys obtained from tensile test results......... 144

Table 8-3: Comparison of ZEX200 and ZEX400 alloy ductility and precipitation hardening ability during 180°C ageing.. 157

List of Figures

Figure 1-1: Schematic showing the major deformation systems in magnesium alloys. A) basal, prismatic, and pyramidal slip with an ⟨a⟩ Burgers vector, b) second-order pyramidal ⟨c + a⟩ slip, c) $\{10\bar{1}2\}\langle 10\bar{1}1\rangle$ extension twinning, d) $\{10\bar{1}1\}\langle 10\bar{1}2\rangle$ compression twinning. 5

Figure 1-2: Schematic of typical texture for magnesium alloys showing alignment of the [0001] direction following a) rolling, b) extrusion. 6

Figure 2-1: Schematic showing basal plate precipitates and c-axis rods as seen along the basal $[0001]$ and prismatic $\langle 10\bar{1}0\rangle$ or $\langle 11\bar{2}0\rangle$ planes. 11

Figure 2-2: Effective inter-particle spacing vs. Number density for different precipitate morphologies. Values are per unit volume of Mg, given a set precipitate volume fraction of 0.04, and an aspect ratio of 40:1 for rods and plates (from Nie [81]). 12

Figure 2-3: Calculated Orowan stress required to bypass different precipitate types for a) basal and b) prismatic slip, for a particle volume fraction of 5%, and an aspect ratio of 0.1 for plates and 10 for rods (from Robson et al. [82]). 13

Figure 2-4: Schematic showing orientation of a) basal plate b) c-axis rod c) prismatic plate precipitates in twinned material, and d) calculated Orowan stress inhibiting basal slip for the different precipitate types within the twin, calculated for a particle volume fraction of 5%, and an aspect ratio of 0.1 for plates and 10 for rods (from Robson et al. [82]). 14

Figure 2-5: TEM micrographs for Mg-8Zn (wt%) aged 2 h at 200°C showing mgzn' precipitate rods and plates. Electron beam parallel to a) $\langle 10\bar{1}0\rangle$, and b) $[0001]$ (from Gao and Nie [42]). 17

Figure 2-6: Schematic of precipitates in Mg-4Zn (wt%) aged 10^4 ks at 450 K (from Bettles et al. [41]). 18

Figure 2-7: TEM image showing grain boundary precipitate and precipitate-free zone for an Mg-5Zn (wt%) alloy aged 6 h at 260°C, x12000 magnification (from Clark [20]). 20

Figure 2-8: Schematic of the ordered GP zone structure formed along a single basal plane of the HCP-Mg lattice, reproduced based on the descriptions of Ping et al. [97] (for solute of RE/Zn) and Oh-ishi et al. [53] (for solute of Ca/Zn). Shaded area shows hexagonal cell of GP zone formed by solutes........... 22

Figure 2-9: Model of the $Mg_6Ca_2Zn_3$ equilibrium phase, as described by Jardim et al. [100], showing a) the unit cell, and additionally from b) $[0001]$, c) $\langle 11\bar{2}0\rangle$, and d) $\langle 10\bar{1}0\rangle$ directions. Note that directions correspond to the $Mg_6Ca_2Zn_3$ phase, and not its orientation within the HCP-Mg matrix. 24

Figure 4-1: Isothermal age-hardening curves for Mg-Zn-Ca alloys aged at 200°C. 47

Figure 4-2: TEM micrographs of a) X2 b) XZ21 aged isothermally at 220°C for 1 hour. Electron beam parallel to $\langle 11\bar{2}0\rangle$ zone axis. Observations performed by V.Y. Gertsman [132]. 47

Figure 4-3: Factsage [127] isopleth phase diagram for Mg-Zn with constant 2wt% Ca........... 48

Figure 4-4: Hardness evolution during non-isothermal ageing at 0.5°C/min and DSC results for as-quenched XZ21 alloy. 50

Figure 4-5: TEM image of XZ21 alloy non-isothermally aged to 250°C with corresponding sadps along a) $\langle 10\bar{1}0\rangle$ zone axis, b) $\langle 11\bar{2}0\rangle$ zone axis, and c) TEM image of large plate precipitates d) large blocky precipitates with sadps $\langle 11\bar{2}0\rangle$ zone axes. Observations performed by X. Wang.. 52

Figure 4-6: TEM images of XZ21 alloy non-isothermally aged to 300°C with corresponding sadps along a) $\langle 10\bar{1}0\rangle$ zone axis, b) $\langle 11\bar{2}0\rangle$ zone axis, and c) $\langle 10\bar{1}0\rangle$ zone axis. Observations performed by X. Wang. 53

Figure 4-7: Calculated equilibrium secondary phase content for XZ21 alloy 55

Figure 4-8: DSC results for XZ21 alloy given a high-temperature ageing heat treatment, and the results of subtracting this data from the as-quenched DSC trace. DSC result for the binary X2 alloy is also presented for comparison. Note that curves are shifted along y-axis for ease of visualization, and axis values are given only for the purpose of scale. 57

Figure 5-1: Age-hardening responses of Mg-Zn-(Ce) alloys aged at 100°C with a) 2 wt% Zn, and b) 4 wt% Zn.. 63

Figure 5-2: Bright-field TEM micrographs of a,b) Z4, c,d) ZE40, and e,f) ZE41 alloys aged 168 h at 100°C, a,c,e) [0001] zone axis, b,d,f) near $\langle 11\bar{2}0\rangle$ zone axis, with [0001] direction indicated on the images. Precipitates identified with numbers assigned in the text... 64

Figure 5-3: Bright field TEM micrographs showing large particles in a) ZE40 and d) ZE41 aged 168 h at 100°C, and corresponding EDS spectra for the matrix and particles in the ZE40 (b, c) and ZE41 (e, f) alloys.. 66

Figure 5-4: Calculated supersaturations in mol fraction for solute elements in HCP-Mg at 100°C, and ageing responses for 168 h ageing at 100°C for Mg-Zn-(Ce) alloys. 68

Figure 5-5: a) Bright field TEM image and b) low-magnification STEM image of ZE20 alloy pre-aged 3 h at 300°C, showing small precipitates on basal planes, with EDS spectra for the c) matrix and d) precipitates. e) fine precipitates in ZE20 alloy pre-aged, then artificially aged 168 h at 100°C. All micrographs from [0001] zone axis. 72

Figure 6-1: a) Hardness evolution and b) hardening response for Mg-Zn-(Ce)-(Ca) alloys aged at 180°C. 79

Figure 6-2: a,b,c) TEM micrographs of peak-aged ZEX400 (aged 168h at 180°C), a) [0001] b) $\langle 11\bar{2}0 \rangle$, c) $\langle 10\bar{1}0 \rangle$ zone axes, with precipitates marked as indicated in the text. D,e) $\langle 10\bar{1}0 \rangle$ matrix zone axis SADP for d) c-axis rods (precipitate 1), and e) large basal plates (precipitate 2). Observations for a, b, performed by P. Donnadieu. 83-84

Figure 6-3: a) Bright-field TEM image, $\langle 10\bar{1}0 \rangle$ zone axis, and b) HAADF-STEM image, $\langle 11\bar{2}0 \rangle$ zone axis showing overview of precipitate microstructure in peak-aged ZEX400 alloy (aged 168h at 180°C), with precipitates marked as indicated in the text. 85

Figure 6-5: APT reconstructed atom map for ZEX400 aged 96 h at 180°C showing c-axis rod precipitates passing through the analysis volume, with a) Mg and Zn solute showing (Zn iso-concentration surfaces on precipitates), b) Ce and Ca solute, c) 1-D concentration profile through a precipitate. APT reconstruction performed by G. Sha. 90

Figure 6-6: Bright-field TEM micrograph of ZEX400 alloy aged 3h at 180°C, $\langle 10\bar{1}0\rangle$ zone axis, with streaking in SADP insert. 91

Figure 6-7: HAADF-STEM images of ZEX400 aged 3 h at 180°C showing monolayer GP zones with corresponding FFT inserts from a) $\langle 11\bar{2}0\rangle$ b)$\langle 10\bar{1}0\rangle$ zone axis, and c) Fourier-filtered image of monolayer GP zone shown in b). 92-93

Figure 6-8: HAADF-STEM image showing a multi-layer and monolayer GP zone with corresponding FFT inserts, in ZEX400 aged 3 h at 180°C, $\langle 10\bar{1}0\rangle$ zone axis. 94

Figure 6-9: HR-TEM images of ZEX400 aged 3 h at 180°C showing i) monolayer GP zones and ii) multi-layer precipitates, with corresponding FFT inserts from a) $\langle 11\bar{2}0\rangle$ b) $\langle 10\bar{1}0\rangle$ zone axis. 96

Figure 6-10: a) HR-TEM image and b) HAADF-STEM image of fine basal precipitates in peak-aged ZEX400 (aged 168 h at 180°C) from $\langle 11\bar{2}0\rangle$ zone axis 97

Figure 6-11: HAADF-STEM image of multi-layer basal precipitates in ZEX400 a) aged 3 h at 180°C from $\langle 10\bar{1}0\rangle$ zone axis, and b) aged 168 h at 180°C from $\langle 11\bar{2}0\rangle$ zone axis, showing dark bands parallel to the basal planes. 98

Figure 6-12: Faint monolayer GP zone (indicated by arrows) next to a growing multi-layer precipitate in ZEX400 aged 3 h at 180°C, $\langle 10\bar{1}0\rangle$ zone axis. 99

Figure 6-13: APT results for ZEX400 alloy aged 168 h at 100°C, showing atom maps for a) Zn, b) Ca, and the results of clustering calculations for c) Zn-rich clusters, d) Ca-Zn clusters. APT reconstruction and analysis performed by G. Sha. 101

Figure 6-14: Bright-field TEM micrographs of ZEX200 alloy a) aged 3 h 180°C, $\langle 11\bar{2}0\rangle$ zone axis, b) aged 168 h 180°C, $\langle 10\bar{1}0\rangle$ zone axis, with streaking apparent in the SADP inserts. Observations performed by P. Donnadieu. 104

Figure 6-15: DSC curves for ZEX200, ZEX400, and ZE40 alloys a) in the as-quenched condition, b) after 3 h ageing at 180°C, c) after 168 h ageing at 180°C, exothermic peaks for ZEX400 alloy are labeled according to their descriptions in the text. c) also includes the results of subtracting the ZE40 result from the ZEX400 trace, as described in the text. 105

Figure 6-16: DSC results for the as-quenched ZEX200 alloy, and the XZ21 alloy aged 24 h at 370°C. 109

Figure 7-1: a-d) Bright-field TEM micrographs of ZEX400 alloy aged 168h at 180°C a) $\langle 10\bar{1}0\rangle$ zone axis showing general precipitate microstructure, b) grain boundary with apparent PFZ, c) $\langle 11\bar{2}0\rangle$ zone axis image showing fine basal precipitates adjacent to a grain boundary, d) PFZ and grain boundary precipitates. Precipitates are marked with numbers as listed in the text. EDS spectra for e) a grain boundary precipitate and f) the matrix, correspond to the locations identified in d). Observations for b,c performed by P. Donnadieu. 117

Figure 7-2: HAADF-STEM images comparing a) ZEX400 and b) Z4 alloys aged 168 h at 180°C, $\langle 11\bar{2}0\rangle$ zone axis, with details of grain boundaries and PFZ presented in c) ZEX400 and d) Z4. 118

Figure 7-3: a) APT solute distributions for Zn in ZEX400 alloy, aged 168h at 100°C showing a grain boundary with Zn segregation (indicated by arrows). B) Detector desorption maps for different sections of the APT volume, showing indexed pole figures for each grain with the grain boundary indicated by a dashed line. c) Ce and Ca atom maps, d) Ca-containing solute clusters. APT reconstruction and analysis performed by G. Sha. 120

Figure 7-4: Solute concentration profiles normal to the grain boundary from APT analysis. Zn depleted zones are estimated based on points of inflection adjacent to the grain boundary........ 121

Figure 7-5: Bright-field TEM image of ZEX400 alloy aged 3 h at 180°C showing fine basal plates adjacent to the grain boundary, and small grain boundary precipitates, $\langle 10\bar{1}0\rangle$ zone axis. 124

Figure 8-1: Optical micrographs of experimental alloys in the rolling plane. 133

Figure 8-2: Average grain diameters for experimental alloys, taken from measurements in the rolling plane. 134

Figure 8-3: SEM backscatter images showing secondary phases for ZE20, ZE40, ZEX200, and ZEX400 alloys, and corresponding EDS spectra for select secondary phase particles, as well as the matrix phase. Low-magnification images show particle distributions in ZEX200, ZEX400. View is normal to the sheet plane of the rolled material. 135

Figure 8-4: Bright field TEM micrographs for a) ZEX200 alloy showing: (1) large particles, (2) medium-sized particles (2*) medium-sized particles at grain boundaries, (3) fine particles, b) ZE20 alloy, c) ZEX200 alloy. EDS spectra are also presented which correspond to the precipitates and matrices shown in b) and c). 137

Figure 8-5: Inverse pole figure maps of Z2, ZE20, ZEX200, ZE40, ZEX400 along the rolling plane, measured by EBSD. Analysis performed by G. Nayyeri. 139

Figure 8-6: Basal pole intensities in the normal direction, as measured by EBSD. Analysis performed by G. Nayyeri. 140

Figure 8-7: Pole figures obtained by neutron diffraction measurement for rolled and annealed a,b) Z2, c,d) ZE20, e,f) ZEX200, g,h) ZE40, and i,j) ZEX400 for a,c,e,g,i) basal, and b,d,f,h,j) prismatic poles. Contour lines represent multiples of a random distribution (MRD), as indicated for each pole figure. Bold contour lines are equal to 1 MRD. The rolling direction (RD) and transverse direction (TD) are labelled on the pole figures. Neutron diffraction measurements performed by S.Y. Lee and M. Gharghouri. 142

Figure 8-8: Typical engineering stress-strain curves obtained by tensile testing for a) 2 wt% Zn based alloys, b) 4 wt% Zn based alloys. 143

Figure 8-9: Equilibrium solute element concentration profiles for the experimental alloys from 400°C to 100°C for a) Zn, b) Ce and Ca in HCP-Mg, calculated using Factsage [127]. Note the logarithmic scale for b). 146

Figure 8-10: Equilibrium secondary phase profiles for experimental alloys from 400°C to 100°C, calculated using Factsage [127]. The plots are generated for the equilibrium phases of a) $Mg_6Ca_2Zn_3$, b) mgznce-type phases, c) $Mg_{12}Zn_{13}$. 147

Figure 8-11: Calculated phase fractions at the homogenizing temperature of 400°C (mol%) and particle area fractions measured by SEM imaging of annealed alloys. 152

Figure 8-12: SEM secondary-electron micrographs showing the fracture surfaces of a,b) Z2, c,d) ZEX200, e,f) ZEX400 alloys following tensile testing. Micro-cracks in a) and e) are indicated by arrows. The arrows in f) show secondary phase particles at micro-void sites in ZEX400. 155

1 Introduction

1.1 General Properties and Application of Magnesium Alloys

The current global issues of increasing energy costs and public interest in environmental stewardship have affected the manufacturing world. This can be clearly seen in the automotive industry, where consumer and regulatory demand has led to renewed interest in the development and production of vehicles with improved fuel efficiency [1].

The plans to increase fuel efficiency in vehicles are numerous and varied. A simple, yet very effective technique to increase fuel efficiency is to reduce vehicle mass [1,2]. This may be achieved by switching to materials with lower density and comparable specific strength, such as aluminum and magnesium. Magnesium is an attractive choice as a lightweight material as it is less dense than aluminum, less expensive than titanium, and has the advantage of recyclability over many composites and thermosetting polymers [3–7]. Magnesium is currently utilized mainly in large, cast parts such as engine blocks and cradles [3,8–10].

Although the low density and high availability of magnesium make it a desirable choice for many automotive applications, it has several drawbacks. Magnesium generally exhibits very low corrosion resistance, and the potential for flammability [3,10–12]. However, these problems can generally be dealt with by selecting proper coatings and alloying elements, provided extreme service conditions are avoided. Of greater limitation to the application of magnesium alloys are their relatively low strength and poor ductility [8,10,13,14]. To fully utilize the potential of magnesium alloys in the automotive industry, it is necessary that these issues be resolved. A promising method for improving magnesium alloy strength is by precipitation hardening; although the development of a significant precipitation hardening effect is also not without its challenges. Magnesium alloy strength, as well as how it can be improved by precipitation hardening, and the deformation and texture characteristics of wrought magnesium which result in its low ductility, are further explored in the following sections.

1.2 Strength and Precipitation Hardening of Magnesium Alloys

While the density of magnesium is very low, its strength is still generally less than that of other lightweight alloys such as aluminum. Many magnesium alloys therefore have lower strength-to-weight ratios than common aluminum alloys [3]. Reliable strengthening by grain-refinement can be difficult to achieve due to the relatively high temperatures used during rolling and extrusion of wrought magnesium. The use of higher temperatures for processing is necessitated by the low ductility of wrought magnesium at room temperature, but it can also lead to significant dynamic recrystallization and grain growth [13]. An alternate and effective way to improve strength is by precipitation hardening, which can be achieved by alloying magnesium with a proper combination of elements.

Precipitation hardening occurs as a result of a diffusional transformation in the solid state. This transformation originates in systems where the solid solubility of one or more alloying elements is sufficiently increased with elevated temperature. This difference in solid solubility with temperature allows for a high amount of solute to be dissolved into solid solution (solutionized) during a high temperature heat treatment, which can then precipitate from solution at lower temperatures (i.e. during ageing). If the sample can be quickly quenched from the solutionizing temperature, the matrix composition at that temperature can be mostly preserved, which produces a metastable supersaturated solid solution. The free energy of the supersaturated solid solution is higher than the equilibrium multi-phase mixture; therefore, the decomposition of the supersaturated matrix via the precipitation transformation is thermodynamically-favourable. This transformation proceeds by removing solutes from solution and forming precipitate particles. If these precipitates can effectively hinder the motion of dislocations in the material to a greater degree than when their component solutes are present in solution, then the alloy will be strengthened.

There are a number of magnesium alloy systems which exhibit the potential for precipitation, including (but not limited to): Mg-Al, Mg-Ca, Mg-Gd, Mg-Nd, Mg-Sn, Mg-Y, and Mg-Zn. Some of the most studied precipitation systems in magnesium are the Mg-Al, Mg-Zn and alloys of magnesium with rare earth (RE) elements, i.e. Mg-RE systems [15–24]. There are several commercially available magnesium alloys that are precipitation hardenable, such as AZ91 (Mg-9Al-1Zn wt%), ZK60 (Mg-6Zn-0.5Zr wt%), and WE43 (Mg-4Y-3RE wt%) alloys [15,24,25]. However, the precipitation hardening responses of commonly available magnesium alloys are notably lower compared to heat-treatable aluminum alloys (ie. in 2xxx [26,27] 6xxx [28–32] and 7xxx [33–36] alloys). These relatively poor age hardening responses, compared to aluminum, have mainly been attributed to the orientation characteristics and low number densities of precipitates in the magnesium alloys. The overall effect of precipitate orientation on hardening is still being investigated as new research results are obtained. However, the significance of precipitate number density on hardening is widely-accepted.

Improving the precipitation behaviour of binary magnesium alloy systems can be done by alloying or microalloying (additions of < 0.5 wt%) with one or more additional elements. It has been found that the small amount of additional elements has the potential to result in large scale effects on the hardening of an alloy. Generally, this increase in the hardening response is achieved by the microalloying additions promoting a finer and more uniform distribution of precipitates [37–40], but in some cases microalloying additions are reported to alter the types of precipitates that form as well [37,41]. Therefore, the continued development of precipitation hardening magnesium alloys through proper design of alloy chemistry and selection of alloying/microalloying elements has the potential to improve the relatively low hardening response exhibited by current alloys.

Among precipitation hardening magnesium alloys, the Mg-Zn system shows a significant hardening response and high potential for alloy development [19,20,42]. However, as noted by Clark [20], the number density of the precipitates which form in binary Mg-Zn alloys still tends to be low, which limits the amount of hardening. Therefore, a refinement of the precipitate microstructure by proper alloying/microalloying addition may result in an increased age hardening response for Mg-Zn based alloys. The precipitation hardening response in Mg-Zn alloys has been reported to be successfully enhanced using several different microalloying additions, such as Ag [43], Ba [37], Co [44], Cr [45], Cu [46–48], Ti [49,50], V [51], and Ca [40,41,52,53]. Ca is of particular interest as an alloying/microalloying addition to Mg-Zn, as Ca additions can potentially provide many benefits to magnesium alloys. These include a significant reduction in flammability and improvement in the oxidation and creep resistance, as well as grain refinement and biocompatibility [11,54–59]. This work will therefore examine modifications to the Mg-Zn system by microalloying to enhance the precipitation hardening response, with particular focus on additions of Ca.

1.3 Deformation and Texture of Magnesium Alloys

Magnesium alloys typically exhibit relatively poor ductility compared to other engineering alloys such as Al or steel. This is primarily the result of its hexagonal-close-packed (HCP) crystal structure. In magnesium grains, deformation occurs primarily by dislocations of a $1/3\langle 11\bar{2}0\rangle$ Burgers vector along the (0001) basal plane [60–62]. This provides two independent slip systems, which is fewer than the five required by the Taylor criterion for general homogeneous plasticity of a polycrystal of uniform density [61,63]. Furthermore, basal slip only allows for slip with $\langle a\rangle$, i.e. $\langle 11\bar{2}0\rangle$, direction components [61]. At higher critical resolved shear stress (CRSS), $\langle a\rangle$ slip can also be activated on the prismatic $\{10\bar{1}0\}$ and pyramidal $\{10\bar{1}1\}$ planes [61,62]. Dislocation movement along these planes provides two and four additional independent slip systems, respectively, which would fulfill the requirement of five independent slip systems [61]. However, while prismatic slip has been reported at room temperature [61,62], pyramidal slip is generally more difficult to activate. Second-order pyramidal slip on $\{11\bar{2}2\}$ planes could also provide additional ductility, as well as slip with a $\langle c+a\rangle$ Burgers vector. This slip system has been attributed to the increased formability of magnesium alloys at elevated temperatures, but again remains difficult to activate at room temperature for common magnesium alloys [61]. A schematic of the slip systems mentioned is provided in Figure 1-1.

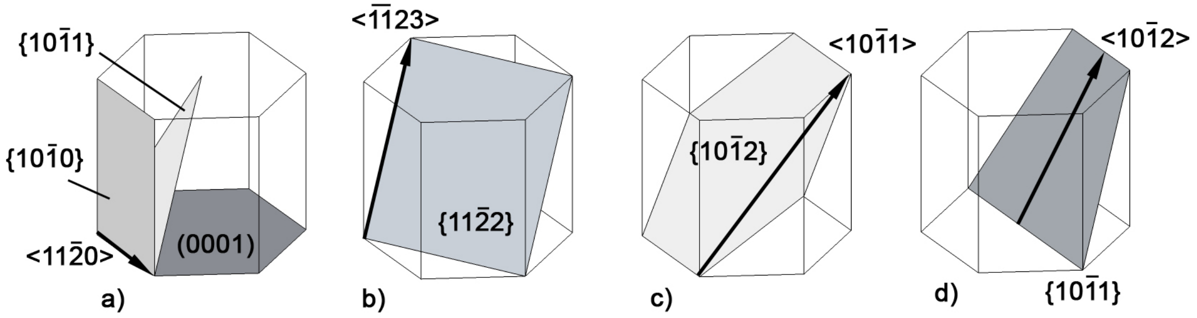

Figure 1-1: Schematic showing the major deformation systems in magnesium alloys. a) basal, prismatic, and pyramidal slip with an $\langle a\rangle$ Burgers vector, b) second-order pyramidal $\langle c+a\rangle$ slip, c) $\{10\bar{1}2\}\langle 10\bar{1}1\rangle$ extension twinning, d) $\{10\bar{1}1\}\langle 10\bar{1}2\rangle$ compression twinning.

The main contributor to non-dislocation deformation in magnesium is twinning [61,62,64,65]. Twinning is the second most readily activated deformation mechanism in Mg. This is most pronounced in large-grained magnesium [60]. Twinning also helps give rise to tension-compression yield anisotropy in magnesium [64,66]. The most common twin to form in magnesium during deformation is the $\{10\bar{1}2\}\langle 10\bar{1}1\rangle$ extension twin, so named as it provides extension along the $\langle c\rangle$ axis [64]. This twinning system can lead to a ductility increase in magnesium; however, the available strain from twinning is finite. Certain twins can also accommodate compression along the $\langle c\rangle$ axis, particularly the $\{10\bar{1}1\}\langle 10\bar{1}2\rangle$ compression twin or $\{10\bar{1}1\}-\{10\bar{1}2\}$ double-twinning [65]. However, activation of these twins can promote micro-cracking and failure, and is considered to be a main contributor to the near-brittle behaviour of magnesium alloys [60,62,65]. The extension and compression twins are also shown schematically in Figure 1-1.

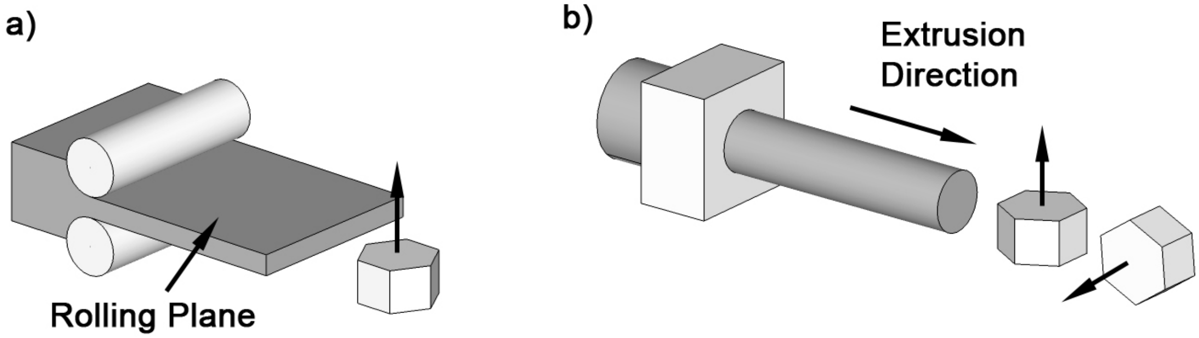

Figure 1-2: Schematic of typical texture for magnesium alloys showing alignment of the [0001] direction following a) rolling, b) extrusion.

For wrought magnesium alloys, their already poor ductility can be exacerbated by strong textures which tend to form following bulk deformation processes (i.e. rolling, extrusion). These textures result in grains generally oriented with the basal pole either normal to the sheet plane in rolling, or normal to the extrusion direction, (shown schematically in Figure 1-2) and arise as a consequence of the predominance of basal slip [67]. This strong basal texture formation in magnesium alloys, when combined with the limited slip and deformation modes, can result in very poor formability for wrought magnesium sheet or extrusions.

There is currently a very high interest in improving the ductility of wrought magnesium by reducing the strength of the basal textures [14], which can be achieved through the addition of RE elements [14,68–73]. The mechanisms by which the RE elements modify the texture are still the subject of much research, but it is noted that most RE elements examined can achieve this effect. However, the RE elements with lower solid solubility in Mg, such as La and Ce, are found to be the most potent at modifying texture, as they produce such an effect even when added in very low amounts (i.e. microalloying levels) [69,70]. Of these, Ce is of particular interest for practical magnesium alloy development due to its relative abundance and low cost (for a RE element) combined with its potency at achieving a weakened texture [73,74].

Considering the common benefit from alloying/microalloying on the precipitation hardening effect (as mentioned previously), and on alloy texture (when using RE elements), it stands that alloy design strategies may be able to achieve both of these improvements in properties simultaneously.

1.4 Objectives and Scope

The objectives of the this research are to (a) study the basic precipitation hardening characteristics of selected Mg-(Zn)-(Ca) based alloys, (b) develop practical magnesium alloys with improved strength and ductility by alloying/microalloying of the Mg-Zn system with Ce and Ca, and (c) to gain understanding of the mechanisms by which these alloying/microalloying additions act to alter the microstructure and enhance these properties. The current research advances the understanding of precipitation hardening in the Mg-Zn-Ca, Mg-Zn-Ce, and Mg-Zn-Ce-Ca systems, while also examining the efficacy of Ce-Ca microalloying additions on modifying the microstructural characteristics of the alloys related to ductility. Examination of precipitation hardening behaviour is conducted using microhardness measurement, transmission electron microscopy, differential scanning calorimetry, atom probe tomography, and thermodynamic analysis. The microstructural characteristics of the alloys are also investigated by optical and scanning electron microscopy, electron backscatter diffraction, and neutron diffraction, with alloy ductility measured by tensile testing. This research consists of the following major components:

I. Precipitation in the Mg-Zn-Ca alloy system is examined for alloys with high Ca content, originally designed for biomedical use. An in-depth look at the precipitation sequence of an Mg-Zn-Ca alloy is provided.

II. The effects of Ce, added at both alloying and microalloying levels, on Mg-Zn alloys with different levels of Zn content are examined. The hardening responses of the alloys and the aged microstructures are analyzed. The relative hardening behaviour of the alloys is compared along with the calculated supersaturation values for the Zn and Ce solutes to establish the effect of Ce on precipitation.

III. The effect of double microalloying additions of Ce-Ca on the precipitation behaviour of Mg-Zn based alloys is investigated. Hardening responses are compared for different Zn contents and for various microalloying element combinations. The precipitation behaviour is further studied, with focus on:

   a. Examination of the precipitates and microstructures within the grains is conducted to identify the hardening precipitates and their evolution during ageing. The effects of the microalloying additions are determined by analysis of different alloys and ageing conditions.
   b. Solute segregation and precipitation at and near the grain boundary regions in the aged microstructure is investigated to determine the effects of the microalloying additions on grain boundary precipitation and precipitate free zone formation.

IV. The microstructural characteristics of Mg-Zn alloys with Ce-Ca microalloying additions in the rolled-and-annealed condition are examined, with focus on properties related to alloy ductility such as grain refinement, secondary phase fraction/distribution, and alloy texture. The microstructures produced by the various alloying/microalloying elements are related to their resultant tensile properties.

2 Literature Review

The following chapter reviews the current research into the effects of Ca and Ce on precipitation hardening and deformation/texture of magnesium alloys, particularly those based on the Mg-Zn system. The review begins with a look at general issues and characteristics of precipitation hardening in magnesium alloys, followed by more focused discussion of precipitation in binary Mg-Zn, and the Mg-Zn-Ca and Mg-Zn-Ce alloy systems. Research into the effects of Ce and Ca additions to improve the texture and ductility of magnesium alloys is then reviewed.

2.1 General Precipitation Hardening in Magnesium Alloys

The increase in yield strength due to precipitation hardening can be generally expressed as [29,75–77]:

$$s_{ppt} = \frac{MF}{bL} \tag{2-1}$$

Where M is the Taylor factor, F is the maximum force due to the interaction between a precipitate and the dislocation, b is the Burgers vector magnitude, and L is the average inter-particle spacing. The hardening due to precipitation in alloys is generally understood by the mechanisms through which moving dislocations interact with precipitates dispersed in the matrix. There are many factors that determine the nature of the precipitate-dislocation interactions, and therefore the degree of strengthening the precipitates provide. Generally, these interactions fall into two main categories: (a) shearing of precipitates by dislocations, and (b) Orowan looping mechanism when precipitates are non-shearable. If a precipitate can be sheared by dislocations as they pass through the matrix, there are several different mechanisms which can cause the material to be strengthened [76,77]. One such method is chemical strengthening, which is caused by the matrix-precipitate interface that is formed when a precipitate is sheared. Other methods include stacking fault strengthening, hardening due to differing precipitate-matrix shear moduli, and order strengthening. There can also be hardening that arises indirectly from precipitates, due to elastic strain fields that surround coherent particles with a certain amount of lattice misfit. The latter mechanism is of great importance in a number of precipitation hardening Al alloy systems [78–80]. When a precipitate is non-shearable, the dislocation can form a loop around the precipitate in a process known as Orowan looping [75]. In either cases of particle shearing or Orowan looping, the inter-particle spacing on the slip plane has a strong effect on the hardening due to precipitation, as shown in equation 2-1. Therefore, for a given volume fraction of precipitates, a higher number density of precipitates will produce a larger hardening response.

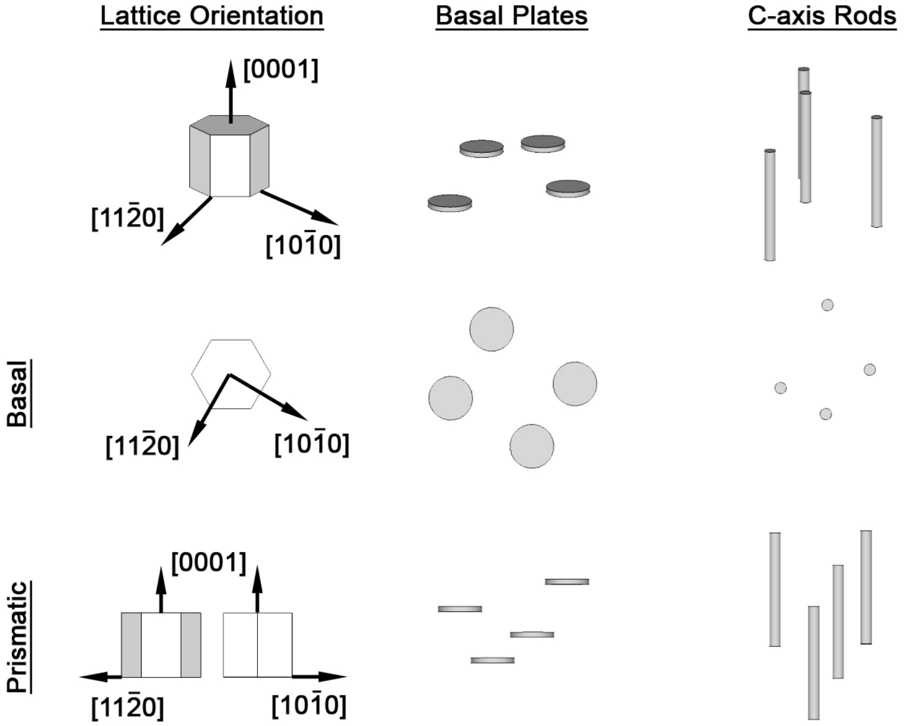

Figure 2-1: Schematic showing basal plate precipitates and c-axis rods as seen along the basal (0001) and prismatic $\{10\bar{1}0\}$ or $\{11\bar{2}0\}$ planes.

For a given precipitate volume fraction, the inter-particle spacing will also depend on the shape (morphology and aspect ratio) and orientation of the precipitates. Precipitates with different morphologies and orientation relationships to the matrix may have different effective inter-particle spacing, depending on the slip plane of the dislocations that they interact with [81]. The projected areas of precipitates with basal plate and c-axis rod morphologies/orientations for given lattice planes are presented schematically in Figure 2-1. The effect of these different morphologies and orientations on the effective inter-particle spacing for a given precipitate volume fraction and number density has been calculated by Nie [81] considering basal slip, and is shown in Figure 2-2.

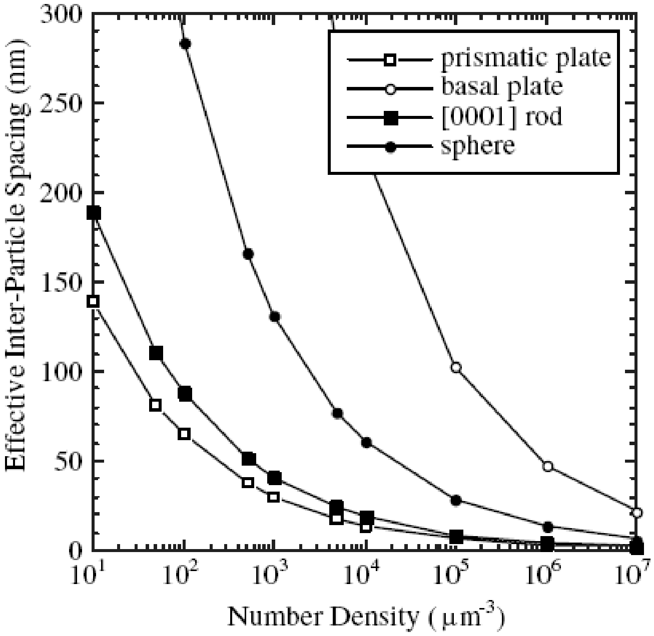

Figure 2-2: Effective inter-particle spacing vs. number density for different precipitate morphologies. Values are per unit volume of Mg, given a set precipitate volume fraction of 0.04, and an aspect ratio of 40:1 for rods and plates (from Nie [81]).

It has been suggested by Nie [81] that since magnesium alloys primarily deform by basal slip, that precipitates which are oriented to most effectively impede basal slip (i.e. with the lowest effective inter-particle spacings as experienced by a moving basal dislocation) will result in the greatest hardening. The combined effects of number density and precipitate morphology on inter-particle spacing for basal slip, as calculated by Nie [81], suggest that prismatic plate and c-axis rod morphologies will be the most efficient at strengthening in magnesium, due to their effectiveness at reducing inter-particle spacing along the basal plane.

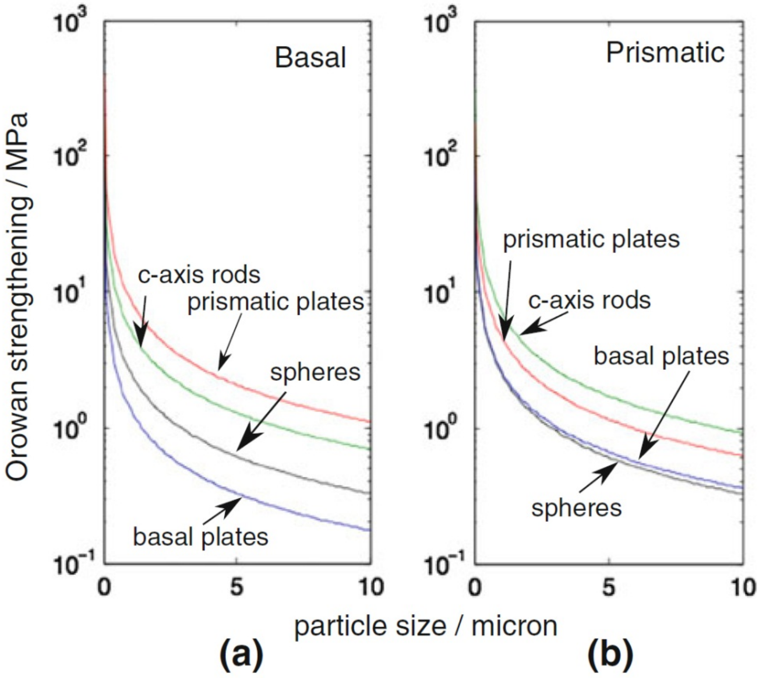

Figure 2-3: Calculated Orowan stress required to bypass different precipitate types for a) basal and b) prismatic slip, for a particle volume fraction of 5%, and an aspect ratio of 0.1 for plates and 10 for rods (from Robson et al. [82]).

In understanding the overall effectiveness of precipitates on hardening, it is important to also examine other deformation modes besides basal slip. This is especially relevant, given that recent observations of deformation in magnesium at room temperature suggest that while the majority of slip is accommodated by basal dislocations, it is non-basal slip, particularly prismatic $\langle a \rangle$ slip that controls macroscopic yielding [83,84]. A similar analysis to that of Nie [81] was performed by Robson et al. [82] which calculated the effective Orowan strengthening for different precipitate types on both basal and prismatic slip, with results shown in Figure 2-3

[82]. The results for basal slip agree with the calculations of Nie [81]. The results for prismatic slip show that c-axis rod precipitates become the most effective, with basal plates increasing in effectiveness compared to the case for basal slip. The importance of precipitation hardening in strengthening for both basal and non-basal deformation modes has been further highlighted by the recent work of Agnew et al. [84] on the deformation of aged WE43. In that alloy, the prismatic plate precipitates which formed were found to dramatically harden against basal slip, and yet only produce modest increases in yield strength. By studying the activity of each deformation mechanism, the researchers were able to observe that the macroscopic yield point correlated more with prismatic $\langle a \rangle$ slip and twinning, which were hardened much less by the prismatic plate precipitates in the aged WE43.

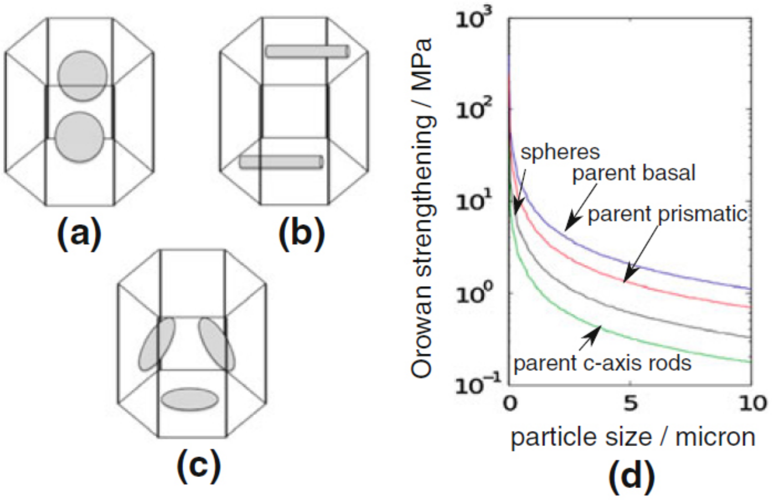

Figure 2-4: Schematic showing orientation of a) basal plate b) c-axis rod c) prismatic plate precipitates in twinned material, and d) calculated Orowan stress inhibiting basal slip for the different precipitate types within the twin, calculated for a particle volume fraction of 5%, and an aspect ratio of 0.1 for plates and 10 for rods (from Robson et al. [82]).

The effect of precipitation on twinning is also important to understand, as magnesium readily forms twins during deformation. Although much of the interactions between precipitates and twinning in magnesium still remains to be determined, some important findings have been reported in the literature. Precipitates have been observed to act as obstacles to twin propagation if the precipitates are of sufficient size relative to the twin [85]. More generally for precipitates involved in hardening, the precipitates have been found to be unsheared and engulfed by twins [86,87]. Considering the common case of $\{10\bar{1}2\}\langle 10\bar{1}1\rangle$ extension twinning, the lattice structure of the matrix undergoes a rotation of 86.3° about $\langle 11\bar{2}0\rangle$, which effectively changes the orientation of the precipitates in the twinned volume. This change in orientation also produces changes in the effectiveness of different precipitate morphologies at inhibiting basal slip within the twin, as shown schematically in Figure 2-4 [82]. The effect of precipitates on slip both within grains and twins can have important implications for strengthening against twinning. The stress required to grow a twin through a grain containing precipitates will be affected by both the Orowan stress on the twinning dislocation, as well as the back-stress resulting from strain incompatibility between the sheared matrix and un-sheared particle [82]. The Orowan stress on the twinning partial dislocation is likely very low due to the very short Burgers vector [86]. However, Robson et al. [82] have reported the back-stress due to strain incompatibility with the precipitates can result in strengthening against twin growth, particularly when the precipitates within the twinned volume also inhibit plastic relaxation of this stress by basal slip. This finding is supported by the report of Stanford et al. [88], who observed a greater increase in hardening of the $\{10\bar{1}2\}\langle 10\bar{1}1\rangle$ twinning system than predicted by the Orowan model for an AZ91 alloy aged to form large basal plate precipitates. It should be noted that such resistance against twin growth does not necessarily impede twin nucleation, which is consistent with the higher numbers of finer twins, with a lower total volume fraction, reported for aged Mg-Zn alloys Stanford and Barnett [87], and Robson et al. [89].

It can therefore be seen that while the fundamentals of precipitate-dislocation interactions are well known, the exact mechanisms by which precipitates in magnesium alloys effectively increase the yield strength are less understood, due to the complicated deformation behaviour of the material. In general however, it is likely that the most effective strategy for enhancing precipitation hardening is by promoting the formation of a high number density of precipitates with an efficient orientation for strengthening, considering both basal and non-basal deformation. A strong candidate system for such a precipitate microstructure is that of Mg-Zn, as the primary precipitates which form during ageing adopt a c-axis rod orientation/morphology, and the precipitate number density can be improved by alloying/microalloying strategies. The nature of precipitation hardening in binary Mg-Zn, and the results of current research into alloying/microalloying of that system with Ca and Ce are discussed in the following sections.

2.2 Precipitation Hardening of Binary Mg-Zn Alloys

The Mg-Zn system has been the subject of much investigation due to its marked precipitation hardening effect [18–20,42,90]. The precipitates of interest for strengthening purposes in the Mg-Zn system are the metastable β'_1 and β'_2 precipitates (β'_1 also referred to as MgZn′) which have been found to be rods that lie with their long dimension perpendicular to the basal plane, and plates on the basal plane, respectively. These precipitates are shown in Figure 2-5 [42], and are represented schematically in Figure 2-6 [41].

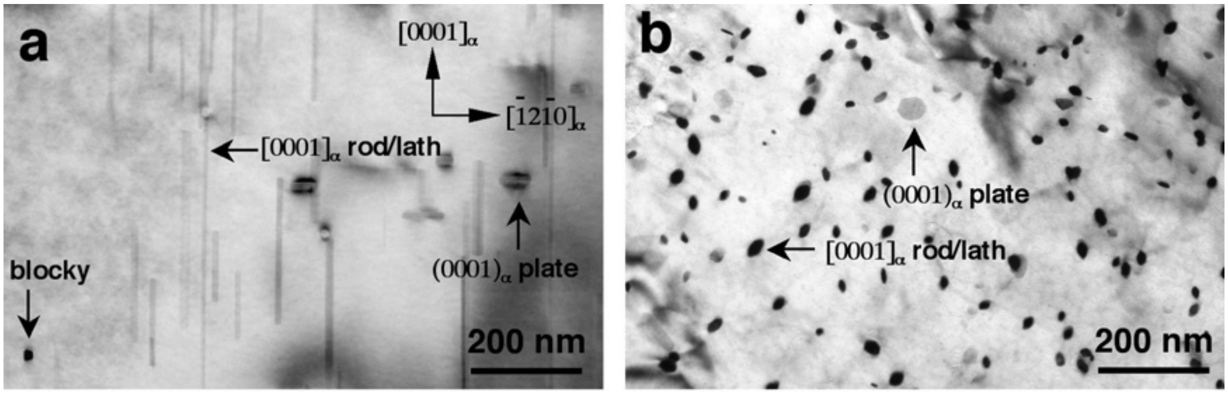

Figure 2-5: TEM micrographs for Mg-8Zn (wt%) aged 2 h at 200°C showing MgZn' precipitate rods and plates. Electron beam parallel to a) $\langle 10\bar{1}0\rangle$, and b) (0001) (from Gao and Nie [42]).

The earliest reports on the β'_1 and β'_2 precipitates identified both phases as the hexagonal $MgZn_2$ laves-C14 phase, with β'_1 having lattice parameters of a = 5.2 Å, c = 8.5 Å and an orientation relationship of $\{11\bar{2}0\}_{\beta'_1}||(0001)_{\mathrm{Mg}}$, $[0001]_{\beta'_1}||\langle 11\bar{2}0\rangle_{\mathrm{Mg}}$, and β'_2 having lattice parameters of a = 5.2 Å, c = 8.48 Å and an orientation relationship of $(0001)_{\beta'_2}||(0001)_{\mathrm{Mg}}$, $\langle 11\bar{2}0\rangle_{\beta'_2}||\langle 10\bar{1}0\rangle_{\mathrm{Mg}}$ [91]. This structure and orientation has been supported by some other researchers [40,41,92]. However, Gao and Nie [42] have reported the β'_1 phase to be monoclinic Mg_4Zn_7, with lattice parameters of of a = 25.96 Å, b = 14.28 Å, c = 5.24 Å, γ = 102.5°, and an orientation relationship of $\{630\}_{\beta'_1}||(10\bar{1}0)_{\mathrm{Mg}}$, $[001]_{\beta'_1}||[0001]_{\mathrm{Mg}}$. A still more recent report by Rosalie et al. [93] has identified domains of both $MgZn_2$ and Mg_4Zn_7 phases within the β'_1 rods. This report has identified the precipitates as having a core of Mg_4Zn_7 with an orientation relationship of $\{10\bar{1}0\}_{\mathrm{Mg}}\ ||(201)$, $[0001]_{\mathrm{Mg}}||[010]$, and the $MgZn_2$ phase growing on the Mg_4Zn_7 phase with two possible orientations. Both of these were oriented with respect to the Mg_4Zn_7 as $[11\bar{2}0]_{\mathrm{MgZn2}}||[010]_{\mathrm{Mg4Zn7}}$, and one had an orientation relationship with respect to the matrix of $\{11\bar{2}0\}_{\mathrm{Mg}}\ ||(0001)_{\mathrm{MgZn2}}$, $[0001]_{\mathrm{Mg}}||[11\bar{2}0]_{\mathrm{MgZn2}}$.

Additionally, it is notable that Gao and Nie [42] also reported that small fractions of the β'_1 phase form small blocky precipitates, and that the β'_2 phase occasionally adopts a lath shape, elongated along the [0001] matrix direction.

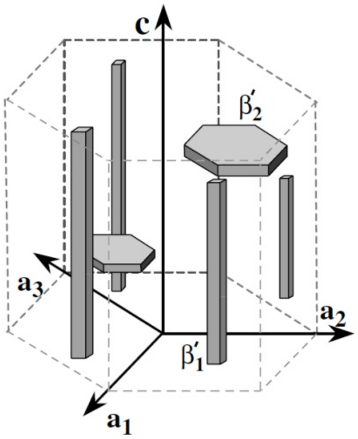

Figure 2-6: Schematic of precipitates in Mg-4Zn (wt%) aged 10^4 ks at 450 K (from Bettles et al. [41]).

Strengthening from these precipitates in the aged condition is primarily attributed to the β'_1 precipitates, as they are found in the highest numbers, with some contributions also from the β'_2 plates [20,42,91]. Considering the rod-like β'_1 precipitates, an early work by Clark [20] reported that these precipitates act as non-shearable obstacles to dislocations, and strengthen the alloy by Orowan looping. This is supported in the recent work by Jain et al. [94], who observed both basal and prismatic dislocations looping and bowing between β'_1 precipitates. It was also noted by Jain et al. [94] that the peak-aged condition for an Mg-6Zn (wt%) alloy aged at 200°C corresponded not only to achieving the maximum precipitate volume fraction, but also to reaching the peak aspect ratio of the β'_1 precipitates (i.e. maximum length per thickness). This observation is consistent with achieving a minimum inter-particle spacing, and maximum strengthening by hard obstacles according to the Orowan equation. As mentioned in section 2.1, the c-axis rod morphology of the β'_1 phase makes it predicted to be an efficient obstacle for impeding both basal slip and prismatic slip [81,82]. This is consistent with recent modelling work by Jain et al. [94], which has suggested that the increase in yield strength associated with β'_1 precipitation is due to hardening considering both basal and prismatic slip.

Table 2-1: Precipitate phases and precipitation sequences at various ageing temperatures for Mg-2.8Zn (at%), as reported by Buha [18]. All directions and planes are given with respect to the HCP-Mg lattice.

Temperature	Precipitation Sequence
160°C	Clusters → GP1 zones + [0001] Rods + (0001) GP zones → (0001) GP zones + (0001) Plates + (β'_1) [0001] Rods + (β'_2) [0001] Laths + (β'_1) [0001] Blocks + (β'_2) Plates
98°C	Clusters → Prismatic Precipitates + (0001) GP zones + (0001) Plates + [0001] Rods + [0001] Laths
70°C	Clusters → GP1 zones + Prismatic Precipitates + (0001) GP zones + (0001) Plates + [0001] Rods + [0001] Laths
22°C	Clusters → GP1 zones + Prismatic Precipitates

The precipitation sequence in binary Mg-Zn alloys remains a subject of continued study, as the precipitate evolution, particularly during the early stages of ageing, has yet to be unambiguously determined [21]. In the most recent work by Buha [18], several different precipitate types and sequences were reported for Mg-Zn aged at various temperatures. The sequences of precipitation at different temperatures, as reported by Buha [18], are listed in Table 2-1. It should be noted that GP1 zones are plates on $\{11\bar{2}0\}_{\mathrm{Mg}}$ and $(0001)_{\mathrm{Mg}}$ GP zones are plates on $(0001)_{\mathrm{Mg}}$ [18]. The formation of GP zones during ageing between 110°C and 60°C was also reported by Mima and Tanaka [90] through indirect observations of changes in alloy hardness and changes in lattice spacing with ageing. Additionally, a recent report by Bhattacharjee et al. [40] also claimed Zn-rich precipitates, observed by 3DAP analysis after ageing an Mg-6.2Zn (wt%) alloy 100 h at 70°C, to be GP zones which acted as precursors for the β'_1 and β'_2 precipitates. However, it should be noted that GP zones were not reported during earlier studies of binary Mg-Zn [20,91]. Overall, further detailed characterization is necessary to unambiguously confirm the presence of GP zones in the precipitation sequence for binary Mg-Zn alloys.

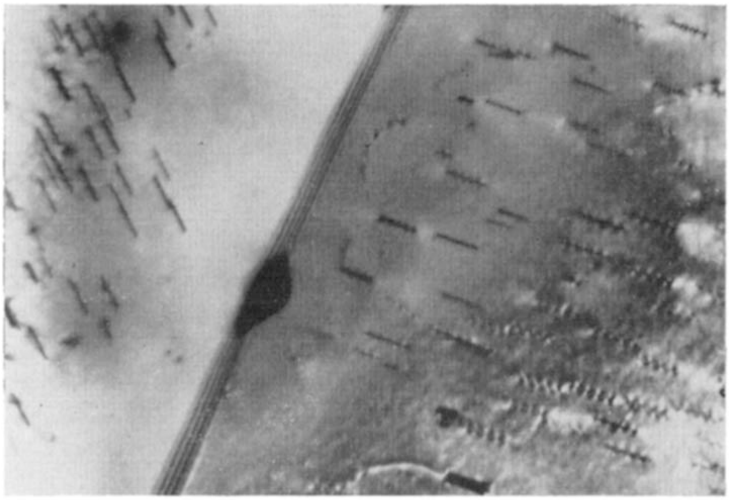

Figure 2-7: TEM image showing grain boundary precipitate and precipitate-free zone for an Mg-5Zn (wt%) alloy aged 6 h at 260°C, x12000 magnification (from Clark [20]).

Another feature of aged binary Mg-Zn alloys is the relatively coarse precipitates which have been reported to form on grain boundaries [20,90]. The formation of these grain boundary precipitates is also associated with a notable precipitate-free zone (PFZ) around the grain boundaries in the aged microstructures. Clark [20] reported a depletion of solute in the PFZ, which was attributed to the growth of the grain boundary precipitates during ageing. Clark [20] also reported the tendency of precipitates to form on twin boundaries and dislocations during ageing. A similar observation was made by Buha [18], who noted that precipitates tended to line up along $\langle 11\bar{2}0 \rangle$ matrix directions, but this was attributed to preferential nucleation of precipitates in the strain field of other precipitates.

It is therefore apparent that while the Mg-Zn system has been the subject of much study regarding precipitation hardening in magnesium alloys, there remains many aspects, particularly involving precipitate nucleation and evolution, which require additional investigation. Furthermore, while the nature of the binary system and the precipitates that form make it a desirable choice for precipitation hardening alloy development, key improvements are required to address the generally low precipitate number density, as well as PFZ formation.

2.3 Precipitation Hardening of Mg-Zn-Ca Alloys

Several works have examined precipitation hardening in the Mg-Zn-Ca system, involving various levels of the two solute elements. To portray a full representation on the reported precipitation behaviour of this system, this review will cover both alloying and microalloying additions, beginning with alloys that have higher Ca:Zn ratios, and generally moving towards alloys with lower relative amounts of Ca.

Comparisons of the precipitation hardening responses of alloys described in this section will be made primarily with binary Mg-Zn alloys, but for Ca-rich Mg-Zn-Ca alloys, it is also worth a brief comparison to binary Mg-Ca. Nie and Muddle [95] reported an improvement in peak hardness of an Mg-1Zn-1Ca alloy over an Mg-1Ca binary alloy (both in wt. %) by the formation of ternary precipitates. Based on calculations, it was reported that these precipitates had lower lattice misfit with the matrix due to the inclusion of Zn. Such an effect facilitated a finer distribution of precipitates and enhanced nucleation rate in the Zn containing alloy. Ortega et al. [96], also reported a increased precipitation hardening response due to interactions between Ca and Zn during ageing of an Mg-1Zn-1Ca (wt%) alloy at 200°C by positron annihilation spectroscopy investigations. From these results, it was suggested that Ca-Zn solute pairs formed during the early stages of ageing.

The nature of Ca and Zn to positively-interact to form clusters and precipitates was also evident from the investigation into the microstructure of an Mg-1.6Zn-0.5Ca (wt%) alloy after ageing at 200°C by Oh-ishi et al. [53]. Those researchers found that the precipitates in the peak-aged condition were fine monolayer GP zones on the (0001) basal planes. HAADF-STEM observations of the GP zones revealed periodic bright spots with spacing of $\frac{3}{2}a_{\mathrm{Mg}}$, indicating a higher amount of heavy solute elements along those atomic columns. The structure of the GP zones was reported to be ordered, with alternating over-sized Ca and under-sized Zn solute atoms according to the structure first reported by Ping et al. [97]. A representation of this structure is shown in Figure 2-8. Together, these different-sized solutes were reported to promote the formation of these GP zones by relieving the misfit lattice strain along the basal plane.

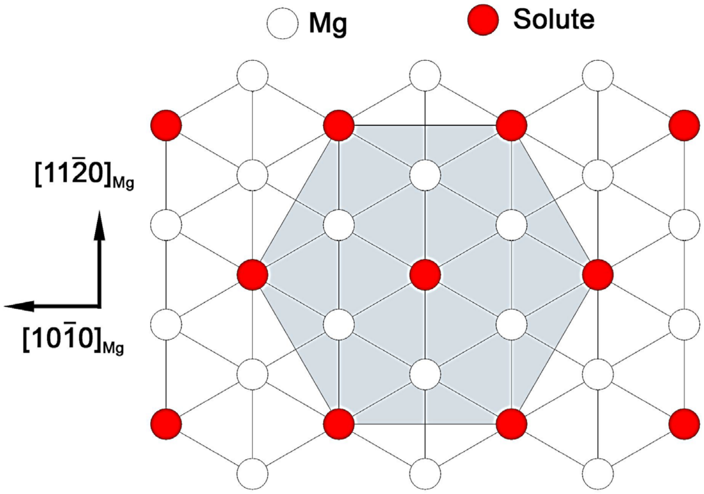

Figure 2-8: Schematic of the ordered GP zone structure formed along a single basal plane of the HCP-Mg lattice, reproduced based on the descriptions of Ping et al. [97] (for solute of RE/Zn) and Oh-ishi et al. [53] (for solute of Ca/Zn). Shaded area shows hexagonal cell of GP zone formed by solutes.

With continued ageing, Oh-ishi et al. [53] noted that aside from some coarse precipitates found on basal planes, the microstructure remained similar, and the GP zones did not coarsen or transform, but only elongated slightly while remaining as monolayers. This is contrasted by the behaviour of an Mg-0.8Zn-0.5Ca (wt%) alloy during ageing at 200°C, as reported by Oh et al. [52]. For that alloy, while monolayer GP zones were also the sole contributor to hardness in the peak-aged condition, over-ageing led to the formation of large, thin plate precipitates on basal planes. However, nanoscale monolayer precipitates were also observed along basal planes, which were found in pairs separated by about 2.5 nm along the [0001] matrix direction. 3DAP analysis of these nanoscale precipitate pairs revealed them to be enriched in both Ca and Zn. With continued ageing at 200°C, these nanoscale precipitate pairs are observed to disappear, while the basal plates continue to thicken and grow. Additionally, rectangular-shaped precipitates are also observed, and identified be the hexagonal Mg_2Ca phase, which contained Zn and exhibited an orientation relationship of either $(0001)_{ppt}||\{10\bar{1}0\}_{\mathrm{Mg}}$, $\langle 11\bar{2}0\rangle_{ppt}||\langle 11\bar{2}0\rangle_{\mathrm{Mg}}$, or $(0001)_{ppt}||(0001)_{\mathrm{Mg}}$, $\langle 11\bar{2}0\rangle_{ppt}||\langle 10\bar{1}0\rangle_{\mathrm{Mg}}$. The lattice parameters of the Mg_2Ca phase were determined by SADP to decrease from $a = 6.23$ Å and $c = 10.18$ Å to $a = 5.80$ Å and $c = 9.41$ Å with increasing incorporation of Zn in the Mg_2Ca.

An alloy with a lower amount of Ca relative to Zn was studied by Bettles et al. [41], who reported on the microstructure of an Mg-4Zn-0.35Ca (wt%) alloy aged at 177°C. TEM analysis revealed the peak-aged microstructure to contain the β'_1 phase, but also fine precipitate plates parallel to the (0001) basal planes of the HCP-Mg lattice. Similar fine basal plate precipitates were also observed by Oh-ishi et al. [53] for an Mg-4.2Zn-0.5Ca (wt%) alloy aged 61 h at 200°C. The fine basal plate precipitates in that work were identified by micro-diffraction analysis as ellipsoidal $Mg_6Ca_2Zn_3$ phase. Levi et al. [98] also identified relatively coarse $Mg_6Ca_2Zn_3$ upon over-ageing of an Mg-3.2Zn-1.6Ca (wt%) alloy for 96 h at 225°C. The $Mg_6Ca_2Zn_3$ phase is described by Jardim et al. [99,100] as a trigonal compound of space group $P\bar{3}1c$, with lattice parameters of a = 9.7 Å and c = 10.0 Å. The structure of the $Mg_6Ca_2Zn_3$ phase is shown schematically in Figure 2-9. Two orientation relationships for the $Mg_6Ca_2Zn_3$ phase were reported by Jardim et al. [99]: $\{11\bar{2}0\}_{ppt}||(0001)_{\mathrm{Mg}}$, $[0001]_{ppt}||\langle 11\bar{2}0\rangle_{\mathrm{Mg}}$, and $\{11\bar{2}0\}_{ppt}||(0001)_{\mathrm{Mg}}$, $[0001]_{ppt}||\langle 21\bar{3}0\rangle_{\mathrm{Mg}}$. It is notable that these are not identical to the orientation relationship reported by Oh-ishi et al. [53] for the fine ellipsoidal $Mg_6Ca_2Zn_3$ of $\{10\bar{1}0\}_{ppt}||\{10\bar{1}0\}_{\mathrm{Mg}}$, $[0001]_{ppt}||[0001]_{\mathrm{Mg}}$. Two additional types of basal precipitates were also observed by Oh-ishi et al. [53] for the over-aged Mg-4.2Zn-0.5Ca, which were found to extend along the $\langle 11\bar{2}0\rangle$ and $\langle 10\bar{1}0\rangle$ directions respectively, and remain unidentified.

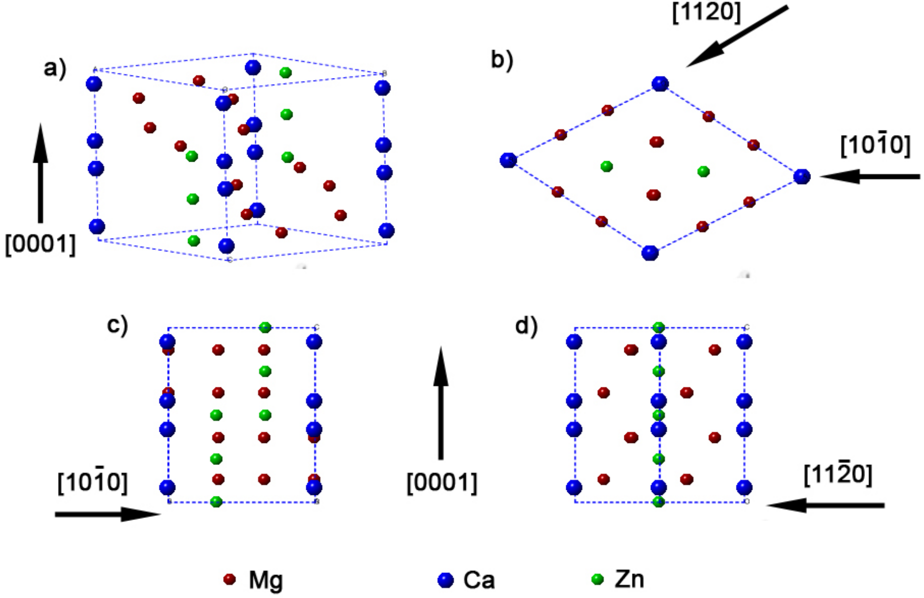

Figure 2-9: Model of the $Mg_6Ca_2Zn_3$ equilibrium phase, as described by Jardim et al. [100], showing a) the unit cell, and additionally from b) [0001], c) $[11\bar{2}0]$, and d) $[10\bar{1}0]$ directions. Note that directions correspond to the $Mg_6Ca_2Zn_3$ phase, and not its orientation within the HCP-Mg matrix.

Table 2-2: Summary of reported precipitates in Mg-Zn-Ca alloys. Note: SADP analysis included as TEM.

Alloy (wt%)	Ageing Temp. (°C)	Ageing Time (h)	Precipitates Reported	Analysis Method(s)	Ref.
Mg-1Zn-1Ca	200	24	Fine scale precipitates on basal planes	TEM	[95]
Mg-3.2Zn-1.6Ca	225	24	$Mg_6Ca_2Zn_3$	TEM	[98]
Mg-0.8Zn-0.5Ca	200	0.56	Monolayer GP zones on basal planes	TEM	[52]
		16.7	Nanoscale basal precipitate pairs, large thin basal plates	TEM, 3DAP	[52]
		55.6	Rectangular Mg_2Ca containing Zn, large basal precipitate plates	TEM, 3DAP	[52]
Mg-1.6Zn-.5Ca	200	1.4	Monolayer GP zones on basal planes	TEM, HAADF-STEM	[53]
		61	Monolayer GP zones on basal planes, coarse basal precipitates	TEM, HAADF-STEM	[53]
Mg-4.2Zn-0.5Ca	200	61	[0001] rods, fine ellipsoidal $Mg_6Ca_2Zn_3$, basal plates	TEM	[53]
		330	[0001] rods, fine ellipsoidal $Mg_6Ca_2Zn_3$, basal plates extending along $\langle 11\bar{2}0 \rangle$ and $\langle 10\bar{1}0 \rangle$ directions	TEM	[53]
Mg-6Zn-1.5Ca (melt spun)	200	1	Spherical and cuboid $Mg_6Ca_2Zn_3$	TEM	[99]
Mg-4Zn-0.35Ca	177	2700	Refined β'_1, β'_2, fine basal precipitates	TEM	[41]
Mg-6.2Zn-0.2Ca	160	0.5	No precipitates or clustering	TEM, 3DAP	[40]
		4	Fine β'_1 containing Ca	TEM, 3DAP	[40]
Mg-6.1Zn-0.4Ag-0.2Ca	160	2	Fine β'_1 , Ca-Zn co-clusters	TEM, 3DAP	[101]
		72	Fine β'_1 containing Ca	TEM, 3DAP	[101]

It is notable that in addition to promoting the formation of fine precipitate phases, Ca additions have also been reported to impart additional precipitation hardening to Mg-Zn alloys by refining the β'_1 precipitate phase distribution [40,41,101]. Such an effect was reported in the previously-mentioned work of Bettles et al. [41] in which fine basal precipitates were observed; however, a refinement of the β'_1 precipitates has also been reported for alloys with very high Zn:Ca ratios, in which no additional precipitate types are identified [40,101]. Bhattacharjee et al. [40] recently reported for an Mg-6.2Zn-0.2Ca (wt%) alloy, that the addition of Ca increased the number density of the β'_1 precipitates by an order of magnitude during ageing at 160°C, compared to a binary Mg-6.2Zn alloy. It is notable that in that work, fine precipitates, reported as β'_1, were found by 3DAP after 4 h of ageing at 160°C which contained approximately 1 at% Ca. 3DAP analysis after 30 mins of ageing at 160°C however did not provide evidence for Ca-Zn co-clusters. An earlier work on a similar Mg-6.1Zn-0.4Ag-0.2Ca (wt%) alloy by Mendis et al. [43] did detect Ca-Zn co-clusters by 3DAP after 2 h of ageing at 160°C. The co-clustering of Ca and Zn was attributed to the Zn solute atoms, with a relatively small size compared to Mg, relieving the misfit lattice strain of the relatively over-sized Ca solutes. The Ca-Zn co-clusters were reported by Mendis et al. [43] to possibly act as nucleation sites for the β'_1 precipitates, which resulted in increasing their number density and enhancing the hardening response.

The results from literature on precipitation hardening in Mg-Zn-Ca alloys therefore report that overall, the addition of Ca to Mg-Zn alloys dramatically improves the precipitation hardening response. This increase in the precipitation hardening response can be due to the formation of additional fine phases such as GP zones, or by refining the precipitates typical of the Mg-Zn system and increasing their number density. A summary of these results is given in Table 2-2.

While the improvement in hardening response in all cases can be related back to the positive interactions between Ca and Zn solute atoms during ageing, the full nature of these interactions, the effects of Ca on Zn phase nucleation, and the exact identification of all the various Zn-Ca-containing precipitate phases and their evolution, remain unclear. Additionally, there is a lack of comprehensive knowledge on the effects of different Zn:Ca ratios and ageing temperatures on the precipitates. In-depth understanding of the precipitation behaviour in this system can lead to advances in both alloy design and precipitation hardening response.

2.4 Precipitation Hardening of Mg-Zn-Ce Alloys

Numerous alloying and microalloying additions to the Mg-Zn system have been studied, yet precipitation hardening in the Mg-Zn-Ce system has received relatively little investigation compared to Mg-Zn alloyed with other, more soluble RE elements such as Nd or Gd [21,22,102]. For most studies on precipitation hardening, Ce has not been added as a single alloying/microalloying addition, but rather as a component of Ce-rich mischmetal (MM). Wei et al. [103] studied two such alloys, Mg-8Zn-1.5MM and Mg-4Zn-1.5MM (wt%), where the MM was composed of approximately 50Ce-25La-20Nd-3Pr (wt%). They reported that upon ageing at 200°C, the hardening response of the alloys was similar to that of a binary Mg-9Zn (wt%) alloy, however the time to reach the peak-aged condition increased for the MM-containing alloys. The Mg-Zn-MM alloys also appeared more resistant to over-ageing than the binary Mg-Zn alloy. This resistance to over-ageing was attributed to a larger amount of β'_2 precipitate plates in the binary alloy.

Ping et al. [97] examined precipitates in an Mg-2.4MM-0.4Zn-0.6Zr alloy, with a MM composition of 54Ce-25La-17Nd-4Pr (both wt%) aged at 200°C. TEM analysis revealed fine, monolayer precipitates along the basal plane. These precipitates were identified as ordered GP zones, and notably exhibited streaking along the [0001] direction in the $\langle 11\bar{2}0\rangle$ zone axis SADP, and along the [0001] direction at $1/3\{11\bar{2}0\}$ and $2/3\{11\bar{2}0\}$ in the $\langle 10\bar{1}0\rangle$ zone axis SADP, as well as extra reflections at $1/3\{11\bar{2}0\}$ and $2/3\{11\bar{2}0\}$ in the [0001] zone axis SADP. The structure of these GP zones was described as consisting of under-sized Zn atoms and over-sized rare earth atoms, arranged to minimize misfit strain, as shown schematically in Figure 2-8 but for RE/Zn solutes. 3DAP analysis of these fine GP zones detected 3.7% Nd, 1.0% Ce, and 1.4% Zn (all at%). However, it was reported that these compositions were likely underestimated by the 3DAP technique.

Nishijima et al. [104] performed a study on precipitates in an Mg-10Ce-2.4Zn (wt%) alloy. However, due to the high Ce content, the alloy was prepared by rapid solidification (melt spinning) and annealing at 200-400°C instead of standard solutionizing and ageing heat treatments. The precipitates found in the annealed alloy were hexagonal and fully coherent with the HCP-Mg matrix. An ordered superlattice structure was reported for these precipitates with lattice parameters of $a = \sqrt{3}a_{\mathrm{Mg}} = 5.71$ Å and $c = c_{\mathrm{Mg}} = 5.21$ Å, and a space group of $P\bar{6}2m$. The estimated composition of the precipitates was described as Mg_5(Ce,Zn). Several anti-phase boundaries were observed within the reported precipitate lattice. It was noted that this precipitate was observed to be stable during annealing up to 300°C, but transformed to the equilibrium Mg_{12}Ce phase by annealing at 400°C.

As evident by the lack of reporting on precipitation in the Mg-Zn-Ce system, the age-hardening and precipitate evolution behaviour of these alloys remains poorly established. Furthermore, many reports have focused on Ce-rich mischmetal addition, which makes it difficult to fully establish the effect of Ce on precipitation. Additions of Ce to Mg-Zn alloys are of current interest for their beneficial effects on texture and ductility [73,105]. Therefore, to fully understand and optimize precipitation hardening in this alloy system so that good combinations of ductility and strength can be achieved, it is necessary to investigate precipitation hardening in the Mg-Zn-Ce system.

2.5 Effect of Ce and Ca Additions on the Ductility and Texture of Magnesium Alloys

The following section will review the reported effects of Ce and Ca additions to Mg/Mg-Zn, with respect to alloy ductility. In particular, the microstructural characteristics related to ductility will be covered, primarily focusing on alloy texture and considering grain refinement.

In improving ductility in magnesium, it is well-reported that RE elements can significantly weaken the basal textures, typical of pure Mg and standard magnesium alloys. The origins of this texture modification effect are still the subject of much ongoing research, and not the primary focus of the current work. However, some major findings of the research into the origins of this effect will be briefly reviewed.

Reports on RE texture modification have attributed the effect to particle stimulated nucleation (PSN) [106–108], which is able to produce a random alloy texture [67]. However, other studies have questioned the significance of PSN in the overall recrystallized microstructure of magnesium alloys [109,110]. It is also noted that several Mg-RE systems exhibit texture modification when no secondary phase particles are present [71,111], and therefore the effect in those alloys cannot be due to PSN. The ability of RE elements to modify texture through solute effects has been linked with the influence of these solutes on activating non-basal slip [71,112,113]. Additionally, RE solutes have been reported or hypothesized to segregate to grain boundaries [71,114], and/or dislocations [68,70,115], and thereby retard dynamic annealing processes and allow for a microstructure with a weakened texture to form [68,71,110,114,116]. A weakened texture has been suggested to form in such a case as a result of a) affecting the dynamic recrystallization (DRX) mode [71,110], b) giving a growth advantage to non-basal oriented grains during recrystallization [114,117], or c) affecting the nucleation sites for new recrystallized grains [110,111,114].

Binary Mg-Ce alloys have generally exhibited refined grain size, a weakened texture, and increased ductility compared to pure Mg [69,70,74]. Mishra et al. [74] reported that additions of 0.2 wt% Ce to magnesium extrusions significantly enhanced the ductility by refining the grain size and promoting a texture with the basal planes rotated 40-50°C from the extrusion axis. Stanford [70] observed that in microalloying Mg with Ce, texture strength could be reduced with a lower amount of Ce alloying element, compared to additions of soluble Y and Gd. A similar observation was also made by Hantzsche et al. [69] in comparing additions of Ce with those of Nd and Y. The potency of Ce was attributed by Stanford [70] to its large atomic radius (compared to Mg, and most other RE elements), which was suggested to promote segregation of Ce solutes to dislocations, whereby texture modification could be achieved by the aforementioned mechanisms.

Ce additions to Mg-Zn alloys also are generally reported to improve ductility and related microstructural characteristics, but are more dependent on the alloy composition. Bohlen et al. [118] investigated several Mg-Zn-Ce based alloys with low (< 1.0 wt%) levels of Ce, and found that the peak intensity for the basal poles in the rolled sheet rotated away from the plane normal, along the rolling directions. However, the greatest spread of the basal poles was along the transverse direction. This led to lower flow stress and higher ductility along the transverse direction during subsequent mechanical testing. It was also noted that the in-plane anisotropy *r*-values of the sheets were generally decreased, especially along the transverse direction, which has positive implications for general sheet formability. A rotation of basal poles towards the transverse directions was also observed by Mackenzie and Pekguleryuz [117] following rolling of Mg-1Zn-(0.3, 0.6, 1.0)Ce (wt%) alloys. Luo et al. [73] reported that for Mg-(2, 5, 8)Zn-0.2Ce (wt%) extrusions, the texture and ductility were generally improved in the Mg-Zn-Ce alloys compared to AZ31, but that ductility decreased with increasing Zn content over a binary Mg-0.2Ce (wt%) alloy. A similar observation was made by Sanjari et al. [119], who studied rolled alloys of Mg-1Zn-0.5Ce, Mg-1Zn-1Ce, Mg-2Zn-1Ce, and Mg-4Zn-1Ce. Those researchers reported that while the basal texture intensities were lowerd by Ce additions, that weaker textures were observed to correspond to higher Ce:Zn ratios. Relatively high amounts of Ce to ZK60 were added by Park et al. [120] (1.0 wt%) and Yu et al. [108] (0.5, 1.0, 1.5 wt%), but due to the high Zn content of the ZK60 alloy, the Ce:Zn ratios were still relatively low. In all cases those researchers reported a weakened texture and refined grain size with Ce addition. However, the alloys examined by Yu et al. [108] notably exhibited a decrease in tensile elongation with increasing Ce. This reduction in ductility was attributed to higher amounts of Mg-Zn-Ce particles in the alloys with increased Ce content.

There have been fewer reports on the effects of Ca on the ductility and microstructure of Mg and Mg-Zn based alloys than on the effects of Ce, and the findings of these reports are much less consistent. Stanford and Barnett [111] reported that while Ca refined grain size in an extruded binary Mg-0.1Ca (wt%) alloy, the texture strength increased. When normalized for grain size, the texture of this Mg-Ca alloy led to a decreased ductility compared to pure Mg. A later report by Stanford [59] however found that Ca additions could improve the texture of Mg-

Ca extrusions, but that this did not translate into improved ductility. The lower ductility of the Mg-Ca alloys, despite their more favourable textures, was attributed in that work to the presence of coarse Mg_2Ca particles in the alloys. Additions of Ca to Mg-Zn based alloys however have been reported to have a generally more positive effect. Zhang et al. [121] reported that additions of 0.2Ca and 0.5Ca to Mg-1Zn (all wt%) resulted in grain refinement, texture weakening, and ductility enhancement. Kim et al. [108] have also reported a weakened texture for rolled Mg-1Zn-1Ca and Mg-6Zn-1Ca (wt%) alloys, noting a split of the basal poles along the transverse direction in the annealed condition. Those researchers attributed the formation of this texture to the preferred growth of extension twin oriented grain nuclei. It is notable that the total elongations reported for the alloys in that work were still fairly low, and that a higher elongation was found for the alloy with higher Zn content (12.3% elongation for Mg-1Zn-1Ca and 17.2% for Mg-6Zn-1Ca).

Ce and Ca both have the potential to positively influence the ductility and microstructure of Mg and Mg-Zn based alloys. However, the different alloys reported in literature, particularly those based on the Mg-Zn-Ce and Mg-Zn-Ca systems, currently exhibit varied improvements in both ductility and texture, and there is a lack of reporting on the combined additions of Ce-Ca. Therefore, while Ce and Ca are strong candidate elements for alloy design, continued research is required to fully understand the effects of Ce, Ca, and Ce-Ca additions on ductility and texture.

2.6 Summary

The strength and ductility of magnesium alloys can be increased by precipitation hardening, and texture modification through RE element addition, respectively. However, many significant details regarding the application of these methods and their effectiveness in magnesium alloys remain poorly understood. Among common magnesium alloy systems, Mg-Zn has demonstrated potential for precipitation hardening, which can be enhanced by adding other alloying/microalloying elements. The addition of Ca to Mg-Zn has been found to be particularly effective at enhancing precipitation, but there is a lack of comprehensive understanding on the exact nature of the precipitation processes, and effects of alloy chemistry for the Mg-Zn-Ca system. The effects of Ce on the precipitation hardening behaviour of Mg-Zn remain relatively unreported. Both of these elements have also shown promise in improving the microstructure, texture, and ductility of Mg-Zn based alloys, with Ce noted to be particularly effective. However, no current knowledge exists for the effects of combined additions of Ca and Ce on the microstructural characteristics or ductility of Mg-Zn, or on the precipitation hardening capabilities of Mg-Zn-Ce-Ca alloys. Therefore, given the potential of Ca and Ce to achieve simultaneous improvement in the key properties of alloy strength and ductility, through precipitation hardening and microstructure modification, it is of considerable significance for magnesium alloy development to examine and understand the individual and combined effects of these elements on Mg-Zn.

3 General Methodology

The choice/design of the compositions of the magnesium alloys studied in this work are described in the subsequent chapters which detail their analysis. Thermal-mechanical processing routes and analysis procedures related to specific experiments described in certain chapters will also be detailed therein. The following describes the general preparation, processing, and analytical methods employed in this work.

3.1 Material Preparation

All experimental alloys studied in this work are composed of elements within the Mg-Zn-Ce-Ca system. The alloy designations are assigned based on the typical naming convention for magnesium alloys (ASTM-B951-11), where the letters specify the alloying elements used (e.g Z for Zn, E for rare earth (Ce), and X for Ca), and the numbers denote their respective content in wt% rounded to the first significant digit. The alloy designations and compositions are listed in Table 3-1.

The experimental magnesium alloys studied in this work were either supplied by CanmetMATERIALS in the as-cast condition (i.e. group A and B alloys), or prepared personally by casting (group C alloys). The group A and B alloys include X2, XZ21, XZ22, ZE21, and ZE41. The group C alloys are Z2, ZE20, ZEX200, Z4, ZE40, ZX40, and ZEX400.

Preparation of the group C alloys was done using solute-rich master alloys of Mg-Ce and Mg-Ca. These were prepared prior to casting by arc melting. The use of master alloys for these elements was necessitated by the low target levels of these elements in some of the alloys, and the high reactivities of the pure Ce and Ca. Zn and Mg were added as pure components. The casting materials were melted using an induction furnace in a graphite crucible and a split copper mould. To avoid oxidation of the melt, the casting chamber was kept under a positive pressure Ar atmosphere. Melts were heated to approximately 750-800°C in order to liquefy any possible solute-rich intermetallic compounds, and obtain a single-phase liquid of uniform composition. To reduce possible composition gradients in the melt, it was agitated with a graphite rod repeatedly during melting, and just prior to casting. The copper mould was kept at room temperature prior to casting, and allowed to cool to room temperature within the Ar casting chamber. The mass of each ingot prepared per melt was 175-200g.

Table 3-1: Compositions of experimental alloys, in wt% (at%).

Group	Alloy Designation	Mg	Zn	Ca	Ce
A	X2	(balance)	-	2.3 (1.41)	-
	XZ21	(balance)	0.9 (0.34)	2.1 (1.29)	-
	XZ22	(balance)	1.8 (0.68)	1.9 (1.17)	-
B	ZE21	(balance)	2.0 (0.76)	-	1.0 (0.18)
	ZE41	(balance)	4.0 (1.54)	-	1.0 (0.18)
C	Z2	(balance)	1.6 (0.60)	-	-
	ZE20	(balance)	1.8 (0.68)	-	0.11 (0.019)
	ZEX200	(balance)	2.0 (0.75)	0.3 (0.18)	0.10 (0.018)
	Z4	(balance)	4.0 (1.52)	-	-
	ZE40	(balance)	4.0 (1.53)	-	0.10 (0.018)
	ZX40	(balance)	4.0 (1.53)	0.3 (0.19)	-
	ZEX400	(balance)	4.0 (1.53)	0.3 (0.19)	0.10 (0.018)

The compositions of the alloys were verified using inductively coupled plasma mass spectrometry (ICP-MS). Measurements were performed at several different locations on the cast ingots to also check for possible macrosegregation, which could result in large-scale variations in the solute distribution. In cases where such macrosegregation was detected, the ingot was sectioned and re-melted. In general, this process did not require more than one repeat before a uniform composition was achieved.

3.2 Thermal-Mechanical Processing

The cast materials were given a homogenizing/solutionizing heat treatment prior to any further processing. This heat treatment was carried out in two stages, with no cooling between stages. The first stage was performed to eliminate any non-equilibrium eutectic. The second stage was performed at higher temperatures to homogenize the cast structure and dissolve solute elements. These heat treatments were performed in air atmosphere, and followed by a water-quench. Therefore, some oxide would typically be formed on the surfaces, which was removed by light grinding. Following this heat treatment, alloys were considered to be in the homogenized condition. Note that for the alloys with high-Ca content, as no further high temperature heat treatment was conducted this condition was also considered as the solutionized condition.

For alloys in group C, sections were also cut from the homogenized ingots and rolled from a thickness of 3.0 mm to 0.5 mm, using a reduction of approximately 0.25 mm per pass and a feed rate of approximately 80 mm/s. Rolling was performed on samples heated to 400°C, using heated rollers in order to minimize sample cooling during rolling. Temperature measurements of the rolling setup indicated the temperature of the rollers to be 150-180°C. Between each rolling pass, the samples were annealed at 400°C for 10 minutes. Following the final rolling pass, samples were annealed at 400°C for 30 minutes in order to fully recrystallize the deformed microstructures. For samples which were processed by the rolling and annealing treatments described above, they are referred to as in the rolled condition or the annealed condition. Note that alloys in group A and B were not rolled, as their high Ca and Ce contents produced a significant number of large secondary phase particles in the homogenized state, which made samples frequently crack and fracture during attempted rolling operations.

Prior to any age-hardening heat treatments of the annealed alloys, solutionizing heat treatments were performed. As the thickness of the rolled samples was low, alloys were protected from oxidation during solutionizing by either performing the heat treatments under Ar atmosphere, or by packing the samples in MgO powder. The solutionizing heat treatments were followed by fast quenching in water.

Table 3-2: Homogenizing, rolling/annealing, and solutionizing heat treatment parameters for experimental alloys.

Group	Alloy Designation	Homogenization Stage 1	Homogenizing Stage 2	Rolling / Annealing	Solutionizing
A	X2	315°C 5 h	505°C 24 h [1]	-	-
	XZ21	315°C 5 h	480°C 24 h [1]	-	-
	XZ22	315°C 5 h	480°C 24 h [1]	-	-
B	ZE21	300°C 5 h	400°C 24 h	-	490°C 6 h
	ZE41	300°C 5 h	400°C 24 h	-	490°C 6 h
C	Z2	300°C 5 h	400°C 24 h	400°C 0.5 h	520°C 6 h
	ZE20	300°C 5 h	400°C 24 h	400°C 0.5 h	520°C 6 h
	ZEX200	300°C 5 h	400°C 24 h	400°C 0.5 h	420°C 6 h
	Z4	300°C 5 h	400°C 24 h	400°C 0.5 h	420°C 6 h
	ZE40	300°C 5 h	400°C 24 h	400°C 0.5 h	420°C 6 h
	ZX40	300°C 5 h	400°C 24 h	400°C 0.5 h	420°C 6 h
	ZEX400	300°C 5 h	400°C 24 h	400°C 0.5 h	420°C 6 h

[1] As no further high temperature heat treatment is given, this constitutes solutionizing of the alloy

A full list of the homogenizing and solutionizing heat treatments given for each alloy is given in Table 3-2. The exact temperatures used for each alloy of group B and C and each heat treatment stage were arrived using on FactSage thermodynamic calculations. The heat treatments were designed in order to maximize the heat treatment temperature, and thereby maximize the amount of dissolved solute, while not inducing any melting by surpassing the calculated solidus temperature.

For artificial ageing, the heat treatments were conducted on solutionized alloys immediately following quenching. Ageing was performed in air atmosphere. The exact times and temperatures of the ageing heat treatments performed in this study are listed in the respective chapters that detail the analysis of those ageing conditions.

3.3 Mechanical Testing

3.3.1 Hardness Testing

Hardness testing was done using an MHT series LECO 200 Vickers microhardness tester and a 100g load. Indentations were made with a minimum separation of 2.5x the diagonal spacing, and were recorded only if the two diagonal lengths matched to within 5% of each other. A minimum of seven separate indentations were made, with more often used to reduce the variability between grains for the non-rolled samples. The highest and lowest values were culled and the remaining values averaged to produce the reported results, with error bars given as one standard deviation assuming a normal distribution.

3.3.2 Tensile Testing

Tensile specimens were prepared by machining from rolled material with an approximate thickness of 0.50 mm. The width of the reduced-area was 5.0 mm, and gauge length was 20.0 mm. Tensile testing was conducted at room temperature using an Instron 5548 micro tensile tester with 1 kN load cell, an extensometer with a 12.5 mm gauge length, and a strain rate of $3.0\text{x}10^{-4}$ s^{-1}. Tests on each alloy were repeated 3-5 times, as necessary to ensure reduced variances. Reported results are averages, with outlying points culled from the data as identified by assuming results to be normally distributed.

3.4 Microscopy & Microstructure Characterization

3.4.1 Optical Microscopy

Samples were prepared for optical microscopy (OM) by grinding with SiC paper up to 1200 grit, using water as a lubricant. This was followed by additional grinding at 1200 grit using ethanol as a lubricant, in order to minimize surface corrosion. Samples were then polished using colloidal silica (approximately 0.06 µm particle size) in ethanol, on a Struers MD-Chem porous neoprene polishing pad. Specimens examined using optical microscopy were etched by immersing for 30-60 s in an etchant consisting of 10 ml H_2O, 6 g picric acid, 5 ml acetic acid, and 100 ml ethanol to reveal grain and twin boundaries [122].

Alloy grain size was measured using optical microscopy analysis of etched specimens. To estimate alloy grain size, the mean lineal intercepts were measured according to ASTM-E112-10. The average grain diameter was then calculated for each alloy from the lineal intercept value, assuming a tetrakaidecahedral grain shape and log-normal size distribution [123].

3.4.2 Scanning Electron Microscopy

Samples examined by scanning electron microscopy (SEM) were prepared using identical methods as for optical microscopy, as described in section 3.4.1, with the exception that samples were not etched. SEM analysis was conducted to identify the presence of resolvable secondary phases, and to analyze surface topography. Area fractions of secondary phase particles were analyzed using 2-3 images at a magnification of 500X, corresponding to a surface area of approximately 250 x 175 µm per image. Qualitative composition data on the phases present was obtained during SEM analysis by energy dispersive spectroscopy (EDS). SEM observations and EDS measurements were made using a JEOL JSM-6560 operating at 20 kV equipped with an Oxford Instruments Inca 350 microanalysis system.

3.4.3 Transmission Electron Microscopy

Transmission electron microscopy (TEM) was conducted to characterize precipitation and secondary phases in the experimental alloys. TEM foils were first prepared by the conventional grinding of samples using 1200 grit SiC paper and ethanol lubricant, to a thickness of less than 0.060 mm. Small discs of 3 mm diameter were then punched from these thin samples. The discs were further thinned to perforation by electro polishing. Electro polishing was performed using a Stuers Tenupol-5, and a solution of 5.3 g lithium chloride ($LiCl$), 11.16 g magnesium perchlorate ($Mg(ClO_4)_2$), 500 ml methanol, and 100 ml butyl cellosolve at -50°C and 50-90 V [122]. Following electro polishing, ion-milling was performed to remove surface oxide, using a Gatan precision ion polishing system (PIPS) operating at 2.5-3 keV and 4-7° for 0.5-1 h at liquid nitrogen temperatures. Alternatively, instead of electro polishing, some foils were thinned to perforation using only ion-milling, at 3-4.5 keV and 7-10° for 2-4 h at room temperature.

Due to the typical textures formed in many of the experimental alloys, high-resolution TEM (HR-TEM) observation of crystallographic directions parallel to the (0001) basal plane could not be achieved for rolled samples by conventional foil preparation techniques, as high amounts of sample tilt were necessary to align the zone axes. Instead, foils had to be prepared from the normal-transverse plane. This was achieved by first sectioning and grinding samples approximately 1.6 x 0.5 x 0.5 mm in the transverse, normal, and rolling directions respectively. These samples were then ground using an Allied MultiPrep instrument and a 0.5 µm abrasive diamond film through the rolling direction, at an angle of 4° to the transverse direction, to form thin wedges. The foil wedges were then fixed to a 3 mm diameter Mo ring using adhesive, and cleaned by ion-milling using the aforementioned Gatan PIPS system at 2.5-3 keV and 4-7° for 0.5-1 h at liquid nitrogen temperatures.

TEM observations were made using the following instruments and operating voltages: Philips CM12 microscope at 120 kV, JEOL 2010F microscope at 200 kV, and JEOL 3010 microscope at 300 kV. The CM12 and JEOL 2010F were also equipped with an Oxford Instruments Inca microanalysis system, and used for EDS analysis of secondary phases. HR-TEM and high-angle annular dark field scanning TEM (HAADF-STEM) observations were made using an FEI Titan 80-300 LB microscope at 300 kV, and an FEI Titan 80-300 HB microscope at 200 kV. All TEM analysis was performed at the Canadian Centre for Electron Microscopy at McMaster University, except for observations made using the JEOL 3010 which were done at the Université de Grenoble.

3.4.4 Electron Backscatter Diffraction

Electron backscatter diffraction (EBSD) was used to measure alloy texture following rolling and annealing. Samples were prepared along the rolling plane by first mechanical polishing using up to 1 µm diamond abrasive, then electro-polishing using 3% perchloric acid and 97% absolute ethanol at -30°C and 20 V for 2 minutes. EBSD analysis was done at the University of British Columbia, using a Hitachi S579 operating at 20kV, 70° tilt, and 23 mm working distance.

3.4.5 Neutron Diffraction

Neutron diffraction experiments were conducted on samples which had been rolled and annealed, in order to measure alloy texture. To achieve a suitable volume for neutron diffraction measurement, several rolled samples were stacked together (and aligned with a common rolling direction), to make a total volume of approximately 7 x 7 x 7 mm. Measurements were made on the E3 spectrometer of the Canadian Neutron Beam Centre. The neutrons had a nominal wavelength of 2.2 Å. The cross section of the beam was 25.4 x 25.4 mm, allowing the entire volume of each specimen to be sampled. Four pole figures, $(0001)_{Mg}$, $\{10\bar{1}0\}_{Mg}$, $\{10\bar{1}1\}_{Mg}$ and $\{10\bar{1}2\}_{Mg}$, were measured for each sample.

3.4.6 Atom Probe Tomography

Specimens were prepared for atom probe tomography (APT) first by the mechanical grinding of sections of homogenized material into pillars, approximately 0.50 x 0.50 x 10 mm in dimensions. These pillars were then given their respective solutionizing and ageing heat treatments. The heat-treated pillars were subsequently made into fine nano-tipped needles by two-stage electro-polishing [124–126]. The first stage was done by repeatedly dipping one end of the pillar intro a solution of 25% perchloric acid (70%) in glacial acetic acid at 20 V-DC until a point was formed. The point was then refined by the second stage of electro-polishing, which used an electrolyte of 2% perchloric acid in 2-butoxyethanol and a potential of 15-20 V-DC.

APT testing was performed at the University of Sydney Australian Centre for Microscopy and Microanalysis, using an Imago local electrode atom probe LEAP 3000 and LEAP 3000X Si. Testing was performed at a specimen temperature of approximately 20K and under ultrahigh vacuum (~1.0 x10^{-11} Torr). A voltage pulse fraction of 20% was used, along with a target evaporation rate of 1% per pulse. Where composition values are reported, the standard error, s, is estimated using the binomial distribution, such that:

$$s = \sqrt{\frac{C^i(1 - C^i)}{n_T}} \tag{3-1}$$

where C^i is the concentration of solute atoms in a given volume, and n_T is the total number of atoms detected in the volume [124].

3.5 Calorimetry

Differential scanning calorimetry (DSC) tests were performed using a Setaram C80 calorimeter. DSC testing was conducted with an empty reference cell and in an air atmosphere. To create a baseline, tests were conducted on samples of pure Mg. The baseline was run separately to better identify inconsistencies in either the specimen or pure Mg tests. To minimize any discrepancies between samples and the pure Mg baselines, all samples were prepared with approximately equal dimensions of 8 x 10 x 15 mm and 2200 mg mass, unless otherwise specified.

All DSC data was normalized by dividing the heat flow measurements by the sample mass. The results for the baselines were then subtracted from the results for the alloys to obtain the final DSC curves. Tests were conducted from room temperature to 300°C using a heating rate of 0.5°C / min.

3.6 Thermodynamic Calculations

Thermodynamic analysis of equilibrium phases was done using the FactSage 6.3 software package [127]. The FT-Lite and VLGM materials databases were used for the calculations. To evaluate the supersaturations for the solutes in the alloys, the supersaturation value was calculated as $\Delta X = X_{\mathrm{soln}} - X_{\mathrm{e}}$, where X_{soln} is the atomic fraction of a given solute element dissolved in the HCP-Mg solid solution at the solutionizing temperature, and X_{e} is the equilibrium solubility for that element at the ageing temperature [128].

3.7 Acknowledgement of Assistance with Experiments

The materials and experiments detailed in this work have partly come about through the contributions and assistance of others.

The high-Ca group A alloys were cast and provided by Dr. Daryoush Emadi through the CanmetMATERIALS academic user access facility (AUAF) program. The group B alloys and pure materials utilized for creating the group B alloys were provided by the Natural Sciences and Engineering Research Council of Canada Magnesium Network Program (MagNET). Casting of the group C experimental alloys was performed with Martin Van Oosten and Dr. Hatem Zurob, with Jim Garrett assisting in creating the master alloys. Dr. Xiaogang Li performed ICP analysis to measure the compositions of the cast materials. HR-TEM and HAADF-STEM observations were performed with the invaluable assistance and expertise of Dr. Andreas Korinek. Conventional TEM observations using the JEOL 2010F were performed with the assistance of Dr. Carmen Andrei. Assistance with TEM specimen preparation was provided by Wen He Gong. Dr. Yuquan Ding provided assistance with SEM operation. Training with the FactSage thermodynamics software was provided by Dr. Aimen Gheribi, and Dr. Youn-Bae Kang.

A number of collaborators have contributed directly to specific microstructural characterization results and have been acknowledged throughout the thesis where those results are reported.

4 Precipitation and Phase Evolution in Mg-Zn-Ca Alloys with High-Ca Content

This chapter presents the results of investigations on the precipitation hardening behaviour of the group A alloys. The majority of this chapter has already been published in Materials Science and Engineering A (B. Langelier, X. Wang, S. Esmaeili, *Evolution of precipitation during non-isothermal ageing of an Mg–Ca–Zn alloy with high Ca content*, Materials Science and Engineering A, 538 (2012) p. 246-251).

4.1 Introduction

Many studies from literature regarding the precipitation hardening behaviour in the Mg-Zn-Ca alloy system have focused on alloys with low amounts of Ca (< 1wt%). However, there are many additional benefits to magnesium alloys with relatively high Ca content (1-3wt%), including significant reduction in flammability and improvement in the oxidation and creep resistance [11,54,56,129]. Furthermore, Mg-Ca and Mg-Zn-Ca alloys are also of interest as biomaterials, both for use as biodegradable implants due to their corrosion characteristics, and the biocompatibility of magnesium and the alloying elements used [57,58,130,131]. An Mg-Zn-Ca alloy with a high amount of Ca may provide significant precipitation hardening, as well as the extra benefits of additional Ca content for future biomaterials applications. The focus of this chapter is the study of the evolution of precipitation in an Mg-Zn-Ca alloy with a high Ca:Zn ratio through the combined use of DSC, hardness testing, TEM, and thermodynamic considerations.

4.2 Experimental Methodology

The alloys studied in this work are described in section 3.1, and the homogenizing/solutionizing heat treatments performed on them are detailed in section 3.2. Following the solutionizing heat treatment and water-quenching, the samples were immediately age-hardened or tested using DSC according to the specifications given in section 3.5. Isothermal ageing was done at 200°C for times ranging from 0 to 7 hours. Other samples were aged with a ramped-temperature heat treatment to simulate conditions during DSC testing. These samples were heated from room temperature to 300°C at a rate of 0.5°C/min, and water-quenched at set temperature intervals. Samples used for TEM investigation were heated using this ramped-ageing heat treatment to 210°C, 250°C, and 300°C. All other experimental procedures, including hardness testing and TEM sample preparation and analysis, are described in the respective sections of chapter 3.

4.3 Results and Discussion

4.3.1 Isothermal Ageing of XZ21 and XZ22 Alloys

The results of hardness measurements for isothermal ageing are shown in Figure 4-1. There is little measurable increase in hardness for the binary X2 sample. However, a significant improvement in hardening is observed for the samples alloyed with Zn. The highest hardness is achieved in the XZ21 sample after approximately 1 hour of ageing. The additional Zn content over 1wt% does not appear to provide any additional benefit to hardening, as the XZ22 alloy exhibits a lower peak-aged hardness than the XZ21 alloy. Note that while binary Mg-(1,2)Zn (wt%) alloys are not tested here, the Mg-Zn phase diagram shows those alloys to exist as a single HCP-Mg phase at 200°C, and therefore no precipitation hardening is expected.

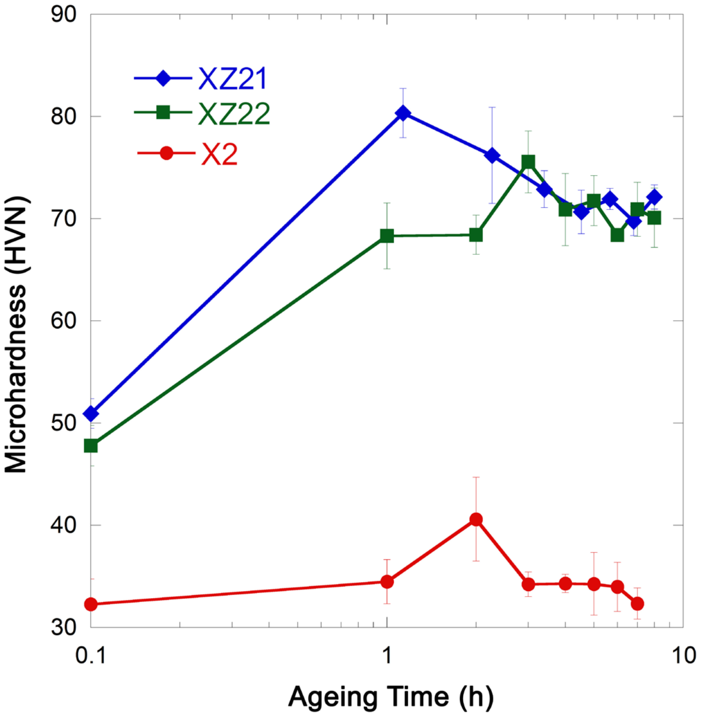

Figure 4-1: Isothermal age-hardening curves for Mg-Zn-Ca alloys aged at 200°C.

The differences in hardening between the binary and ternary alloys can be explained by TEM analysis, which shows a large difference between the size and number density of precipitates formed (Figure 4-2), which is due to the presence of Zn.

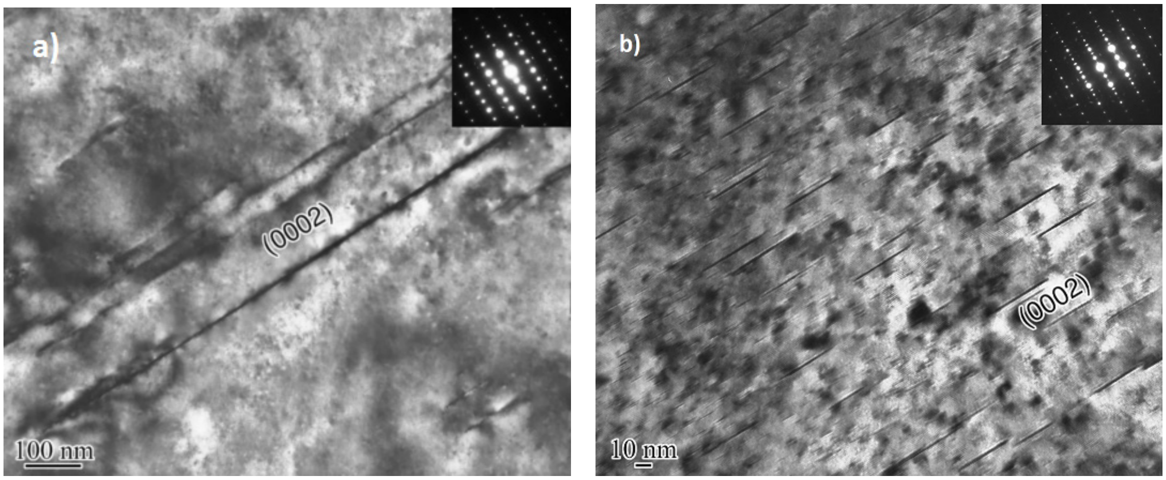

Figure 4-2: TEM micrographs of a) X2 b) XZ21 aged isothermally at 220°C for 1 hour. Electron beam parallel to $\langle 11\bar{2}0 \rangle$ zone axis. Observations performed by V.Y. Gertsman [132].

The higher hardening response of the XZ21 alloy compared to the XZ22 alloy can be understood by examining the Mg-Zn-Ca isopleth phase diagram shown in Figure 4-3. It can be seen in Figure 4-3 that there exists a temperature-composition region where only α-Mg and Mg_2Ca exist at equilibrium for the XZ21 alloy. In contrast, no temperature exists for the XZ22 alloy where Zn is entirely solutionized in the solid state. This explains how Zn content in excess of maximum solubility can hinder the effectiveness of solutionizing, and therefore of precipitation hardening for the XZ21 alloy. The presence of Zn-containing phases during solutionizing could also further hinder precipitation hardening by affecting how the precipitate phases nucleate and grow during ageing. The XZ21 alloy was chosen for further DSC and TEM analysis due to the preferable hardening performance over the XZ22 alloy.

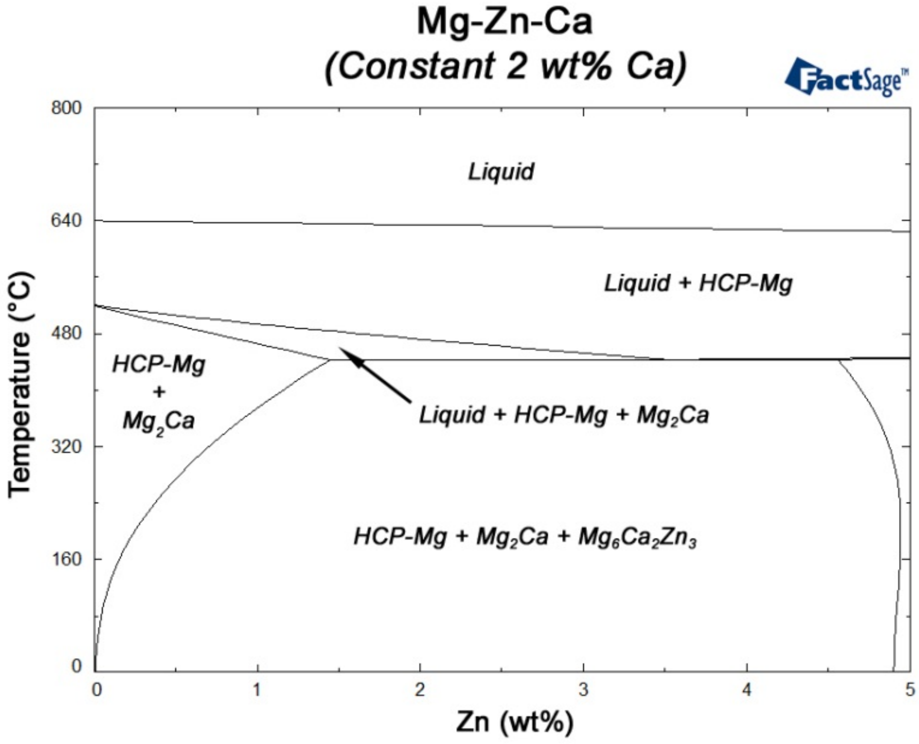

Figure 4-3: FactSage [127] isopleth phase diagram for Mg-Zn with constant 2wt% Ca.

4.3.2 Experimental Analysis of Precipitate Evolution in XZ21

The DSC result on the as-quenched sample and the corresponding hardness evolution curves are shown in Figure 4-4. This shows the progression of precipitation during non-isothermal ageing, with each peak representing a precipitation event. For the sake of comparison, hardness results during the non-isothermal ageing heat treatment are shown in Figure 4-4 as well. Three major exothermic peaks, designated as peaks I, II and III, are observed on the DSC trace. The appearance of each individual peak attests to an overlapping nature of the precipitation events that are associated with the peak. Examining the hardening profile shows that there is no significant hardness increase during the temperature range associated with Peak I (50-160°C). However, Peak II, which is centered at 200°C, coincides with a large increase in the hardness. The maximum value of hardness (i.e. the peak-aged condition), corresponds to the end temperature for this peak (~ 235°C). Peak III occurs in the temperature range of 235-300°C which matches the hardness reduction, suggesting that the precipitation during this peak corresponds with an over-aging process.

From the DSC results, it can be seen that 210°C corresponds with the end of the main sub-peak within peak II (i.e. the start of a shoulder to peak II), while 250°C and 300°C correspond to the initiation and completion of the main segment of peak III. Hence, TEM tests on samples heated to 210°C, 250°C and 300°C, which correlate to slightly under-aged, slightly over-aged and heavily over-aged conditions, respectively, shed light on the microstructural evolution associated with these important stages of the alloy’s precipitation evolution.

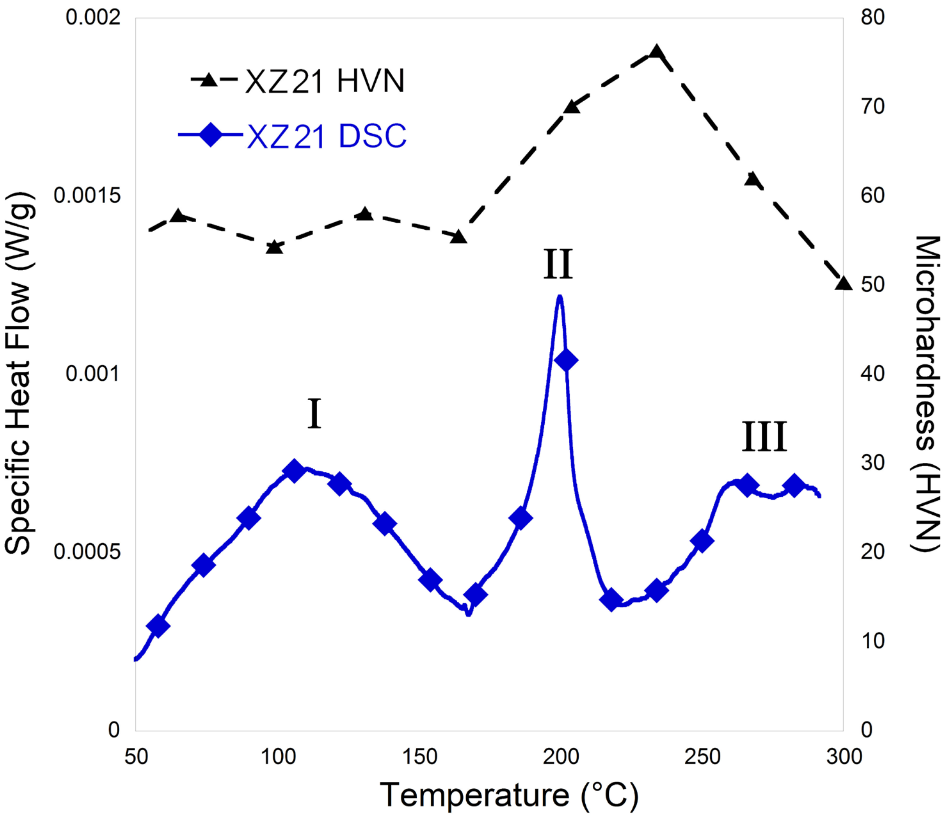

Figure 4-4: Hardness evolution during non-isothermal ageing at 0.5°C/min and DSC results for as-quenched XZ21 alloy.

The TEM analysis of the sample aged to 210°C generally revealed no visible precipitates. No reflections from precipitates were observed in the selected area diffraction patterns (SADP) either. The significant hardening that occurs when the alloy is aged to 210°C suggests that very fine GP zones, unresolvable with the conventional TEM used for this analysis, form at this aging condition. Previous studies of isothermally-aged Mg-0.5Ca-0.8Zn (wt%) [10] and Mg-0.5Ca-1.6Zn (wt%) [11] have identified very fine GP zones during the early stages of ageing, and up to the peak-aged condition. The formation of these GP zones, which are associated with hardening in those alloys, has been attributed to the presence of both Ca and Zn elements [11].

TEM analysis of the sample aged to 250°C shows evidence for four types of precipitates. A dotty contrast is visible, due to the presence of fine unidentified nanoscale precipitates. There are also numerous small plate-shaped precipitates (Figure 4-5a, b), very large plates (Figure 4-5c, indicated by arrows) and occasional large blocky precipitates (Figure 4-5d). Streaks along the [0001] direction at $1/3\{11\bar{2}0\}$ and $2/3\{11\bar{2}0\}$ in the $\langle 10\bar{1}0\rangle$ zone axis SADP are observed (Figure 4-5a SADP). There are also low intensity streaks parallel to the [0001] direction in the $\langle 11\bar{2}0\rangle$ SADP (Figure 4-5b SADP). The fine basal plate precipitates resemble the precipitates observed by Oh et al. [52] in an isothermally-aged Mg-0.5Ca-0.8Zn (wt%) alloy. Oh et al. [52] have also observed the corresponding streaking along the [0001] direction at $1/3\{11\bar{2}0\}$ and $2/3\{11\bar{2}0\}$ in the $\langle 10\bar{1}0\rangle$ SADP. These streaks were attributed by Oh et al. to internal ordering of the basal plate precipitates [52]. Similar streaks were also attributed by Oh-ishi et al. [53] to ordered GP zones. The structure of these ordered GP zones was first described in detail by Ping et al. [97] for an Mg-RE-Zn-Zr alloy, and later for the Mg-Ca-Zn system by Oh-ishi et al. [53]. It is therefore likely that the fine basal plates observed at 250°C represent coarsened GP zones, which had previously formed and had provided the hardening observed at 210°C. They are also responsible for the streaking in the SADPs in Figure 4-5a-b, as the GP zones coarsened and gained internal ordering. The large, coarse plates observed in the XZ21 alloy (Figure 4-5c) match the morphology of the coarse plates observed in an isothermally-aged X2 alloy (Figure 4-2a) In that binary alloy, those large plates were identified by SADP to be Mg_2Ca [132], suggesting that these large plates in the XZ21 alloy (Figure 4-5c) are also a form of Mg_2Ca.

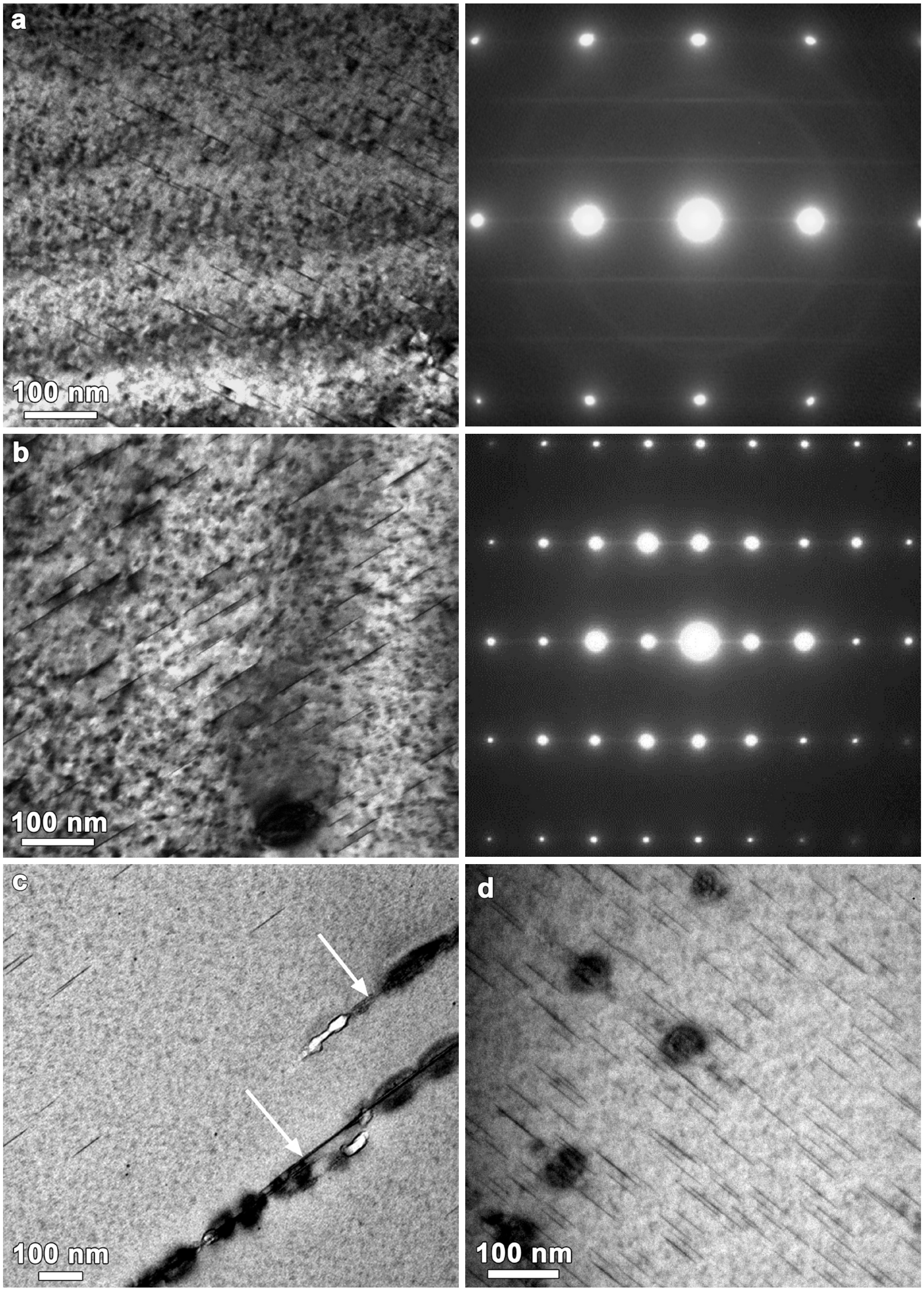

Figure 4-5: TEM image of XZ21 alloy non-isothermally aged to 250°C with corresponding SADPs along a) $\langle 10\bar{1}0\rangle$ zone axis, b) $\langle 11\bar{2}0\rangle$ zone axis, and c) TEM image of large plate precipitates d) large blocky precipitates with SADPs $\langle 11\bar{2}0\rangle$ zone axes. Observations performed by X. Wang.

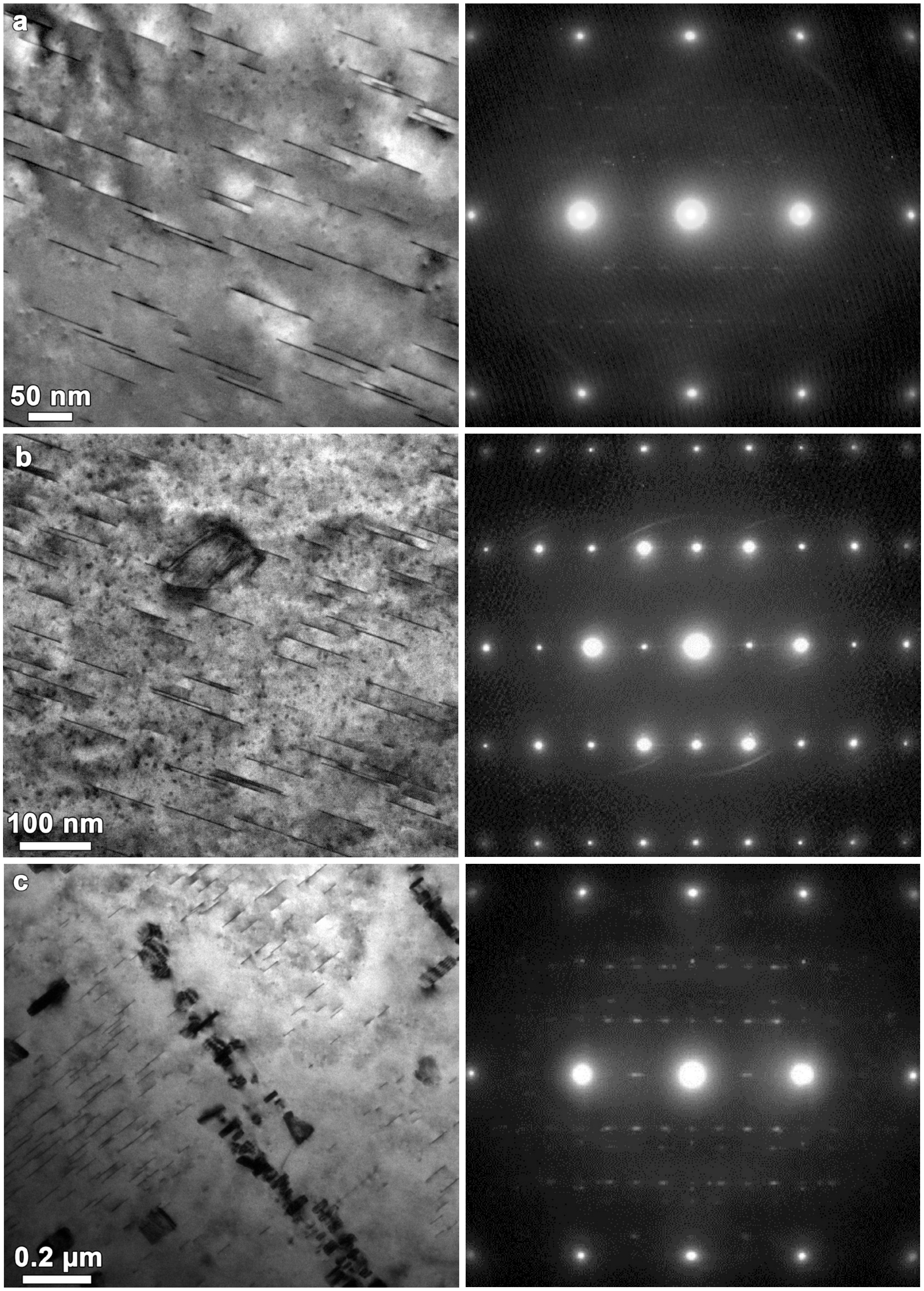

Figure 4-6: TEM images of XZ21 alloy non-isothermally aged to 300°C with corresponding SADPs along a) $\langle 10\bar{1}0 \rangle$ zone axis, b) $\langle 11\bar{2}0 \rangle$ zone axis, and c) $\langle 10\bar{1}0 \rangle$ zone axis. Observations performed by X. Wang.

Figure 4-6 shows the TEM results for the XZ21 alloy non-isothermally aged to 300°C. The precipitates found in this condition consist of fine basal plates and the unidentified nanoscale precipitates (Figure 4-6a, b). Large blocky precipitates are also commonly observed (Figure 4-6c), and the large basal plates seen in the previous ageing condition are noted to persist to this temperature (not shown). The SADP images for the alloy aged to 300°C show that the streaking seen for the $\langle 10\bar{1}0\rangle$ SADP in Figure 4-5a has become weak and non-continuous for this aging condition, as seen in Figure 4-6a. The streaking observed along the [0001] direction for the $\langle 11\bar{2}0\rangle$ in Figure 4-5b has also become weaker and shorter for the sample aged to 300°C, as seen in Fig. 3b. With the selected area aperture focused on the large blocky precipitates, extra reflections are observed in the SADP (Figure 4-6c). These extra reflections identify the blocky precipitates as Mg_2Ca, with an orientation relationship of $[01\bar{1}0]_{Mg} \parallel [\bar{1}2\bar{1}0]_{Mg2Ca}$, $(0001)_{Mg} \parallel (0001)_{Mg2Ca}$. EDS analysis was performed on the Mg_2Ca precipitates, which indicated the presence of Zn in these phases. This finding is consistent with earlier reports from literature [52].

A qualitative comparison of the TEM results and hardness data for the samples aged to 250°C and 300°C provides insight into the overall changes in the precipitation state when the temperature is increased. The fine basal plates, present in both conditions, appear to be slightly larger for the sample aged to 300°C. The dotty contrast due to the unidentified nanoscale precipitates is also less visible in the sample aged to 300°C, suggesting a decrease in number density. Conversely, the blocky Mg_2Ca precipitates which were found occasionally for the sample aged to 250°C, increase in number density for the 300°C sample. The decrease in appearance of the nanoscale precipitates and apparent increase of blocky Mg_2Ca precipitates over this temperature interval corresponds with the decrease in hardness of the alloy, i.e. over-aging of the alloy towards the formation of equilibrium phases (Figure 4-4).

4.3.3 De-convolution of DSC Data for Precipitate Evolution in XZ21

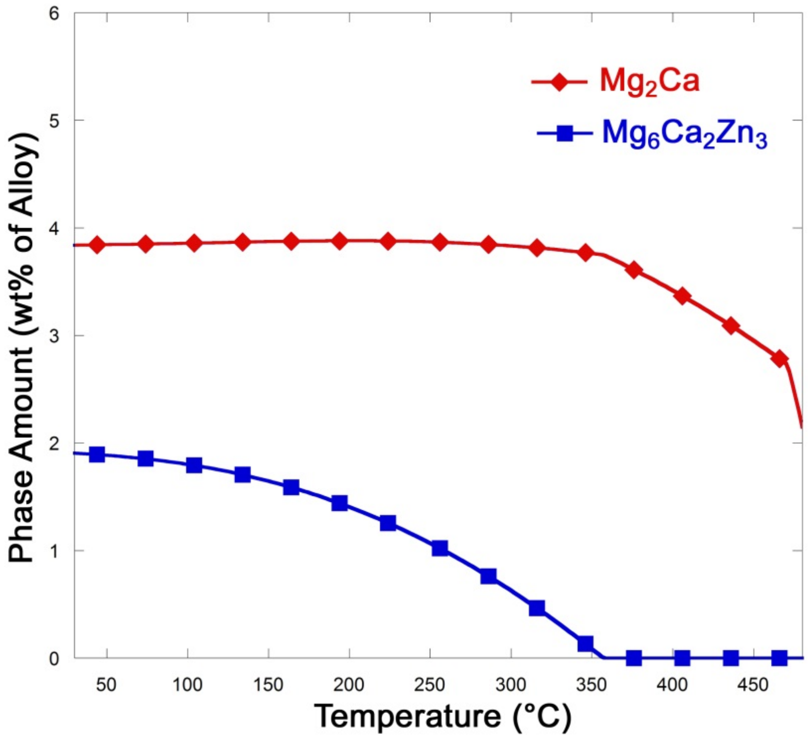

Figure 4-7: Calculated equilibrium secondary phase content for XZ21 alloy

The appearance of the overlapping-natured DSC peaks and the corresponding TEM results suggest that a successive precipitation process, involving the formation/transformation of multiple phases, occurs during ageing of the XZ21 alloy. The precipitation evolution in this alloy is analyzed by first considering the thermodynamic stability of phases as a function of temperature using FactSage thermodynamic calculations. As shown in Figure 4-6, Mg_2Ca and $Mg_6Ca_2Zn_3$ are the equilibrium phases for the XZ21 alloy.

The high Ca content of the alloy causes the Mg_2Ca phase to be stable in equilibrium at all temperatures over the range investigated. However, the results shown in Figure 4-6 reveal that the amount of Mg_2Ca remains nearly constant for temperatures below about 350°C. On the other hand, the $Mg_6Ca_2Zn_3$ phase, which is present in significant quantities at low temperatures, is unstable above 357°C. These results suggest that ageing the XZ21 alloy for a sufficiently long time at a temperature above 357°C to achieve the equilibrium state will dissolve any $Mg_6Ca_2Zn_3$ phase or it's precursors that exist, while a significant quantity of Mg_2Ca phase will form and remain in the microstructure. The resulting microstructure will have the capability to form further precipitates during any subsequent aging at lower temperatures due to the presence of the dissolved solutes. However, these precipitates will not include any significant level of Mg_2Ca due to the fact that this phase will already be present at levels close to its maximum in the alloy. Accordingly, an aging treatment was done on a solutionized alloy sample by heating it for 24 hours at 370°C. The sample was subsequently water-quenched and DSC tested. The result of the DSC test on this sample is shown in Figure 4-8. The differences between the DSC results for the as-quenched and aged samples can also be analyzed by subtracting the DSC trace for the aged sample from the as-quenched sample. The resultant subtracted trace is also shown in Figure 4-8. These differences are due to the difference in the precipitation processes involved. While the as-quenched sample's trace represents precipitation involving the sequence of formation towards both Mg_2Ca and $Mg_6Ca_2Zn_3$ equilibrium phases, the thermodynamic analysis predicts that the aged alloy represents only the precipitate evolution that occurs in the sequence of formation towards the $Mg_6Ca_2Zn_3$ equilibrium phase. Accordingly, it is suggested that the subtracted result should mainly represent Mg_2Ca formation.

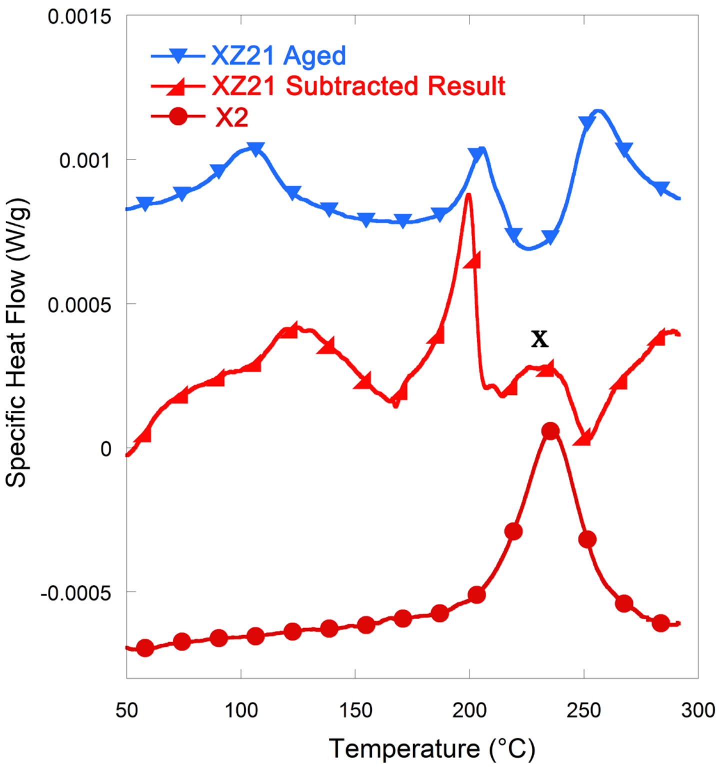

Figure 4-8: DSC results for XZ21 alloy given a high-temperature ageing heat treatment, and the results of subtracting this data from the as-quenched DSC trace. DSC result for the binary X2 alloy is also presented for comparison. Note that curves are shifted along y-axis for ease of visualization, and axis values are given only for the purpose of scale.

The DSC trace for the aged sample shows three major exothermic peaks, while the subtracted trace clearly reveals the overlapping natures of peaks I, II and III. The first two exothermic peaks are centered at approximately the same respective temperatures as peaks I and II for the as-quenched sample. Peak I is considered to represent early stage decomposition of the solid solution for both the as-quenched and aged alloys. Hardening results suggest that peak II represents the formation of very fine GP zones/precipitates, which are observable by TEM when they coarsen to the fine basal plates shown in Fig. 2a-d, and are marked by streaks in the corresponding SADPs.

The presence of a new exothermic peak in the subtracted result (i.e. peak x in Figure 4-8) suggests that an exothermic event occurs in the approximate temperature range of 220°C to 250°C during testing of the as-quenched sample. It is speculated that this event is hidden on the trace for the as-quenched sample due to the overlapping effects from concurrent endothermic and exothermic processes. Since this peak only appears in the DSC trace of the subtracted result it is expected to primarily represent Mg_2Ca formation, likely in the form of the large coarse plate precipitates (Figure 4-5c). This is supported by observations that the location of peak x coincides with the single exothermic peak of the binary X2 alloy. The overlapping endothermic peak which has obscured peak x is likely caused by the temperature of the DSC test passing the GP zone solvus temperature.

The third exothermic peak in the as-quenched sample's DSC result is seen to be a double-peak, composed of the two sub-peaks observed over the similar temperature range in the DSC traces for the aged and subtracted results. The first part of the double peak exists in the aged alloy result, and may represent the formation of some $Mg_6Ca_2Zn_3$ equilibrium phase. However, TEM analysis could not confirm the presence of $Mg_6Ca_2Zn_3$ phase for the non-isothermal ageing tests examined in this work. It is expected that the formation of this phase would occur with extended ageing, as predicted by the thermodynamic analysis. The second part of the double peak exists in the subtracted result, which is associated with Mg_2Ca evolution. Therefore, the large blocky Mg_2Ca precipitates commonly observed in the microstructure at higher ageing temperatures (Figure 4-5d, Figure 4-6c) are attributed to this part of peak III. The unidentified nanoscale precipitates, which provide a fine dotty contrast to TEM images (Figure 4-5a, b), are noted by TEM observations to decrease in number density with increasing temperature. It is therefore possible that by transformation or dissolution as temperature increases, these precipitates contribute to the formation of the Mg_2Ca phase in the second part of peak III.

4.4 Summary

The precipitation hardening behaviour of Mg-Zn-Ca alloys XZ21 and XZ22 is investigated and compared to the behaviour of Mg-Ca alloy X2. It is found that Zn improved the precipitation hardening effect dramatically compared to the binary X2 alloy. This is due to the formation of new precipitate phases with a refined distribution. However, a higher amount of Zn in the XZ22 alloy is not found to provide additional benefit due to surpassing the solid solubility limit.

DSC analysis, combined with TEM, hardness measurement, and thermodynamic analysis reveals the precipitation evolution for the XZ21 alloy, aged non-isothermally to 300°C. Early decomposition of the solid solution is observed in the DSC at low temperatures, with no apparent effect on hardening. Fine GP zones then form which serve to harden the alloy to the peak-aged condition. With a continued increase in the ageing temperature, the GP zones evolve to fine basal plates. Large basal plates also form, which are suggested by the results of DSC and thermodynamic calculations to be an Mg_2Ca type of precipitate. Further ageing leads to the formation of unidentified nanoscale precipitates. These precipitates begin to disappear with extensive over-ageing. Blocky precipitates, identified by SADP to be equilibrium Mg_2Ca, are formed in the highly over-aged sample. No evidence for the presence of the $Mg_6Ca_2Zn_3$ equilibrium phase is found in this alloy during the non-isothermal heat treatment performed in this work.

5 Effects of Ce Additions on the Precipitation Hardening of Mg-Zn Alloys

This chapter reports on the investigation of the precipitation hardening behaviour of the Mg-Zn system with alloying/microalloying additions of only Ce. The age-hardening responses of alloys with various Zn and Ce content are measured, and analyzed using TEM and thermodynamic calculations.

5.1 Introduction

The majority of recent research on magnesium alloys has been focused on improving the generally poor mechanical properties of magnesium, specifically the alloy ductility/formability and strength. A promising method of alloy design, noted to improve the formability of magnesium alloys, is the addition of rare earth elements, which act primarily by promoting a random alloy texture following bulk deformation [3,14,69,70,74,111]. Among the rare earth elements, Ce is noted to be particularly potent at modifying texture and enhancing ductility, which makes it a desirable choice for alloying with magnesium [69,74]. However, the design of alloys that utilize rare earths for the texture effect must still consider material strength. Among magnesium alloys that have recently been the focus of extensive metallurgical analysis, Mg-Zn alloys have shown that significant strengthening can be achieved by precipitation hardening [18,19,21,42,90]. While the effects on ductility and texture modification resulting from the addition of Ce to Mg-Zn based alloys have been reported in literature [66,73,105,117–119], the effects of Ce additions on the precipitation hardening response of Mg-Zn alloys are yet to be established. In this work, the effects of Ce in both microalloying (<0.5 wt%) and alloying levels, on the precipitation hardening responses of Mg-Zn alloys are evaluated. The precipitation hardening behaviour is investigated through microhardness measurement, TEM observation, and thermodynamic analysis, which relate the alloy chemistry to the phase transformation and hardening behaviour.

5.2 Experimental Methodology

The alloys analyzed in this section are from the Mg-Zn-(Ce) system, and contain 2 or 4 wt% Zn, and 0, 0.1, or 1.0 wt% Ce (i.e. group B alloys and most of group C from Table 3-1). Exact material details are given in section 3.1. These alloys were heat treated according to the homogenizing and solutionizing treatments described in section 3.2. No rolling operations were performed prior to solutionizing. Following water-quenching from the solutionizing heat treatment, the alloys were aged at 100°C for times ranging up to 240 h. This ageing temperature was selected so as to be below the relatively low solvus temperature for 2 wt% Zn in the binary Mg-Zn system (calculated to be 150°C). Hardness measurement, TEM analysis, and thermodynamic calculation of solute supersaturations were conducted as per the descriptions given in sections 3.3.1, 3.4.3, and 3.6 respectively.

5.3 Results

Hardness measurements on the alloys in the as-quenched condition showed that the Z2 and ZE20 alloys have an initial hardness of approximately 40 HVN, while the Z4, ZE40, ZE21 and ZE41 alloys all have a higher as-quenched hardness of approximately 48 HVN. Due to variability in the initial microstructures, the precipitation hardening capabilities of the alloys are analyzed by comparing the age hardening responses (i.e. the increase in hardness from the as-quenched condition). The age hardening responses for 100°C ageing are shown for the alloys with 2 wt% Zn and 4 wt% Zn in Figure 5-1a & b, respectively. For every alloy, the hardening response can be seen to increase with ageing time. After 168 h of ageing, the response of the Z2, ZE20, and ZE21 alloys all begin to decrease. In the cases of the Z4 and ZE40 alloys, a clear hardening response plateau appears after 168 h of aging. Although the hardening response of the ZE41 alloy appears to continuously increase beyond 168 h of aging considering the average hardness values, the error bars may suggest a potential hardness plateau between 168 and 240 h of aging. Given the general similarity between the alloys in achieving a peak or a plateau in hardness level after 168 h of ageing, this ageing time is referred to as the peak-ageing condition for the alloys in this chapter and used for comparison.

From the different hardening behaviours of the alloys, it is seen that the addition of Ce does not appear to enhance the hardening response of the corresponding binary Mg-Zn alloys in the peak-aged condition. In fact, both ZE20 and ZE21 show a decreased hardening response compared to Z2 over all the ageing times investigated. While the hardening response of ZE40 is roughly equal to that of Z4, a lower hardening response in the peak-aged condition is observed for ZE41. Increasing the Zn concentration generally increases the hardening response in the peak-aged condition. In that regard, a slight increase is observed for the binary alloy Z4, and ZE41 over those of Z2 and ZE21, while a significant increase is achieved for the ZE40 alloy compared to ZE20.

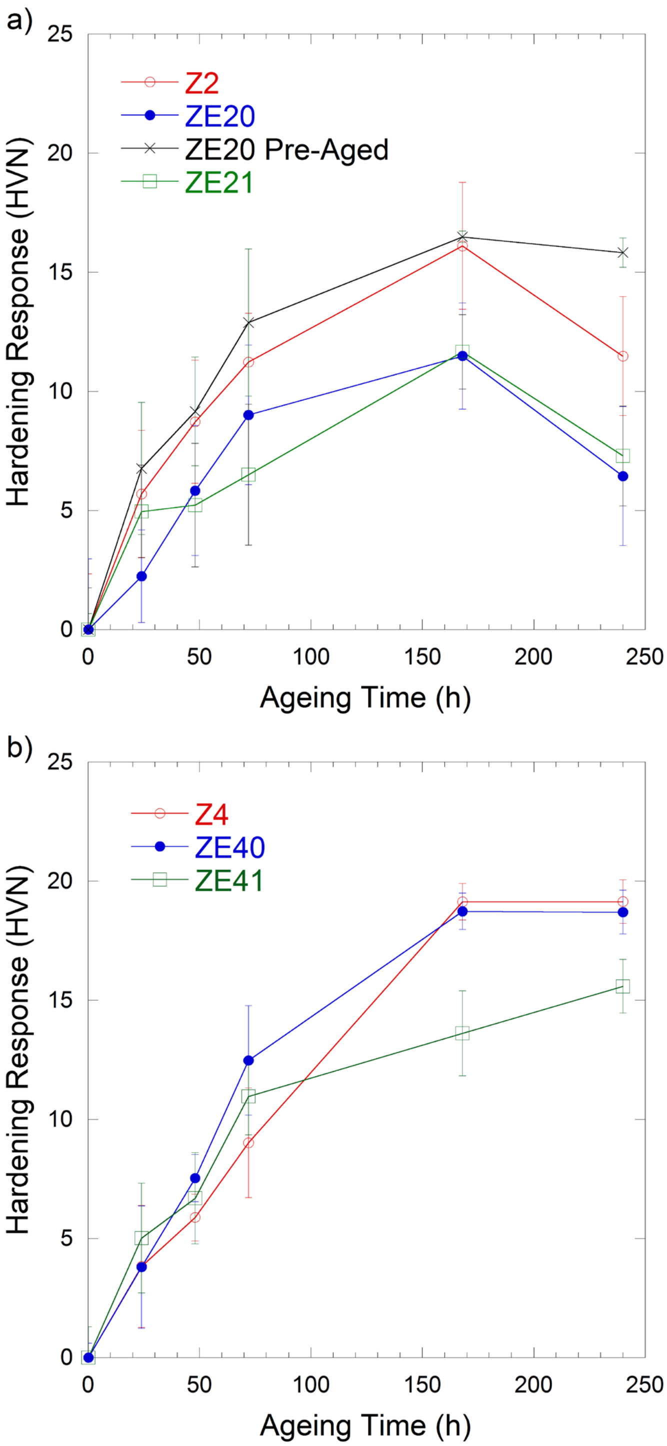

Figure 5-1: Age-hardening responses of Mg-Zn-(Ce) alloys aged at 100°C with a) 2 wt% Zn, and b) 4 wt% Zn.

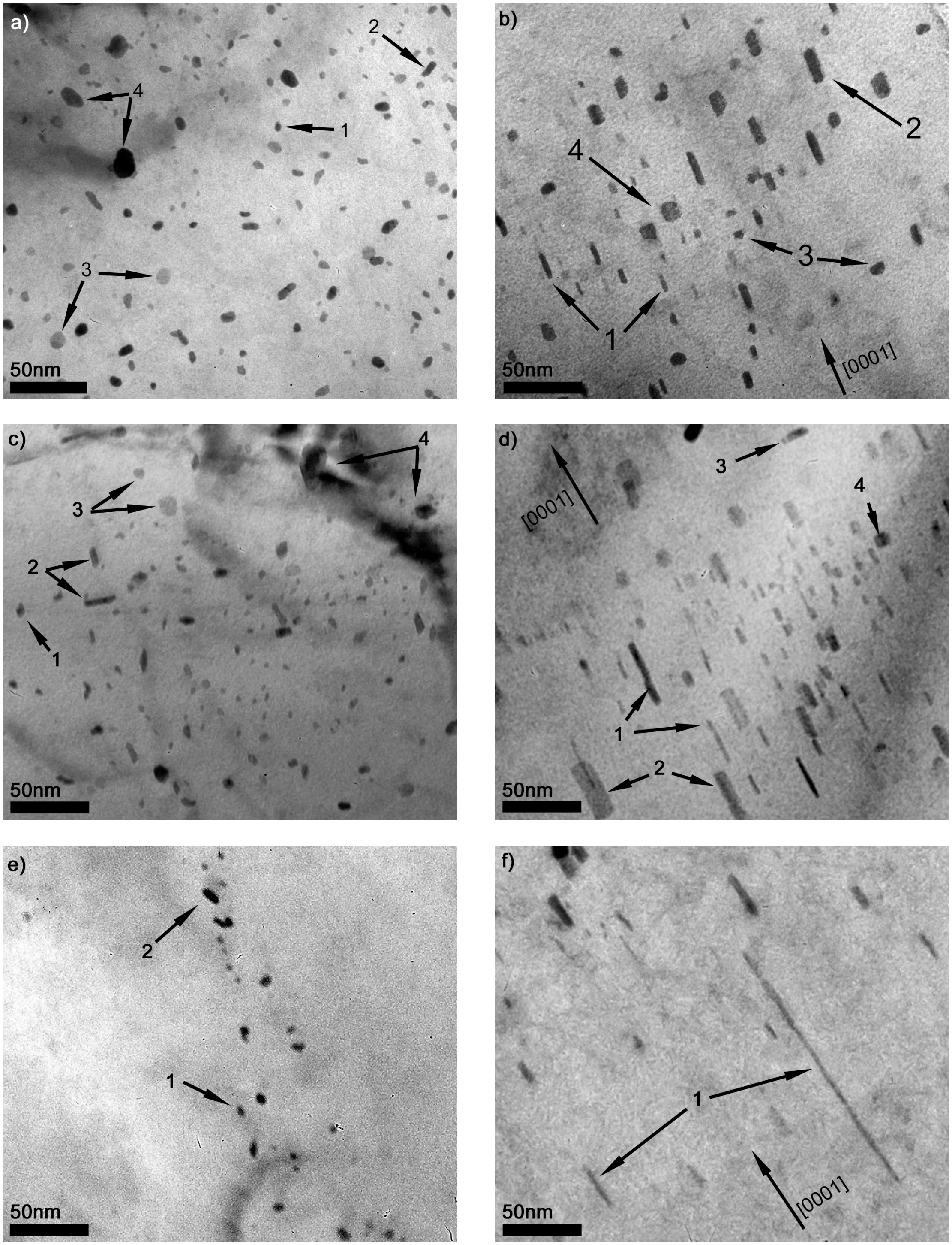

Figure 5-2: Bright-field TEM micrographs of a,b) Z4, c,d) ZE40, and e,f) ZE41 alloys aged 168 h at 100°C, a,c,e) [0001] zone axis, b,d,f) near $\langle 11\bar{2}0 \rangle$ zone axis, with [0001] direction indicated on the images. Precipitates identified with numbers assigned in the text.

TEM analysis of the microstructures following 168 h of ageing at 100°C reveals similar precipitates for all the alloys examined, varying only in apparent number density. Typical TEM images of the precipitates are shown for the 4 wt% Zn alloys in Figure 5-2. The precipitates observed in the microstructures are found to consist mainly of 1) rods parallel to the [0001] direction, 2) lathes with their long axes parallel to the [0001] direction, 3) plates parallel to the basal plane, 4) small blocky/irregular-shaped precipitates. These precipitates are indicated on the micrographs shown in Figure 5-2 according to the numbers given above. The c-axis rods are found to be 15-150 nm in length and 3-20 nm in width. The lathes closely resemble the rods as they are also elongated parallel to the c-axis, ranging from 15-50 nm in length. However, whereas along the basal plane the cross section widths of the rods are close to identical, the lathes extend along the $\langle 11\bar{2}0\rangle$ and $\langle 10\bar{1}0\rangle$ matrix directions. This gives them a cross section width of close to 5 nm in one direction, and 15-25 nm in the other. The basal plates are generally 5-20 nm in width along the basal plane, and about 3-5 nm thick in the [0001] direction. The blocky/irregular precipitates are generally cuboidal or rounded in shape and about 10-30 nm in every dimension. It should be noted however that these precipitates have not been distinguished as clearly separate from the c-axis rod precipitates or basal plates, and may just be particularly thick, short variants of these precipitates with an aspect ratio ~1 in the cross-section. The c-axis rods and basal plate precipitates are by far the most commonly observed in the aged microstructures. The lathes and blocky/irregular precipitates are found only occasionally throughout the matrix.

Comparing between the alloys, it is noted that the number densities of precipitates found in the aged microstructures appear to be approximately proportional to the hardening responses in the peak-aged condition. The lowest precipitate number density among the alloys shown in Figure

5-2 is clearly for the ZE41 alloy (Figure 5-2e), which also exhibits the lowest hardening response among those same alloys after 168 h of ageing. However, it should be noted that the distributions of the precipitates observed in all the alloys examined are generally non-uniform, with many precipitates formed on dislocations. The non-uniformity of the precipitate distributions appears to be further increased in the Ce-containing alloys, as evident in Figure 5-2e.

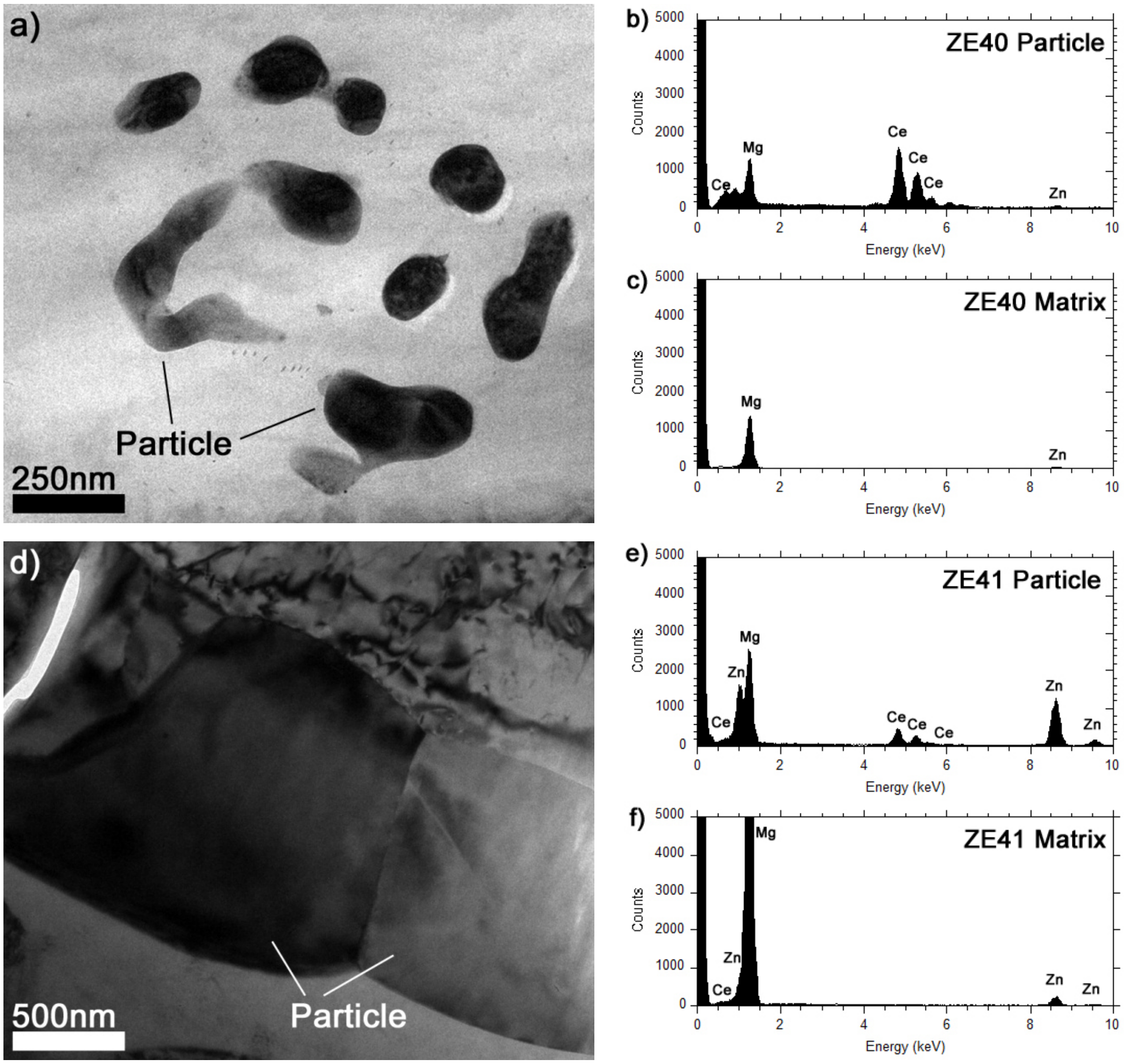

Figure 5-3: Bright field TEM micrographs showing large particles in a) ZE40 and d) ZE41 aged 168 h at 100°C, and corresponding EDS spectra for the matrix and particles in the ZE40 (b, c) and ZE41 (e, f) alloys.

In addition to the fine precipitates presented in Figure 5-2, coarse particles containing Ce are found in all the ternary Mg-Zn-Ce alloys as well, with typical examples shown for ZE40 and ZE41 in Figure 5-3a and d, respectively. In the microalloyed samples, these particles are generally observed in clusters (such as shown in Figure 5-3a). EDS analysis shows that along with being enriched in Ce, these particles also contain some Zn. The highest amount of these particles were observed for the alloys containing 1 wt% Ce.

5.4 Discussion

The trends observed from the hardening results in this work show that the addition of Ce is not beneficial for the precipitation hardening of Mg-Zn alloys, and may even lead to a reduction in the age hardening response. This effect can be understood by considering the origin of the hardening response of the alloys, and how that is affected by the presence of Ce.

The increase in strength due to the presence of precipitates in an age hardened alloy is inversely-proportional to the inter-particle spacing on the slip plane [29,76,77]. Therefore, higher hardening will be achieved by higher number densities of precipitates. Given the natural anisotropy of slip in HCP magnesium alloys, the orientation and morphology (i.e. aspect ratio) of the precipitates may also significantly influence the effective inter-particle spacing along a given slip plane [81,82]. Additionally, the uniformity of the precipitate distribution will also be an important factor in dictating the effective inter-particle spacing, and therefore the strengthening achieved by precipitation. In the current alloys, ageing at 100°C results in the formation of fine-scale precipitates in combinations of morphologies and orientations that are common between the alloys. Based on the relative numbers of these precipitates, the c-axis rods, with similar characteristics as the well-known Mg-Zn type β_1' precipitates [18,42], and potentially the lathes and basal plates, similar in characteristics to Mg-

Zn type β_2' precipitates [42], are most likely to impact hardness. Therefore, as the characteristics of the precipitates themselves do not change between the alloys, the relative hardening behaviours of the alloys can be attributed to different precipitate number densities, and the relative uniformity in distribution of the precipitates. The negative effects of Ce on hardening appear to originate by adversely affecting both of these microstructural characteristics, as evident from TEM observations.

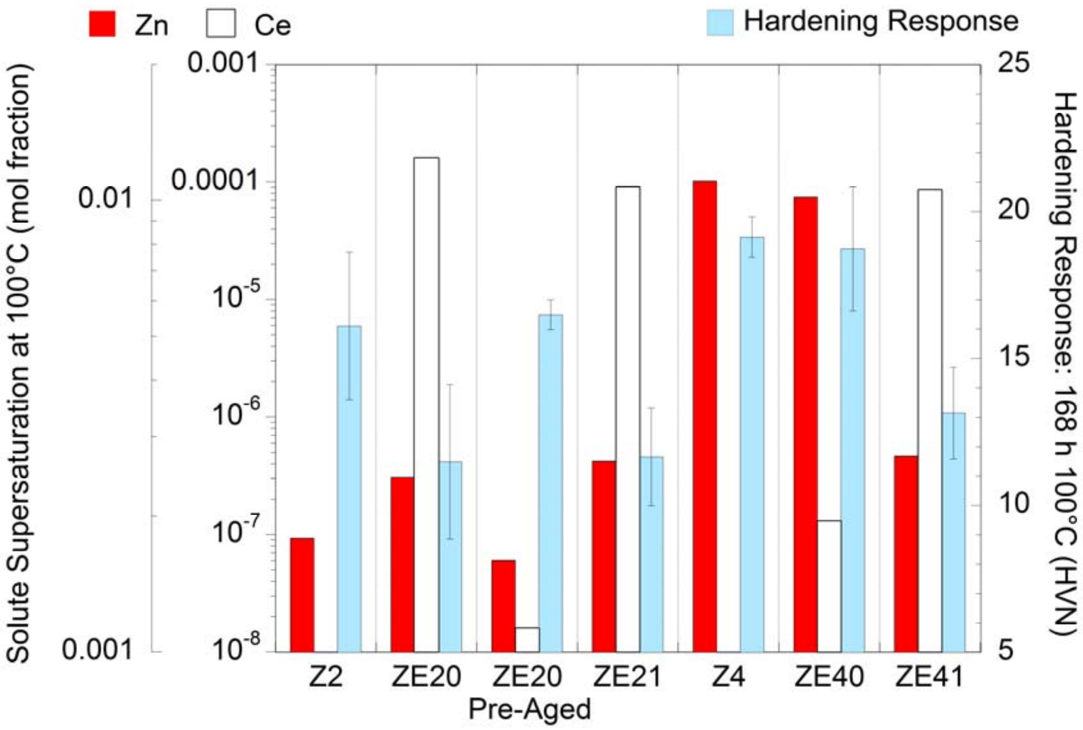

Figure 5-4: Calculated supersaturations in mol fraction for solute elements in HCP-Mg at 100°C, and ageing responses for 168 h ageing at 100°C for Mg-Zn-(Ce) alloys.

To further examine the trends in the alloying/microalloying contents and hardening responses for the alloys examined in this chapter, the supersaturation levels for Zn and Ce are calculated. These calculations are performed using values for the solutionizing and ageing temperature solute concentrations obtained by thermodynamic calculations with the FactSage software. It should be noted that only the portion of the material that exists in the HCP-Mg phase at the solutionizing temperature is used to calculate the equilibrium solubility levels at the ageing temperature. These results are plotted in Figure 5-4, along with the hardening response for each alloy after 168 h of ageing at 100°C. It is evident from Figure 5-4 that the matrix supersaturations of the solute elements do not necessarily scale with their bulk content in the alloys. This is most notable in that the Ce supersaturation in ZE20 is comparable to that of ZE21, and the Zn supersaturation is approximately equivalent in ZE21 and ZE41. The departure in supersaturation trends from those of bulk alloy content is due to the fact that the solutes are not only in the matrix, but are also present in the large secondary phase particles, examples of which were shown in Figure 5-3. The quantity of the large particles that can form during the processing of the alloy is dictated by their thermodynamic stability at the solutionizing temperature.

A comparison of the binary Z2 and Z4 alloys shows the positive effect of Zn supersaturation on hardening, in the absence of Ce. Figure 5-4 also shows that the hardening responses in the high-Zn (i.e. 4 wt%) alloys that contain Ce correlate with the supersaturation level of Zn in the matrix as well. This correlation can be understood in that increased Zn supersaturation can further promote nucleation of the hardening Mg-Zn type precipitates, and as a result this will produce a higher precipitate number density and an increased age hardening response. The calculation results presented in Figure 5-4 show how the higher Ce alloy content of the ZE41 alloy can serve to lower its Zn supersaturation, and thereby reduce its hardening response compared to Z4 and ZE40. This reduced Zn supersaturation is due to the formation of Zn-Ce containing coarse particles that are stable at the solutionizing temperature. These particles effectively tie up Zn and prevent it from being present in solution at the onset of ageing. This effectively deprives the solid solution from the benefit of the high level of Zn in the alloy composition.

While the effects of Zn supersaturation are made clear by examining the binary and high-Zn alloys, the effect of Ce supersaturation is less easily understood. A comparison of the hardening responses for Z4 and ZE40 suggests that a small amount of Ce supersaturation has a negligible effect on hardening. A significant decrease in hardening is noted for the ZE41 alloy which has an increased Ce supersaturation; however, as this decrease in hardening can also originate from the aforementioned reduction in Zn supersaturation, the individual contributions of the two effects cannot be separated in that alloy. Instead, the effect of Ce supersaturation can be more clearly observed by comparing trends in the low-Zn (i.e. 2 wt%) alloys. For the low-Zn alloys, the Ce-containing ZE20 and ZE21 alloys have similar respective supersaturations for Zn and Ce, and also exhibit similar hardening responses. A comparison of these alloys with the binary Z2 alloy, however, shows that while the Zn supersaturation levels of all the alloys are relatively similar, the hardening responses of the ternary alloys are lower. It is therefore concluded that the reduction in the hardening responses for these Ce-containing low-Zn alloys is due to the effects of Ce supersaturation. This observed reduction in the hardening response due to Ce solutes appears contrary to the behaviour of many other alloying/microalloying additions reported for Mg-Zn system in literature [39,41,45,133].

To confirm the negative effect of increased Ce supersaturation on the precipitation hardening response, a pre-ageing heat treatment was designed to diminish Ce supersaturation in the ZE20 alloy prior to aging at 100°C. The ZE20 alloy is selected for pre-ageing, as the supersaturation ratio of Ce:Zn in the as-quenched condition is highest for this alloy, and the age hardening response is the lowest. The pre-aging temperature was determined using FactSage calculations, which show that for the ZE20 alloy at 300°C, Zn still exhibits significant solubility in Mg but the solubility of Ce is near-zero. To implement the pre-ageing heat treatment, samples of the ZE20 alloy are aged for 3 h at 300°C following solutionizing, and prior to ageing at 100°C. It is found that for ZE20 in the as-pre-aged condition, the hardness is nearly identical to that of the as-solutionized ZE20. The evolution of the hardness of the pre-aged alloy during aging at 100°C is reported in Figure 5-1a, from which it can be seen that the pre-aging process successfully eliminates the negative effect of Ce solute in reducing the hardening response. The pre-aged ZE20 alloy hardens more significantly than the directly aged ZE20 alloy, at level similar to that of the binary Z2 alloy. Similar hardening behaviours for the pre-aged ZE20 and binary Z2 alloy are consistent with the calculated supersaturations presented in Figure 5-4, which show identical Zn and Ce supersaturations for the two alloys, considering that the pre-ageing heat treatment practically eliminates Ce from the solid solution.

In the as-pre-aged condition, precipitates that are not found in the ZE20 alloy when given the standard solutionizing and ageing heat treatment are observed by TEM. These precipitates are formed during the pre-ageing heat treatment, and are shown in Figure 5-5a, b. The morphology of these precipitates is generally hexagonal or circular plates, parallel to the basal planes, and they are found to exist with an average diameter of approximately 50 nm. EDS measurements from these precipitates confirm the presence of significant levels of Ce, as well as Zn (Figure 5-5c and d), signifying that the predicted precipitation of Ce during the pre-ageing treatment is valid. Minimal hardening is achieved due to their presence, as seen from the nearly identical hardness values for the as-pre-aged and as-solutionized ZE20 alloy samples, which is attributed to the large inter-particle spacing of these precipitates (apparent in in Figure 5-5b). For artificial ageing of the pre-aged ZE20 alloy at 100°C, hardening is achieved by the formation of fine, hardening precipitates, such as those shown in Figure 5-5e. These precipitates appear to have characteristics similar to those observed in the other aged Mg-Zn-(Ce) alloys.

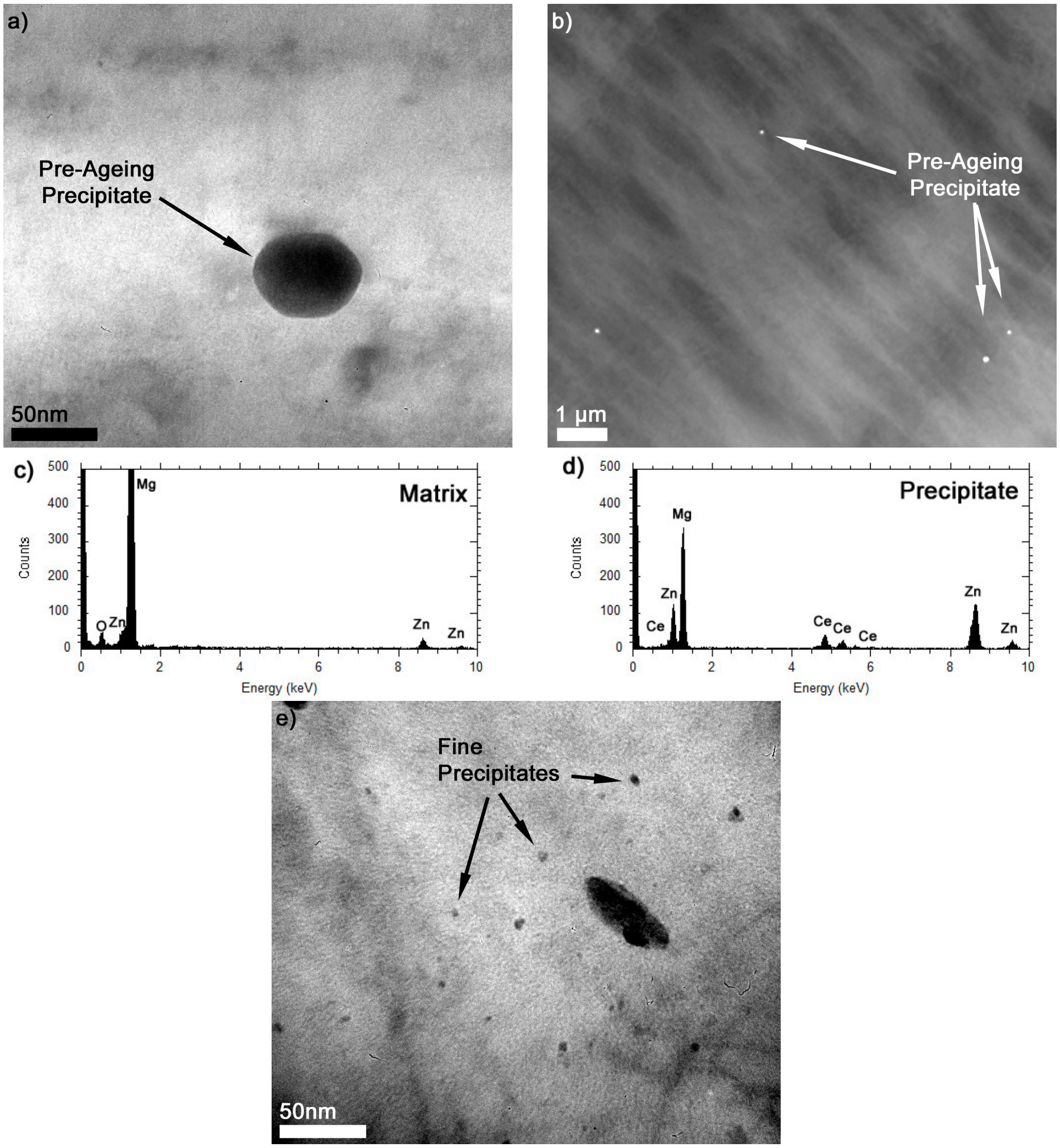

Figure 5-5: a) Bright field TEM image and b) low-magnification STEM image of ZE20 alloy pre-aged 3 h at 300°C, showing small precipitates on basal planes, with EDS spectra for the c) matrix and d) precipitates. e) fine precipitates in ZE20 alloy pre-aged, then artificially aged 168 h at 100°C. All micrographs from [0001] zone axis.

As evident by the TEM investigations and hardening considerations, the effect of Ce supersaturation on reducing the age hardening response can be attributed to a lower number density of precipitates, and an increase in the overall non-uniformity of the precipitate distribution. Both of these microstructural characteristics can be achieved by the modification of nucleation processes by Ce solutes. It should be noted that while the number density of precipitates may also be influenced by coarsening processes, considering the relatively low ageing temperature utilized in the current work, the role of coarsening is expected to be negligible. Therefore, only nucleation effects on the precipitate number density are considered.

The effect of Ce supersaturation on nucleation may be related to interactions of Ce and Zn solutes with lattice defects. Such defects are typically generated in excess during rapid quenching from high temperature heat treatments, such as water-quenching following solutionizing in the current case [20,134–137]. Point defects in the form of vacancies are often considered to assist with solute migration during the nucleation process [138–140]. The tendency of vacancies to interact with solutes to such an effect is related to the solute-vacancy binding energy within a given solution. Recent calculations, based on density functional theory, report the binding energies of Zn and Ce, both within the basal plane of Mg matrix, to be 0.05 eV and 0.08 eV, respectively [141,142]. The greater solute-vacancy binding energy for Ce than Zn, shown by these values, suggests that vacancies will more strongly bind to Ce solutes, compared to Zn. As a result of such preferential binding to Ce, Zn solutes may be deprived from binding to vacancies, which will negatively affect the nucleation of Mg-Zn type precipitates. It should be noted that this effect may be prominent whether vacancies are present either in equilibrium or excess levels. Cases in which solute-vacancy binding occurs preferentially with one solute component over another have notably been reported to reduce the natural ageing response in Al-Cu when microalloyed with Sn, In, Cd, or Au [143–146]. It is hypothesized here that the preferential binding of vacancies to Ce in the nucleation stage is responsible for the reduced number density of Mg-Zn type precipitates in the Ce-containing alloys.

The preferential binding of Ce to vacancies, and its effect on nucleation, may also influence the resulting precipitate distributions. Nucleation of precipitates on heterogeneous sites, such as dislocations, are noted to not only reduce the energy barrier for nucleation, but also assist with solute diffusion [140]. Therefore, nucleation processes involving such sites will be particularly favored for precipitation, in comparison with homogeneous nucleation, when the concentration of mobile vacancies is significantly reduced [134]. In the current case, the preferential solute-vacancy binding involving Ce can thus serve to increase the tendency for vacancy-starved Mg-Zn phases to nucleate heterogeneously, resulting in an increased fraction of those precipitates to form non-uniformly on lattice defects, such as dislocations.

Further investigations are still required to evaluate the above hypotheses and confirm the exact effect of Ce on limiting the age hardening responses of Mg-Zn alloys when in solid solution. However, from the results obtained in this work it can be recommended that Ce addition to Mg-Zn alloys to be limited to microalloying levels if a high age hardening response is desirable, as high Ce levels in the alloy can reduce the Zn supersaturation in solid solution, and adversely affect the precipitation behavior of Mg-Zn type hardening precipitates. It is also recommended that the hardening response may be further optimized by minimizing the supersaturation of Ce in the Mg matrix through a suitable pre-aging process.

5.5 Summary

The precipitation hardening behaviours of Mg-2Zn and Mg-4Zn (wt%) alloys with alloying/microalloying additions of Ce are evaluated. It is found that for artificial ageing at 100°C, all alloys harden until an apparent peak-aged condition, after approximately 168 h of aging. The increase in hardness is attributed to the formation of Mg-Zn type precipitates which are fine in scale, but generally non-uniform in distribution. The apparent number densities of these fine precipitates correlate to the relative age hardening responses for the alloys in the peak-aged condition. The age hardening response is found to increase with increasing Zn supersaturation. High Ce alloy content can affect this negatively by forming coarse secondary phases, enriched in Ce and Zn, which are stable during solutionizing. These phases reduce Zn supersaturation, and therefore decrease the age hardening response. Ce additions are also found to negatively affect hardening when the Ce supersaturation level is high. This effect is confirmed by implementing a pre-ageing heat treatment for the ZE20 alloy that effectively removes Ce from solution by forming Ce-rich precipitates. This pre-ageing heat treatment restores the age hardening response of ZE20 during ageing at 100°C to a level similar to binary Mg-Zn. The effect of Ce supersaturation on reducing hardening is hypothesized to stem from the preferential binding of Ce with vacancies, which adversely affects Zn solute mobility and the nucleation of Mg-Zn type precipitates. This is suggested to lead to a reduced hardening response by decreasing the number density of precipitate nuclei, and increasing the non-uniformity of the precipitate distributions by promoting heterogeneous nucleation on lattice defects, such as dislocations. From the findings of this work, it is recommended that Ce addition to age-hardenable Mg-Zn alloys be limited to microalloying levels, or that Ce-supersaturation is minimized through alloy design and/or a suitable pre-ageing process.

6 Precipitation Hardening of Mg-Zn Alloys with Ce-Ca Microalloying Additions

While previous chapters have examined precipitation in the Mg-Zn-Ca and Mg-Zn-Ce alloy systems, the following chapter studies precipitation in Mg-Zn alloys with combined microalloying additions of both Ce and Ca. The precipitation hardening responses of the Mg-Zn-Ce-Ca alloys are examined, and compared to binary Mg-Zn alloys, as well as alloys with single microalloying additions of Ce or Ca. In-depth analysis is conducted to determine the precipitate microstructures and phase evolution in this alloy system.

6.1 Introduction

Despite the high potential for utilization of magnesium alloys as a lightweight material their use is limited by their generally low strength and poor ductility [8,10]. Two promising options to improve these properties are by increasing strength through precipitation hardening [21,147], and enhancing ductility by rare earth element additions [69,70,72,111]. Recent research has demonstrated that the precipitation hardening effect in magnesium alloys can be significantly improved by the additions of microalloying elements [38,41,45,147]. These are additional elements added to a base alloy in small amounts (typically < 0.5 wt%). The addition of rare earth elements to magnesium alloys has been noted to improve formability through the promotion of a random texture [73,74]. Among the rare earth elements, Ce has been reported as one of the most potent elements for affecting texture [70]. While the effect of Ce on the precipitation hardening response of Mg-Zn alloys is not considered beneficial (see chapter 5), its addition in microalloying levels improves texture in these alloys [73,118]. It has also been shown that Mg-Zn-Ca alloys, with Ca in both alloying (see chapter 4) and microalloying levels [40,41,43] can offer a significant precipitation hardening effect. Therefore, there exists the opportunity to obtain both improvement in texture and precipitation hardening capability by alloying and/or microalloying of Mg-Zn alloys with Ce and Ca. This chapter reports on the precipitation hardening effect of such alloys in comparison with corresponding binary Mg-Zn alloys, as well as Mg-Zn alloys with either Ce or Ca single microalloying element additions. It should be noted that utilization of Ca as an additional microalloying element is also due to the multiple benefits in processing and properties that Ca has demonstrated when added in alloying or microalloying levels to magnesium alloys, and particularly to Mg-Zn alloys [11,40,41,52–54,56,95,133,148,149].

6.2 Experimental Methodology

A list of the experimental alloys examined in this chapter, as well as the tests conducted, is presented in Table 6-1. Alloys were prepared according to the description in 3.1, and rolled, annealed, and solutionized as per the procedures described in section 3.2. To examine the precipitation hardening effect, samples of the alloys quenched from the solutionizing temperature were age-hardened in air atmosphere at 180°C. The hardening responses of the alloys were measured and the microstructures and precipitation behaviours were investigated by combined TEM and DSC analysis, with all testing conducted according to the methods outlined in the respective sections of chapter 3. In analyzing the APT results, cluster calculations were performed using the maximum separation method, with Ca and Zn selected as target solutes. For Ca as a target solute, the minimum cluster size was set as 5 solute atoms, the maximum 6-nearest-neighbour separation distance of 1.7 nm and an envelope distance of 0.9 nm to include all other surrounding atoms. For Zn clustering, the minimum solute atoms was set to 10, with the maximum separation distance set to 0.65 nm and the envelope distance 0.5 nm. In the Zn clustering calculation, the higher value for the minimum solute atoms and lower values for the separation and envelope distances were set due to the higher matrix concentration for Zn, in order to better distinguish Zn clusters from the randomly distributed Zn solute in the matrix.

Table 6-1: List of experimental alloys investigated and test conducted related to chapter 6.

Alloy Designation	Hardness Measurement	TEM	HR-TEM	HAADF-STEM	DSC	APT
Z2	x	-	-	-	x	-
ZE20	x	-	-	-	x	-
ZEX200	x	x	x	x	x	-
Z4	x	x	x	x	x	-
ZE40	x	x	x	x	x	-
ZX40	x	x	x	x	x	-
ZEX400	x	x	x	x	x	x

6.3 Results and Discussion

6.3.1 Precipitation Hardening Behaviour

The results of the hardness measurements on the aged alloys are shown in Figure 6-1a. In the as-quenched condition, the various alloys are observed to have different hardness values. These differences are attributed to grain size and solid-solution strengthening effects. A more straightforward comparison of the precipitation hardening capabilities of the alloys can be obtained by analyzing the increase in hardness from the as-quenched condition. These age-hardening responses of the alloys are plotted in Figure 6-1b.

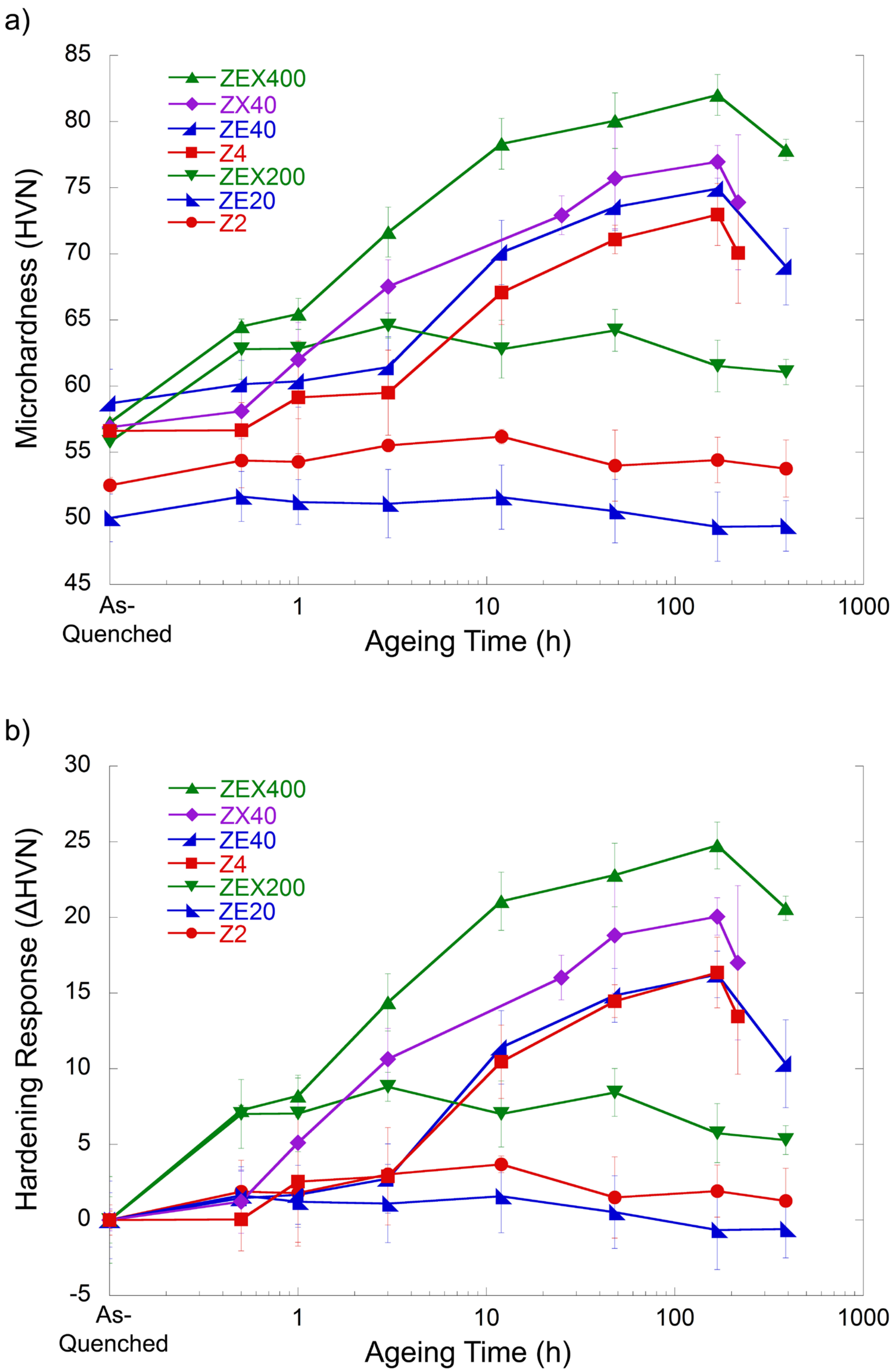

Figure 6-1: a) Hardness evolution and b) hardening response for Mg-Zn-(Ce)-(Ca) alloys aged at 180°C.

The double additions of Ce-Ca are observed to provide the highest improvement in hardening, when compared to either the binary or single-element microalloyed alloy variants of equivalent Zn content. The ZEX200 alloy achieves only a moderate age-hardening response, but this is considerable given that the Z2 and ZE20 alloys do not harden at all during ageing. The hardness of the ZEX200 alloy exhibits a relatively rapid increase in hardness during the early stages of ageing ($t < 3$ h), but is found to reach a plateau after that time. Ageing beyond 48 h for the ZEX200 alloy produces a slight decrease in hardness, signifying the onset of over-ageing. The ZEX400 alloy is observed to harden rapidly from the initial stages of ageing, and continue to harden at a significant rate until the peak-aged state, which is reached after 168 h of ageing. The ZEX400 alloy achieves a peak hardness of 82 HVN (hardening response of 25 HVN), which is the highest among the alloys examined in this work, excluding the high-Ca alloys presented in chapter 4.

The hardening response results for the alloys indicate that the single additions of Ce do not improve precipitation hardening compared to the binary alloys. This lack of beneficial effect on hardening is evident by comparing the hardening response curves for the Z4 and ZE40 alloys, as well as the Z2 and ZE20 alloys, and is in good agreement with the results from chapter 5 for 100°C ageing. On the other hand, the addition of Ca appears to be very effective at enhancing hardening, as is clearly demonstrated by the respective hardening responses of the Z4 and ZX40 alloys. The double addition of Ce-Ca however produces the greatest improvement in the age-hardening response. This can be seen in the age hardening response of the ZEX400 alloy, which in the peak-aged condition exhibits an increase of approximately 5 HVN compared to the ZX40 alloy, and an increase of approximately 10 HVN compared to the Z4 or ZE40 alloys. The small benefit to hardening response by the combined additions of Ce and Ca over the single Ca addition may suggest possible synergistic effects between the two microalloying elements. As the ZEX400 alloy achieves the greatest precipitation hardening response of the alloys examined in this work, the investigation of precipitation hardening in this alloy will be the focus of the remaining parts of this chapter. However, analysis of the other alloys will occasionally be presented for comparison, in order to aid in understanding the effects of the alloy chemistry on the observed precipitation behaviour.

6.3.2 Peak-Aged Microstructure of the ZEX400 Alloy

TEM analysis of the peak-aged ZEX400 alloy (168 h ageing at 180°C) reveals a high density of precipitates in the microstructure. Three major precipitate types are noted: 1) large rods parallel to the c-axis of the Mg matrix, (seen end-on in Figure 6-2a, and from the side in Figure 6-2b and c), 2) large basal plates (seen in Figure 6-2a and c), and 3) numerous fine basal plates (seen in Figure 6-2b and c). The c-axis rod precipitates are found with lengths of 100 nm to several hundred nanometers or more, and an approximate average diameter of 10-20 nm. The large basal plates are approximately 75-100 nm in average diameter along the basal plane, with thicknesses of around 15-30 nm. The fine basal plates are observed with apparent thicknesses of < 5 nm and diameters ranging from 10-30 nm. SADPs are presented from the c-axis rods in Figure 6-2d, and from the large basal plates in Figure 6-2e. Based on these diffraction patterns, as well as the observed precipitate morphologies and orientations, the c-axis rod precipitates and large basal plates are identified as the β'_1 and β'_2 precipitates, respectively, as commonly-reported for Mg-Zn [42]. The fine basal precipitates are however unreported for binary Mg-Zn alloys. The fine basal plates are found in a much higher number density than the other precipitate types. The β'_1 rods are also observed in high numbers, while the β'_2 plates are more occasionally found throughout the matrix. The relative number densities and distributions of the above three types of precipitates can be seen from the images presented in Figure 6-3. It should be noted that additional precipitates were also observed along the grain boundaries in the peak-aged microstructure; however, this chapter will only consider precipitation within the grains, with precipitation at and near grain boundaries analyzed in greater detail in chapter 7.

From Figure 6-3, the distributions of all three precipitate types generally appear uniform. However, the β'_1 and β'_2 precipitates are occasionally observed aligned in micron-scale arrays along the [0001] and $\langle 11\bar{2}0 \rangle$ matrix directions, as seen in Figure 6-3a. Alignment of Mg-Zn precipitates along $\langle 11\bar{2}0 \rangle$ matrix directions has been previously reported by Buha [18], who attributed the observation to preferential precipitate nucleation in the strain fields of existing precipitates. Clark [20] also reported alignment of the β'_1 precipitates, which he attributed to nucleation along dislocations formed during quenching. To the best of the author's knowledge, no reports have previously presented precipitate alignment along the [0001] matrix direction. Assuming the hypothesis of Clark [20] that the alignment occurs along dislocation lines, it is possible that the [0001] direction alignment is produced by nucleation along a prismatic $\langle a \rangle$ dislocation. However, further investigation into this behaviour is required to confirm such an effect.

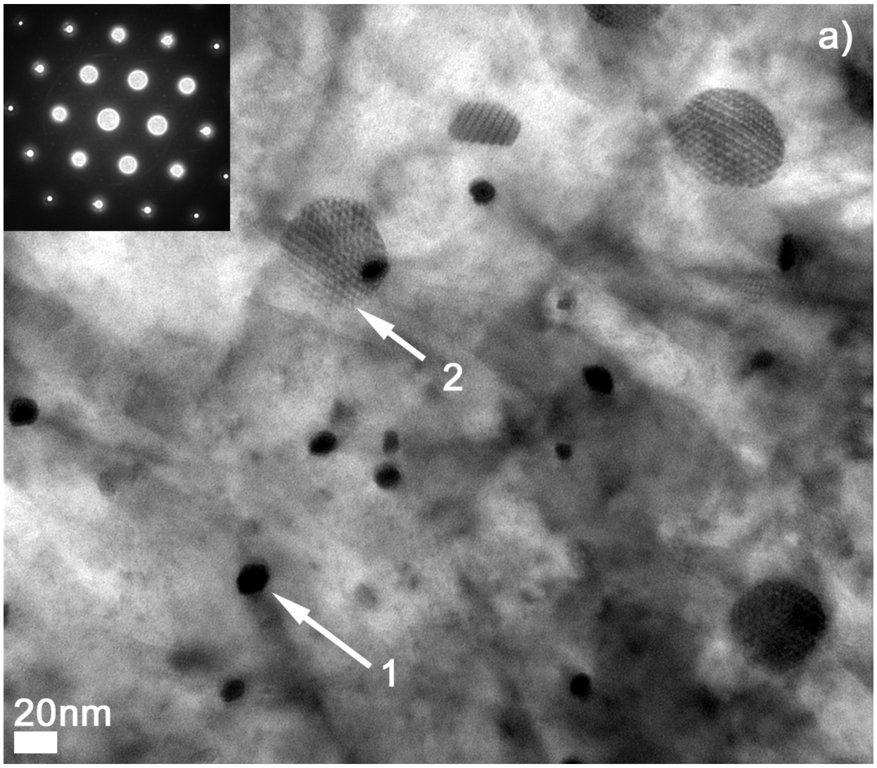
a)
2
1
20nm


b)
1
3
20nm

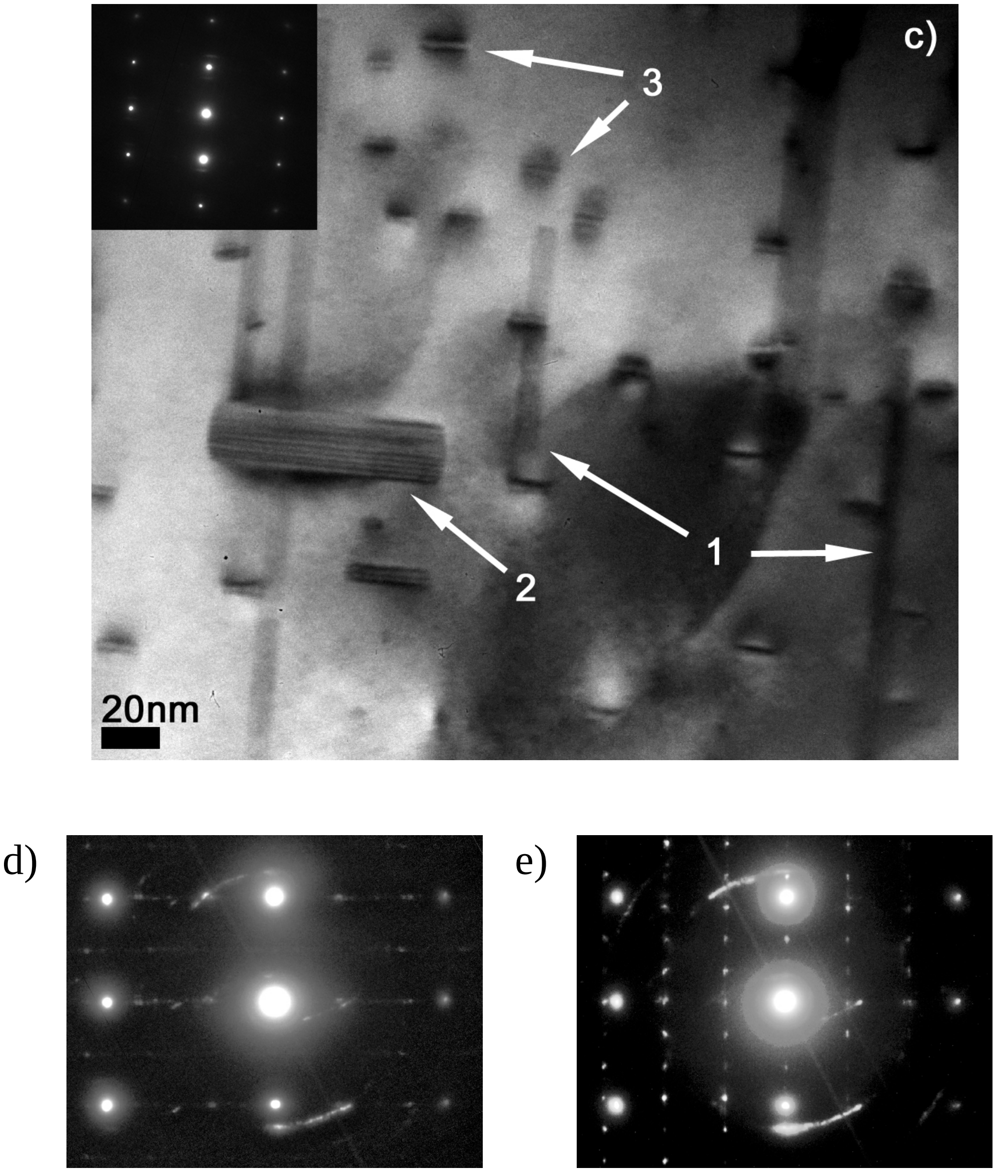

Figure 6-2: a,b,c) TEM micrographs of peak-aged ZEX400 (aged 168h at 180°C), a) [0001] b) $\langle 11\bar{2}0\rangle$, c) $\langle 1010\rangle$ zone axes, with precipitates marked as indicated in the text. d,e) $\langle 10\bar{1}0\rangle$ matrix zone axis SADP for d) c-axis rods (precipitate 1), and e) large basal plates (precipitate 2). Observations for a, b, performed by P. Donnadieu.

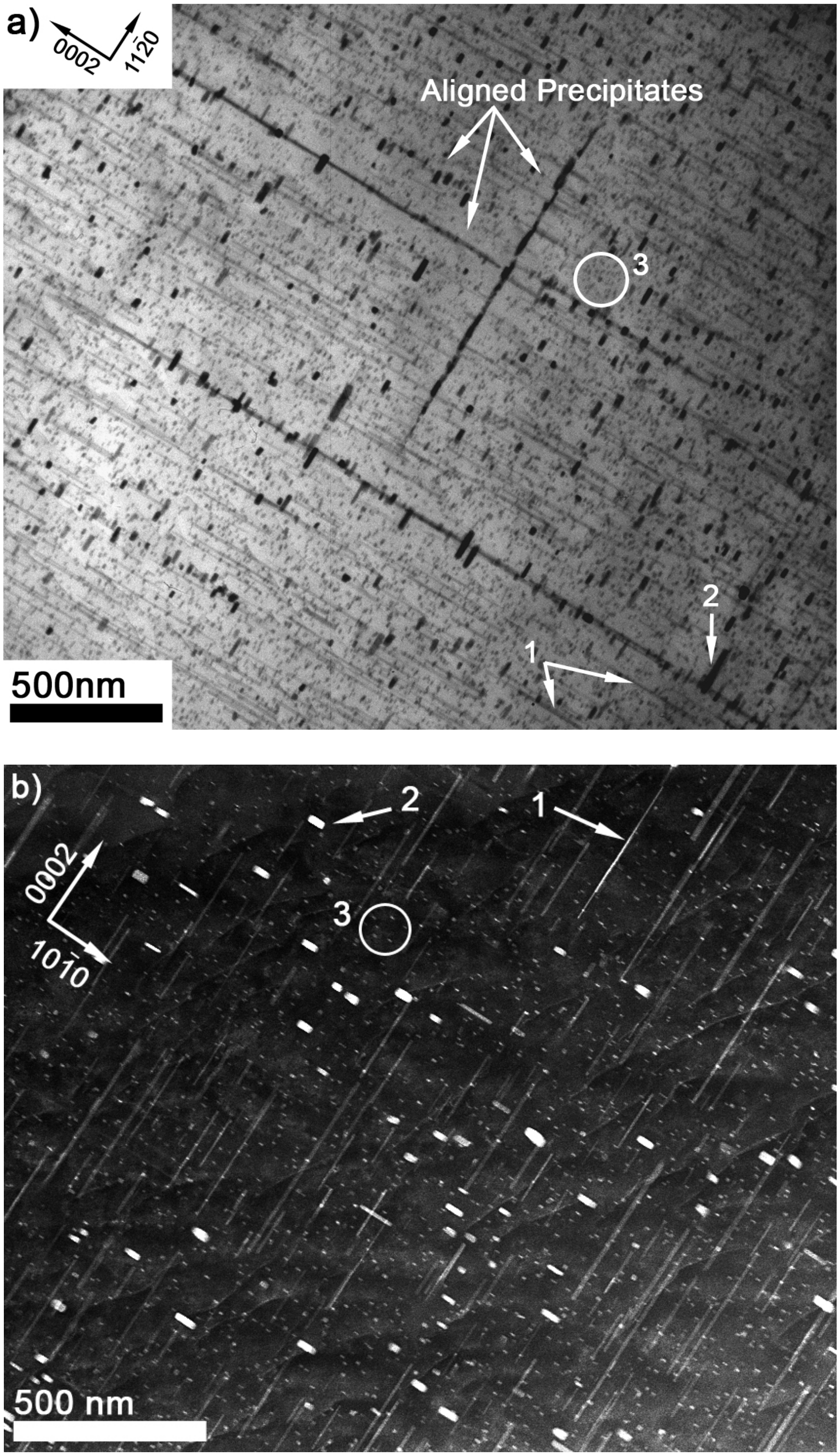

Figure 6-3: a) Bright-field TEM image, $\langle 10\bar{1}0\rangle$ zone axis, and b) HAADF-STEM image, $\langle 11\bar{2}0\rangle$ zone axis showing overview of precipitate microstructure in peak-aged ZEX400 alloy (aged 168h at 180°C), with precipitates marked as indicated in the text.

In relating the observed precipitate types and distributions to the hardening behaviour, it is noted that the lowest inter-particle spacings are found for the β'_1 precipitate rods, and the fine basal plate precipitates. Such small inter-particle spacings will positively affect the hardening capabilities of these two precipitate types. Furthermore, the fine basal precipitates are also observed to have a coherent strain contrast with the surrounding matrix (see Figure 6-2b) which can provide strengthening even when a dislocation does not directly encounter the precipitate [75,76]. The c-axis rod morphology of the β'_1 is also noted as very efficient at strengthening against both basal and prismatic $\langle a \rangle$ slip [81,82]. In comparison, the basal plate morphology of the fine plates has been reported as relatively less effective [81]. However, in a sufficiently high number with low inter-particle spacing, as observed in the current work, basal plate precipitates can still be effective at hardening [53,75,76,81,150]. In particular, basal plates are relatively effective at inhibiting prismatic $\langle a \rangle$ slip, which is important as this type of slip is reported to determine macroscopic yielding of magnesium [84]. In contrast to the β'_1 precipitate rods and fine basal plate precipitates, the β'_2 precipitates are observed to have a fairly large average inter-particle spacing. Such a large average inter-particle spacing of the β'_2 precipitates, and their relatively low numbers, will translate to producing a minimal hardening effect. Therefore, it is likely that a combination of the β'_1 precipitates and the fine basal precipitates is responsible for achieving maximum hardening in the peak-aged ZEX400 alloy.

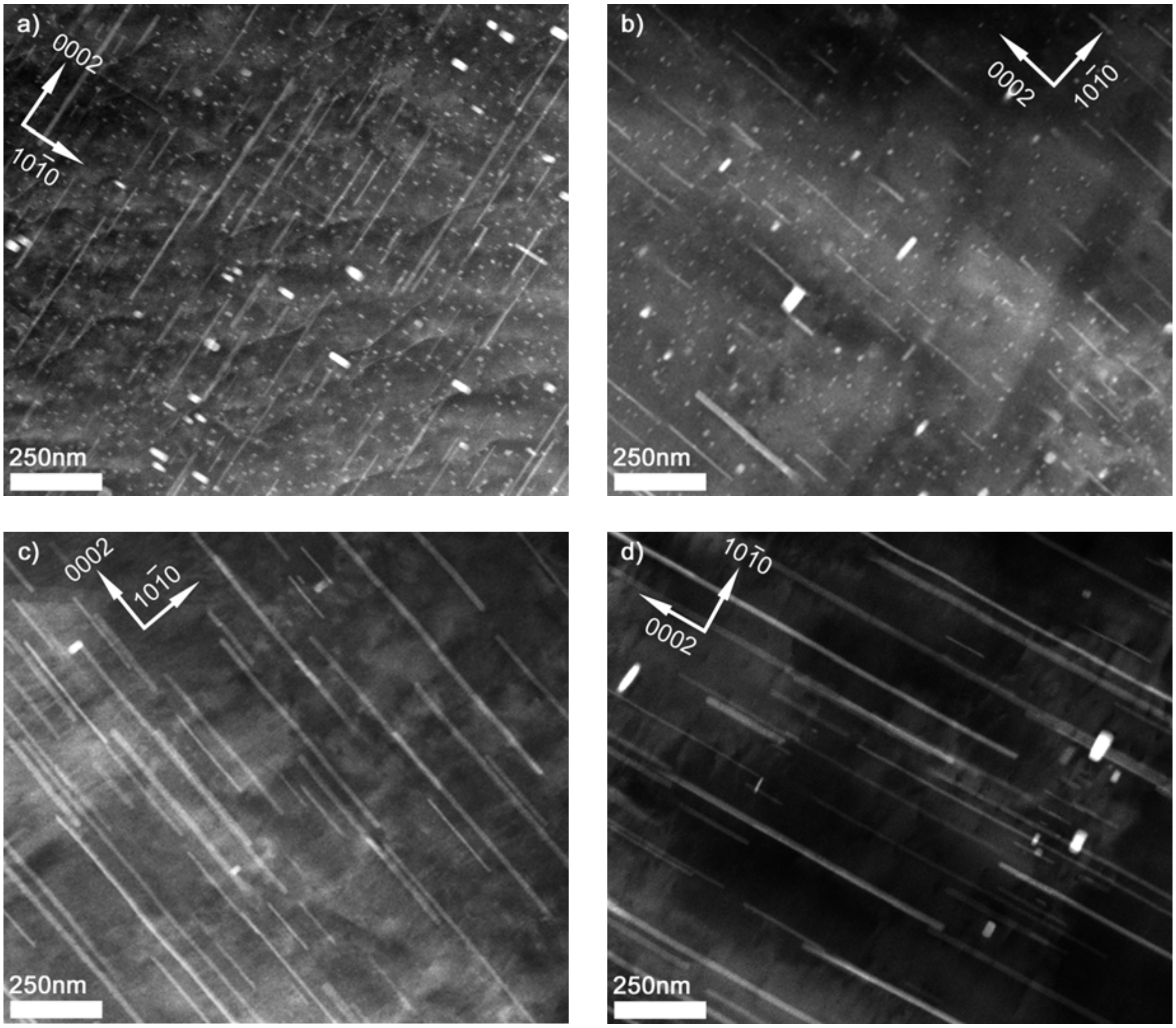

Figure 6-4: HAADF-STEM images of a) ZEX400, b) ZX40, c) ZE40, d) Z4 alloys aged 168 h at 180°C from $\langle 11\bar{2}0 \rangle$ zone axis.

Comparisons of the peak-aged microstructures of the ZEX, ZX40, ZE40, and Z4 alloys can be drawn from the HAADF-STEM images presented in Figure 6-4, which highlight the different effects of the Ce, Ca, and Ce-Ca microalloying elements on the precipitate types and distributions. The most apparent differences between the alloys are: a) the size and distribution of the β'_1 rod precipitates, and b) the presence (or lack) of the fine basal plate precipitates. Between the Z4 and ZE40 alloys, the β'_1 rod precipitates appear very similar in size and distribution. However, for the Ca-containing ZEX400 and ZX40 alloys, the β'_1 rods are generally shorter, although the apparent width is not very different. The distribution of the β'_1 phase also appears refined in the Ca-containing alloys, especially for the ZEX400 alloy in comparison with the Z4 alloy. The difference regarding the fine basal precipitates is also between the alloys which contain Ca and those which do not. The fine basal plate precipitates observed in the peak-aged condition for the ZEX400 alloy are also apparent in the ZX40 alloy. However, no similar fine precipitate plates are observed in the Z4 alloy, or the ZE40 alloy. In relating the microstructures to the precipitation hardening responses (Figure 6-1b), it is seen that the Ca-containing alloys also exhibit the greatest hardening responses. Therefore, these results suggest that the increased hardening due to Ca modification can be attributed to a refinement of the β'_1 rod precipitates and the presence of the fine basal plate precipitates. The nature of those two precipitates in the ZEX400 alloy, and the origin of their respective refinement/formation are explored further in the following subsection.

6.3.3 Precipitates in the ZEX400 Alloy

Detailed chemical analysis of the β'_1 precipitates is achieved by APT analysis of a ZEX400 alloy sample volume containing sections of those precipitates. The reconstructed atom maps and concentration profile for a β'_1 precipitate, for an alloy aged 96 h at 180°C, are shown in Figure 6-5. Composition data for the precipitates is given in Table 6-2. From the Zn content in Figure 6-5c and Table 6-2, it appears that the stoichiometry of the β'_1 precipitates is closest to MgZn. This finding is similar to that of the recent report by Bhattacharjee et al. [40] for an Mg-6.2Zn-0.2Ca (wt%) alloy analyzed by 3DAP after 4 h of ageing at 160°C. In that work, Bhattacharjee et al. [40] also reported that the β'_1 precipitates contained approximately 1 at% Ca. Such a result is not found in the current study, with levels of both Ca and Ce detected in the precipitates at much lower levels than 1 at%. The Ca content is found to be close to the matrix level, signifying a lack of segregation to the β'_1 precipitates. The Ce content appears to be slightly higher, with this apparent Ce enrichment also seen in the atom map shown in Figure 6-5b. However, due to the very low overall Ce solute content, such enrichment cannot be proven as statistically significant [124]. It is more likely that the apparent enrichment is an artefact of the ranged ion assignment during reconstruction, as the mass-to-charge ratio of the most abundant Ce peak ($^{140}Ce^{2+}$, 69.95 u/e) is close to that of an abundant Zn peak ($^{68}Zn^{+}$, 67.92 u/e) and overlaps another less-abundant Zn peak ($^{70}Zn^{+}$, 69.93 u/e). Given the very high level of Zn in the precipitates, an erroneous reading of slight Ce enrichment could be produced in this manner. Therefore, given the levels of Ca and Ce enrichment found in this work and considering both statistical and experimental errors, the β'_1 precipitates are not likely to contain any significant level of microalloying elements.

Table 6-2: Composition data for the APT results shown in Figure 6-5.

	Zn (at%)	Ca (at%)	Ce (at%)
Matrix	0.59 ±0.039	0.019 ±0.007	0.010 ±0.005
Precipitate (average)	50.71 ±0.254	0.038 ±0.039	0.359 ±0.030

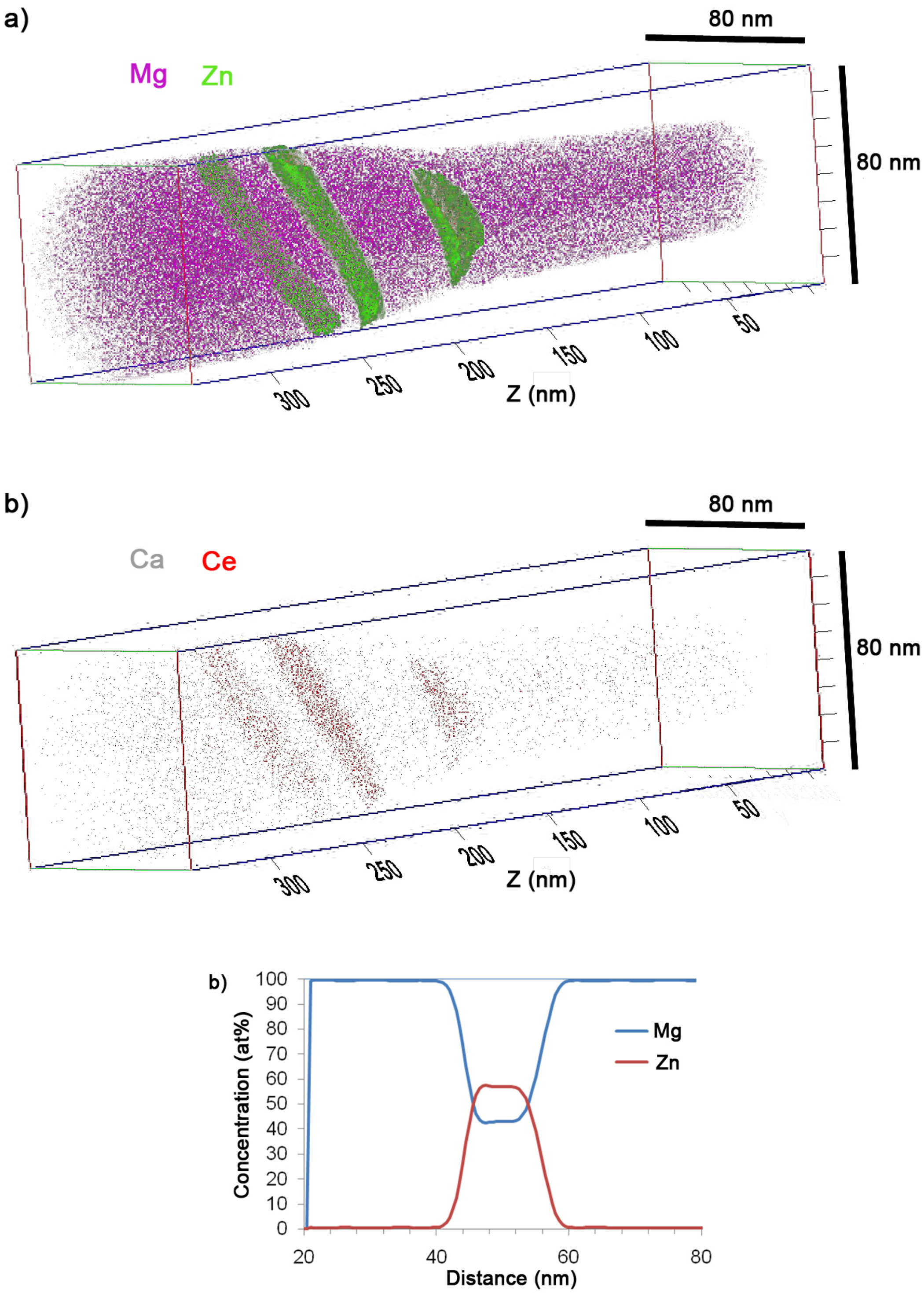

Figure 6-5: APT reconstructed atom map for ZEX400 aged 96 h at 180°C showing c-axis rod precipitates passing through the analysis volume, with a) Mg and Zn solute showing (Zn iso-concentration surfaces on precipitates), b) Ce and Ca solute, c) 1-D concentration profile through a precipitate. APT reconstruction performed by G. Sha.

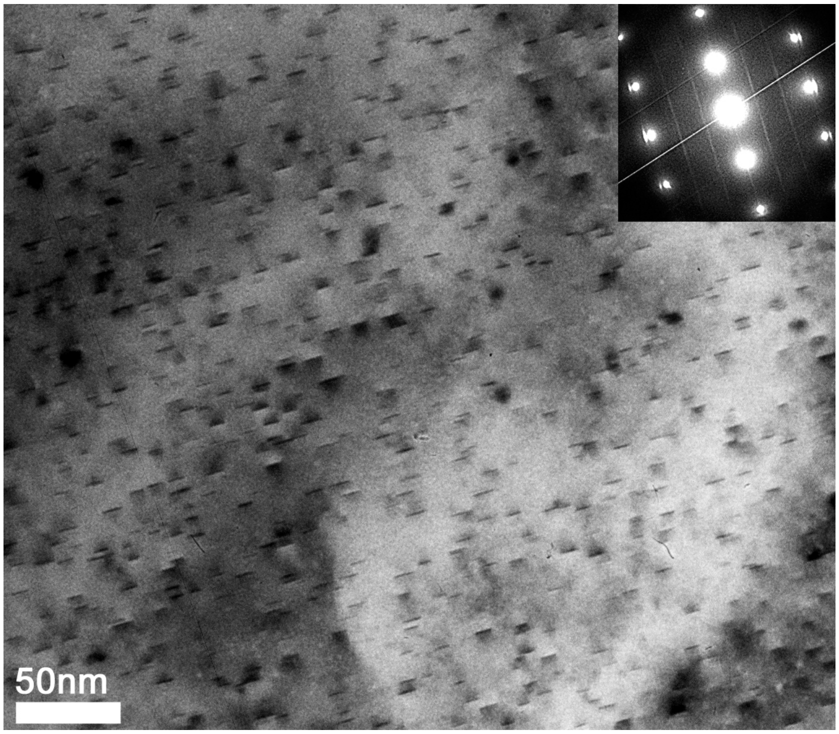

Figure 6-6: Bright-field TEM micrograph of ZEX400 alloy aged 3h at 180°C, $\langle 10\bar{1}0\rangle$ zone axis, with streaking in SADP insert.

Insight into the nature of the fine basal precipitates in the ZEX400 alloy can be obtained by analysis of these phases when they first appear in the microstructure. This analysis is conducted by TEM observation of the microstructure after 3h of ageing at 180°C, which represents an intermediate point along the age-hardening curve (i.e. an under-aged condition). After 3h of ageing, no β'_1 or β'_2 phases are found in the ZEX400 alloy; however, a uniform distribution of fine basal plate precipitates is already observed, as shown in Figure 6-6. The average size of these plate precipitates is smaller than in the peak-aged condition, with diameters ranging from 5-10 nm. Streaking is also observed parallel to the [0001] direction at $1/3\{11\bar{2}0\}$ and $2/3\{11\bar{2}0\}$ in the $\langle 10\bar{1}0\rangle$ zone axis SADP in Figure 6-6, which was notably absent from observations of the peak-aged condition. This streaking suggests the presence of a high number of ordered GP zones in the microstructure [53,97].

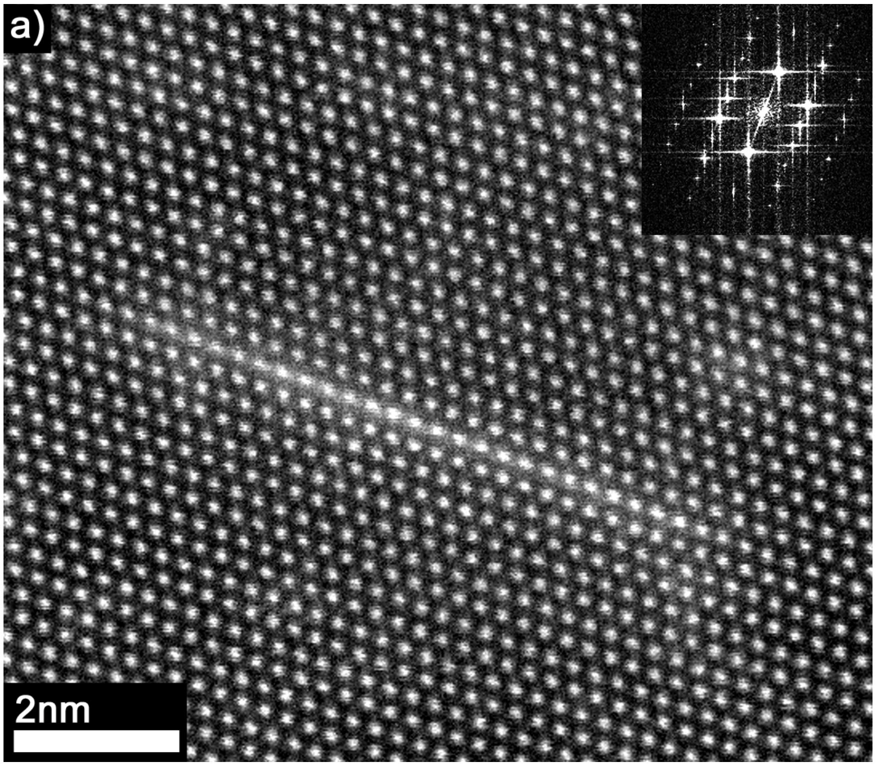
a)
2nm

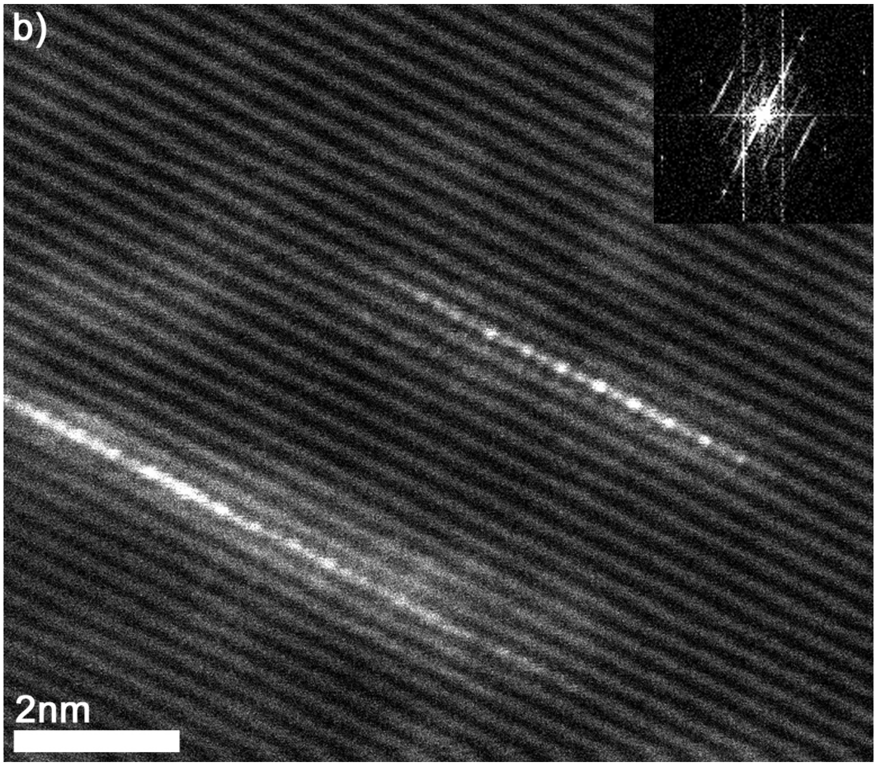
b)
2nm

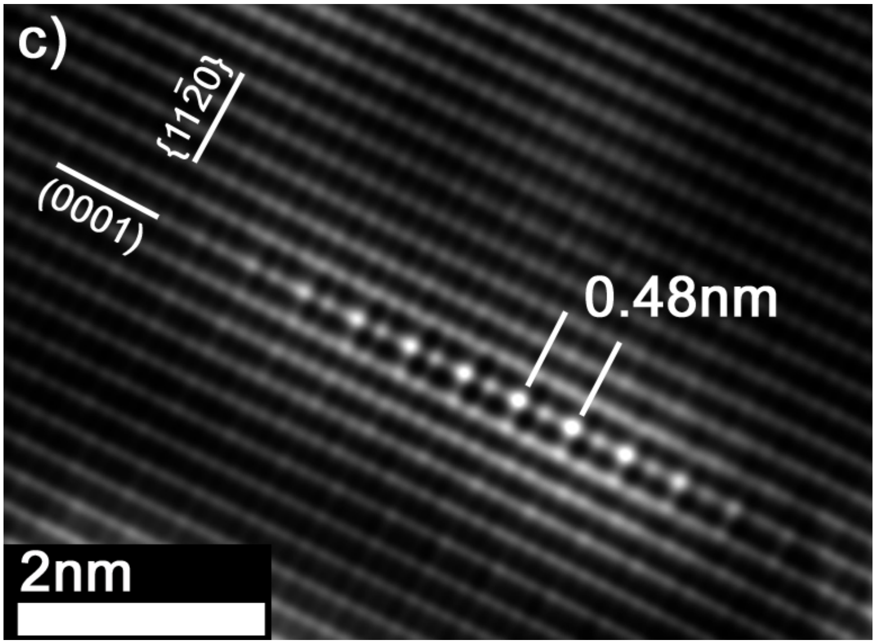

Figure 6-7: HAADF-STEM images of ZEX400 aged 3 h at 180°C showing monolayer GP zones with corresponding FFT inserts from a) $\langle 11\bar{2}0\rangle$ b) $\langle 10\bar{1}0\rangle$ zone axis, and c) Fourier-filtered image of monolayer GP zone shown in b).

High-resolution HAADF-STEM images presented in Figure 6-7 confirm the presence of monolayer GP zones aligned within a single basal plane of the HCP-Mg matrix, which appear as bright lines due to the relatively heavy solute elements, with an average diameter of approximately 5-10 nm. Observations from the $\langle 11\bar{2}0\rangle$ zone axis (Figure 6-7a) show uniform brightness for every atomic column, while observations from the $\langle 10\bar{1}0\rangle$ zone axis (Figure 6-7b,c) show higher-contrast atomic columns, with a spacing of $3/2a_{\mathrm{Mg}}$ = 0.48 nm. The brightness of these columns indicates that they are rich in the relatively heavy solute atoms. These observations indicate that the solutes within the monolayer GP zones are likely arranged in a hexagonal structure, with $a_{\mathrm{GPZ}} = \sqrt{3}a_{\mathrm{Mg}} = 0.556$ nm, and an orientation relationship of $(0001)_{\mathrm{GPZ}}||(0001)_{\mathrm{Mg}}$, $\langle 11\bar{2}0\rangle_{\mathrm{GPZ}}||\langle 10\bar{1}0\rangle_{\mathrm{Mg}}$. A monolayer GP zone structure has previously been reported by Ping et al. [97] for Mg-Zn-RE and Oh-ishi et al. [53] for Mg-Zn-Ca based alloys, as shown schematically in Figure 2-8. The ordering of the monolayer GP zones is attributed in those works to a combination of undersized and oversized atoms, which together have a negative enthalpy of mixing. As proposed by Ping et al. [97], such a combination of undersized and oversized atoms can promote GP zone formation and ordering by reducing the misfit lattice strain. This combination of oversized and undersized atoms is also considered to affect the monolayer GP zone structure in the current alloy, as Zn is an undersized element compared to Mg (atomic radii of 1.379 Å and 1.598 Å respectively [151]), while Ca is oversized, with an atomic radius of 1.970 Å [151]. It should be noted that no GP zones (i.e. fine basal plate precipitates) observed to form in the ZE40 alloy, which indicates that Ca is the key to their formation. However, it is possible that Ce is incorporated into the GP zones in the ZEX400 alloy as well, as it is also oversized (atomic radius 1.818 Å [151]).

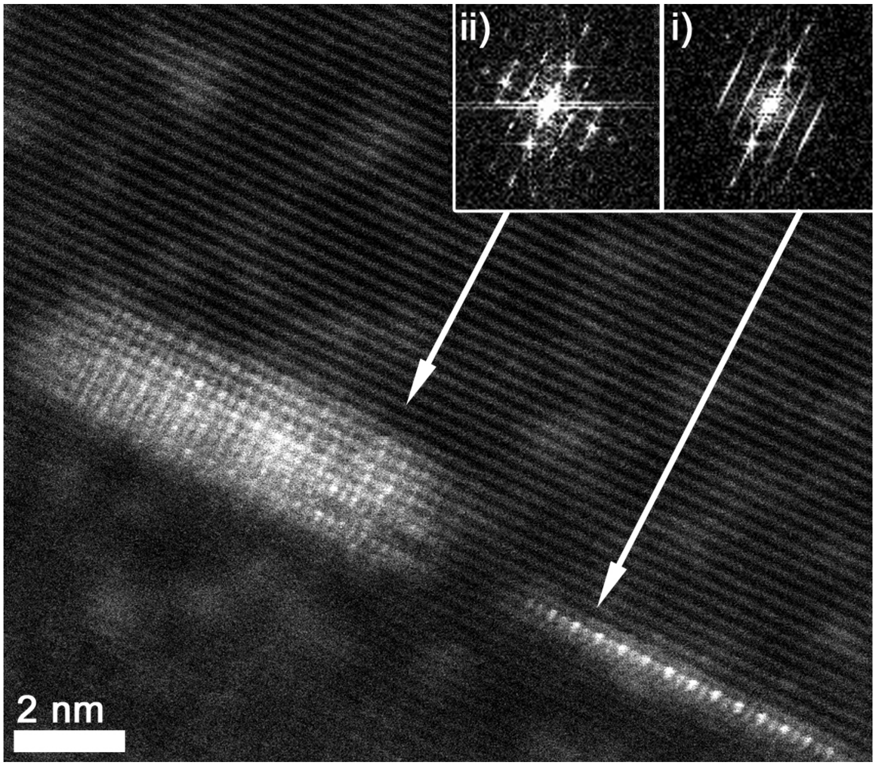

Figure 6-8: HAADF-STEM image showing a multi-layer and monolayer GP zone with corresponding FFT inserts, in ZEX400 aged 3 h at 180°C, $\langle 10\bar{1}0 \rangle$ zone axis.

HAADF-STEM (Figure 6-8) and HR-TEM (Figure 6-9) observations also reveal that in addition to the monolayer GP zones (marked i) some of the fine basal plates appear as multi-layer precipitates of 1-3 nm thickness (marked ii). The average diameter of these precipitates is approximately 5-10 nm, which is identical to the monolayer GP zones. Observations of the multi-layer precipitates by HAADF-STEM (Figure 6-8a, b) show that the atomic structure of each basal plane closely resembles that of the monolayer GP zone. This is seen in Figure 6-8a, where the monolayer GP zone and multi-layered precipitate both exhibit a periodic change in brightness, corresponding with a higher amount of heavier elements in the atomic columns, at the same interval distance. This suggests that the structure of the multi-layer precipitates on each (0001) plane may be equivalent to that of the monolayer GP zone. The thickness of the multi-layer precipitates can possibly arise due to the stacking of these monolayers in the standard HCP $\cdots\mathrm{ABAB}\cdots$ stacking sequence, which remains fully coherent with the matrix lattice. Fast Fourier transforms (FFTs) taken from the HR-S/TEM images of the precipitates (presented in Figure 6-8 and Figure 6-9) show that the monolayer GP zones exhibit similar streaking along $1/3\{11\bar{2}0\}$ and $2/3\{11\bar{2}0\}$ in the $\langle 10\bar{1}0\rangle$ zone axis FFTs as is observed in the corresponding SADP for the alloy aged 3 h at 180°C (Figure 6-6). However, for the thicker precipitates this streaking becomes non-continuous. Notably, for the $\langle 10\bar{1}0\rangle$ zone axis images, spots appear in the FFT for the multi-layered precipitates along the $1/3\{11\bar{2}0\}$ and $2/3\{11\bar{2}0\}$ streaks, at points equidistant to (0002) and $1/2(0002)$. This pattern is consistent with the lattice parameters and orientation relationship of the monolayer GP zone, with the additional lattice parameter of $c_{\mathrm{GPZ}} = c_{\mathrm{Mg}} = 0.521$ nm. These multi-layer precipitates are therefore suggested to be multi-layer GP zones, with a similar structure to that of the monolayer GP zones, but built up over several basal planes.

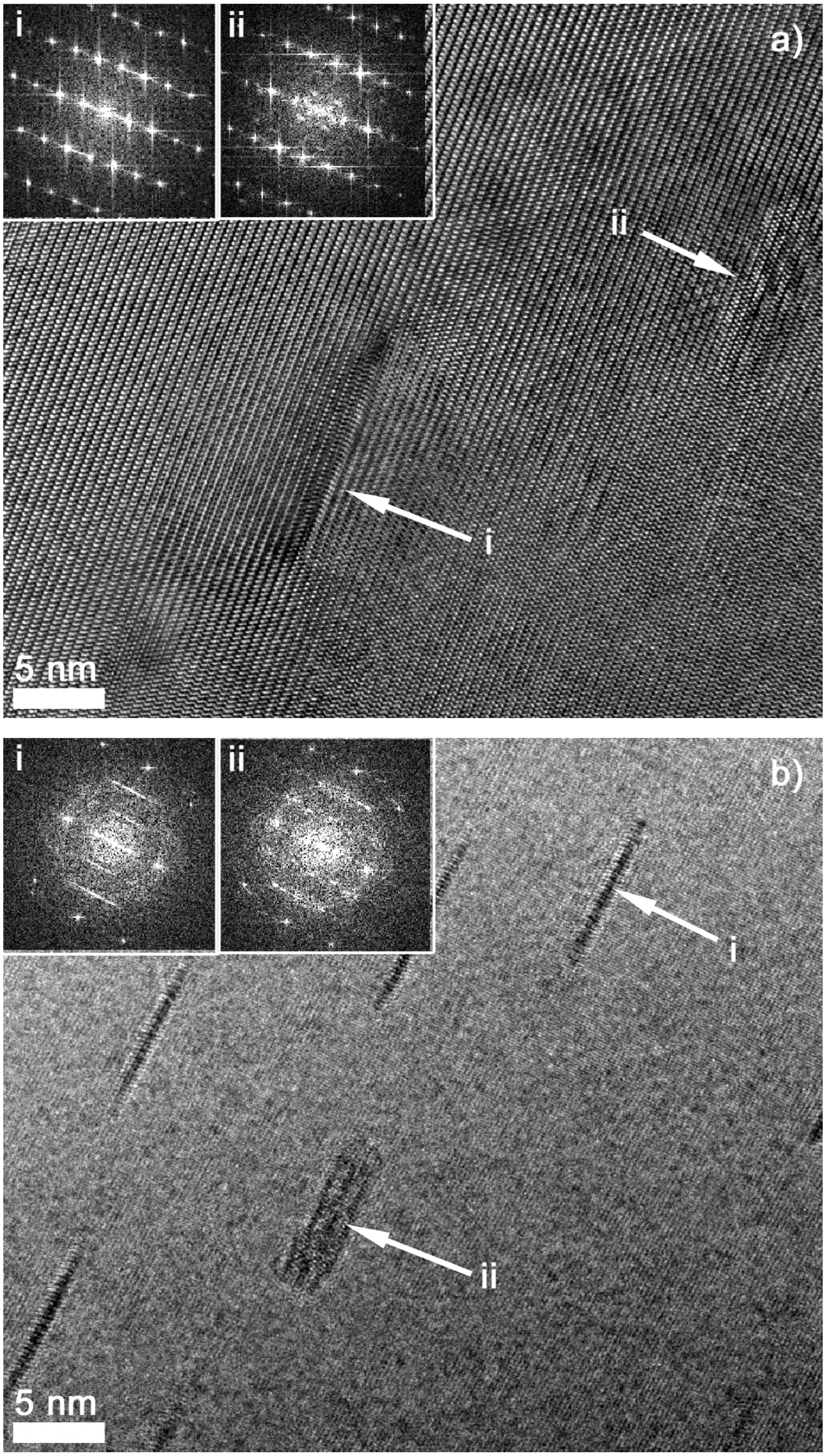

Figure 6-9: HR-TEM images of ZEX400 aged 3 h at 180°C showing i) monolayer GP zones and ii) multi-layer precipitates, with corresponding FFT inserts from a) $\langle 11\bar{2}0 \rangle$ b) $\langle 10\bar{1}0 \rangle$ zone axis.

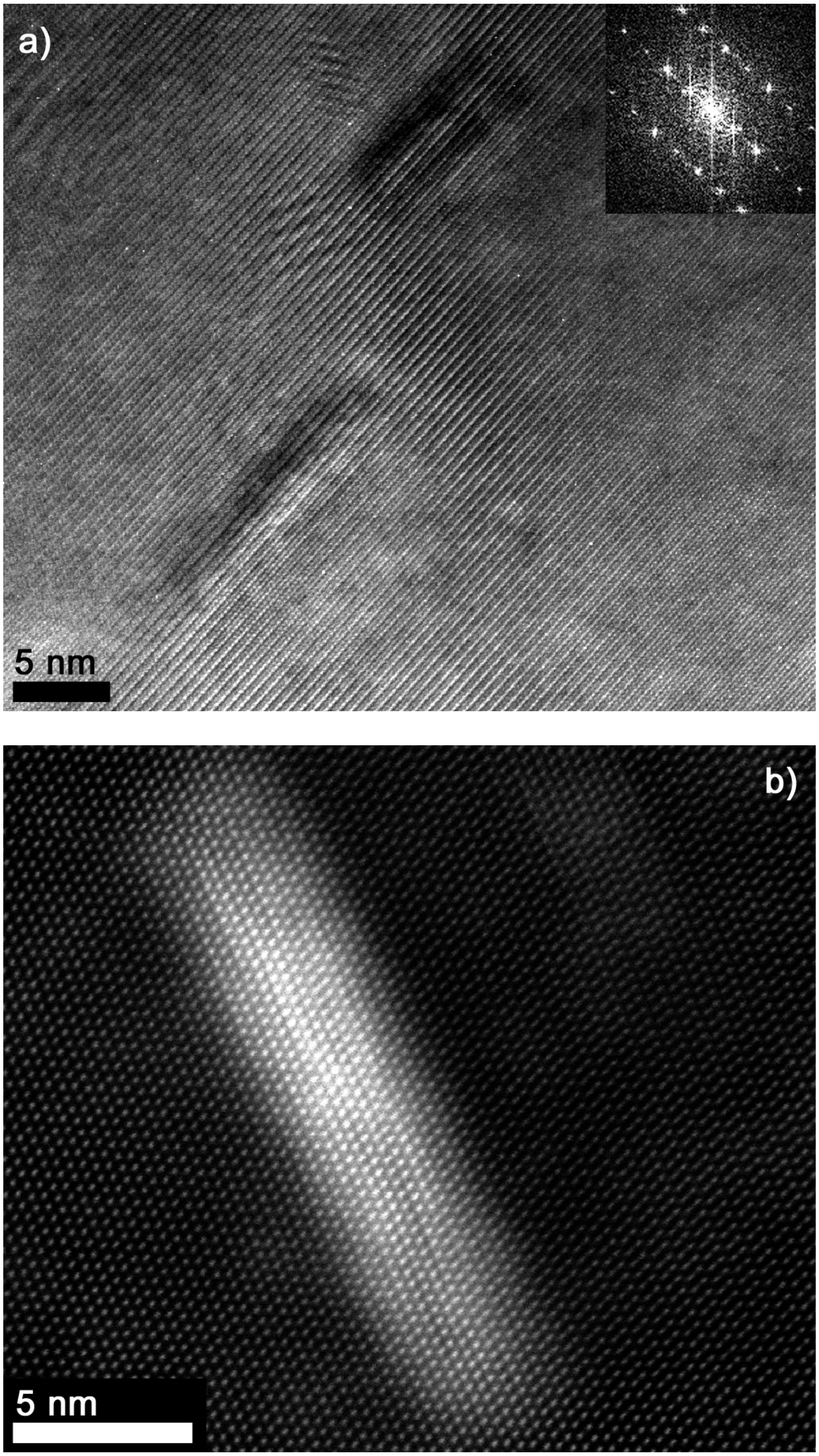

Figure 6-10: a) HR-TEM image and b) HAADF-STEM image of fine basal precipitates in peak-aged ZEX400 (aged 168 h at 180°C) from $\langle 11\bar{2}0 \rangle$ zone axis

HR-S/TEM observations of the fine basal precipitates in the peak-aged condition (images shown in Figure 6-10) reveal a fully coherent structure, which appears identical to the multi-layer precipitates observed after 3 h ageing. Only the size of the precipitates appears to have increased, to approximately 3-5 nm in thickness and 10-30 nm in average diameter. Observations of the precipitates in both conditions also show that some contain bands of bright and dark contrast parallel to the basal planes, as shown in Figure 6-11. This signifies that some atomic planes contain a higher amount of heavier solutes. The overall similarity between the fine basal plates in the peak-aged condition and the multi-layer precipitates found for 3 h ageing, suggests that they are the same phase for both ageing conditions.

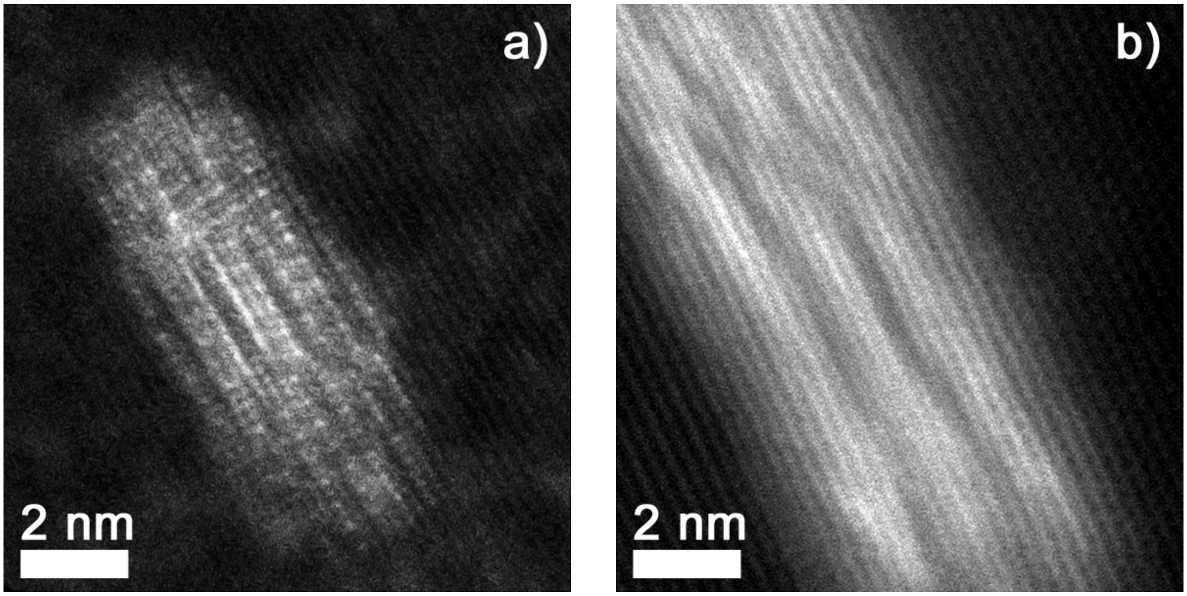

Figure 6-11: HAADF-STEM image of multi-layer basal precipitates in ZEX400 a) aged 3 h at 180°C from $\langle 10\bar{1}0 \rangle$ zone axis, and b) aged 168 h at 180°C from $\langle 11\bar{2}0 \rangle$ zone axis, showing dark bands parallel to the basal planes.

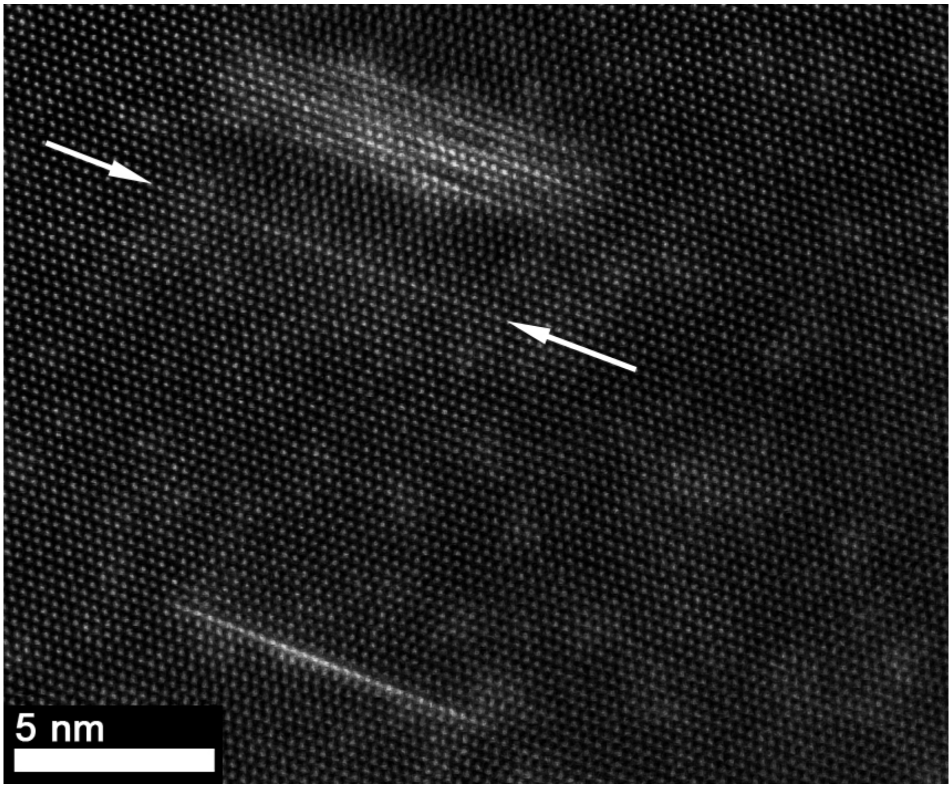

Figure 6-12: Faint monolayer GP zone (indicated by arrows) next to a growing multi-layer precipitate in ZEX400 aged 3 h at 180°C, $\langle 11\bar{2}0 \rangle$ zone axis.

After 3 h of ageing at 180°C both monolayer and multi-layer GP zones are observed, but in the peak-aged condition (168 h of ageing) the monolayer GP zones are no longer present. Instead, the fine basal plate precipitates are found to be entirely composed of the multi-layer GP zones. Therefore, it is suggested that the GP zones evolve from the monolayer form to the multi-layer form as ageing progresses. Given the lack of Mg-Zn type β'_1 or β'_2 precipitates found coincident with the monolayer GP zones (i.e. after 3 h of ageing), it follows that the matrix surrounding the monolayer GP zones will still be supersaturated with Zn. Therefore, it is possible that the transition from monolayer GP zone to multi-layer GP zone occurs in order to accommodate additional Zn. It is hypothesized that this change in local chemistry of the GP zone by enrichment in Zn, relative to Ca, leads to preferential growth of the GP zones along the

$[0001]_{Mg}$ direction. Furthermore, by accommodating additional Zn solute, the matrix adjacent to the multi-layer GP zones would decrease in Zn content, compared to the matrix surrounding the monolayer GP zones. Such local gradients in matrix composition can then cause volume diffusion of Zn towards the growing multi-layer GP zones. Additionally, the fine basal plates may grow preferentially compared to the monolayer GP zones due to the Gibbs-Thomson effect [140], according to which the lower solubility of both Ca and Zn solute in the matrix adjacent to the larger precipitates can drive gradual dissolution of smaller monolayer GP zones. Figure 6-12 provides some evidence for such dissolution of a monolayer GP zone at the expense of a growing multi-layer GP zone. In this figure, a monolayer GP zone appears faint (and therefore contains little solute) when found next to a multi-layer precipitate. The GP zone in Figure 6-12 could therefore be losing solute as it dissolves, which is then incorporated into the adjacent multi-layer GP zone as it grows.

The dark bands found in some of the multi-layer precipitates, especially in the peak-aged condition, may signify a change in the internal structure of those precipitates, as the solute arrangement adjusts to the higher Zn content in order to reach the next step of metastable equilibrium. It is possible that these precipitates then act as a precursor to a precipitate phase with a different structure than the matrix. Based on thermodynamic calculations, the equilibrium form of this phase may be the $Mg_6Ca_2Zn_3$ phase. It is noted that this phase has a higher Zn:Ca ratio than the monolayer GP zones (27 at% Zn and 18 at% Ca in the stoichiometric $Mg_6Ca_2Zn_3$ phase, compared to 33 at% for Ca and Zn together in the monolayer GP zone). Therefore, the multi-layer GP zones could act as a transitional form between the monolayer GP zones and the $Mg_6Ca_2Zn_3$ phase, which arises as the Zn content of the precipitate increases. The full precipitation sequence in the ZEX400 alloy is further described in the following subsection.

6.3.4 Precipitation Sequence in the ZEX400 Alloy

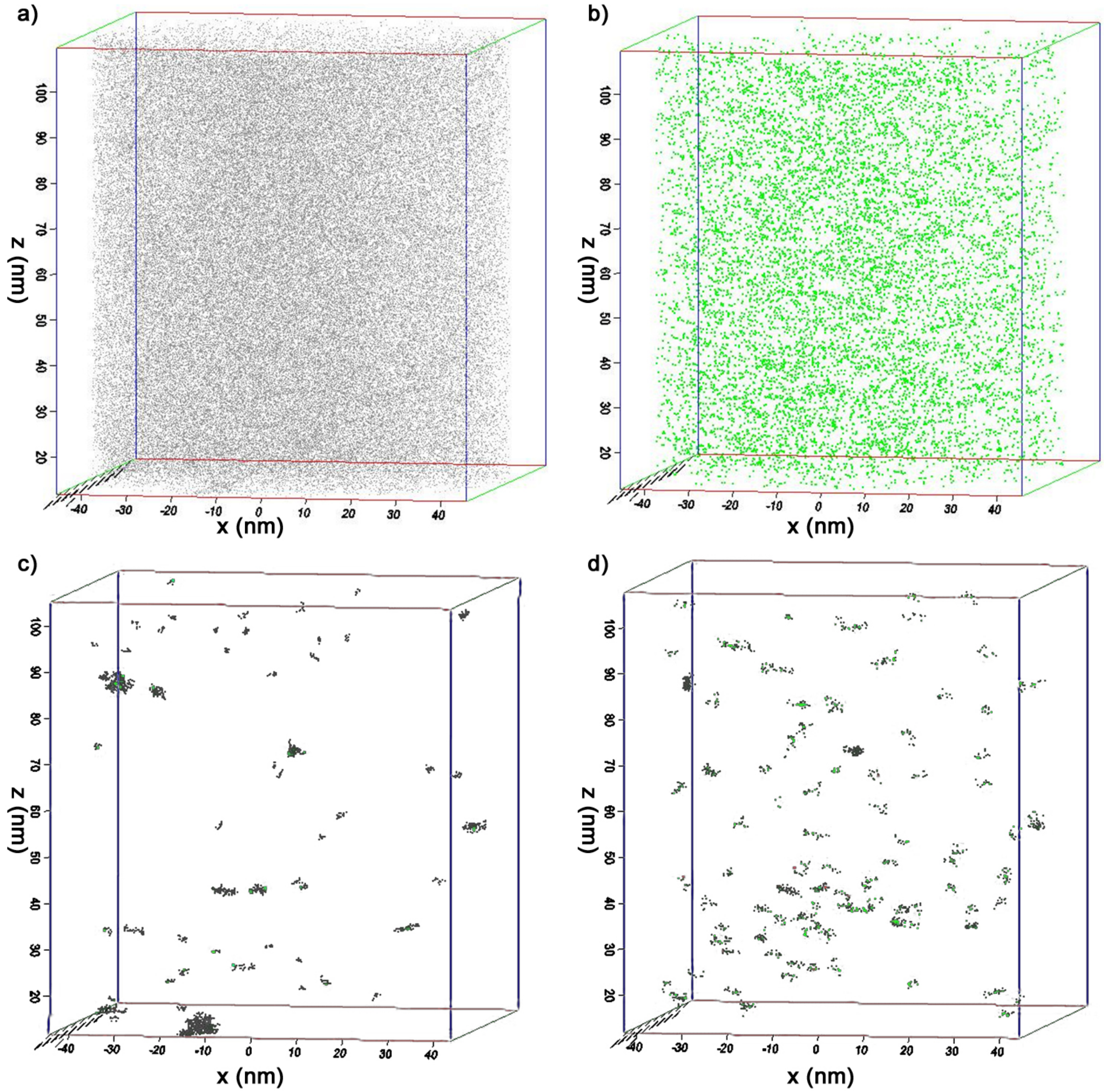

Figure 6-13: APT results for ZEX400 alloy aged 168 h at 100°C, showing atom maps for a) Zn, b) Ca, and the results of clustering calculations for c) Zn-rich clusters, d) Ca-Zn clusters. APT reconstruction and analysis performed by G. Sha.

Further insight into the precipitate evolution and hardening behaviour of the ZEX400 alloy can be obtained by full investigation of the precipitation sequence leading to the peak-aged condition. The earliest precipitates to form during ageing are suggested to be the monolayer GP zones. The origins of the monolayer GP zone precipitation can be attributed to early-stage clustering. APT study of the ZEX400 alloy in an under-aged condition (168 h at 100°C) provides evidence of solute clustering, as shown in Figure 6-13. The analysis indicates two types of clusters: Zn-rich clusters (Figure 6-13c) and Ca-rich, Ca-Zn clusters (Figure 6-13d). The Ca-Zn clusters are found in a higher number density and appear to be more uniformly distributed. Table 6-3 lists the compositions of the clusters found from the APT results shown in Figure 6-13. It should be noted that some Ca was found in the Zn-rich clusters as well, but the Ca:Zn ratio in those clusters is significantly lower than the same ratio in the Ca-Zn clusters. Both types of clusters contain only trace levels of Ce. This lack of significant Ce clustering can be attributed to the very low Ce solute supersaturation in the alloy. These findings indicate a tendency for co-segregation between Ca and Zn, which confirms that the GP zone precipitation is primarily due to interactions of Zn and Ca solutes. Furthermore, the findings for two types of clusters (Zn-rich and Ca-Zn) are consistent with the two major compositions of precipitates found in the peak-aged alloy (Zn-rich β'_1 and β'_2, and Ca-containing fine basal precipitates).

Table 6-3: Cluster composition data calculated from the APT results shown in Figure 6-13.

	Zn (at%)	Ca (at%)	Ce (at%)
Zn Clusters	9.36 ±0.217	0.24 ±0.036	0.028 ±0.012
Ca-Zn Clusters	2.61 ±0.074	1.34 ±0.053	0.019 ±0.006

It is also worth comparing the precipitate evolution in the ZEX400 alloy with that of the ZEX200 alloy, in order to better understand the role of Zn on the precipitation sequence. TEM observations show that in the microstructure of the ZEX200 alloy, the precipitates are almost entirely plates on the basal planes, as found when aged for either 3 h or 168 h at 180°C (shown in Figure 6-14). Only the presence of sparsely-dispersed large basal plates, as indicated in Figure 6-14b, distinguishes the over-aged condition. These large basal plates are generally 50-100 nm in diameter and 25-40 nm thick, with an appearance that is unlike that of the β'_2 phase. It has not been determined by direct observation if the finer precipitates in the ZEX200 alloy are monolayer or multi-layer GP zones, as seen in the ZEX400 alloy. However, streaking is observed in the diffraction patterns for the ZEX200 alloy, even after 168 h of ageing (over-aged condition), which is characteristic of the monolayer GP zones. This can be seen parallel to the [0001] direction at $1/3\{11\bar{2}0\}$ and $1/3\,\{11\bar{2}0\}$ in the $\langle 10\bar{1}0\rangle$ zone axis SADP for the over-aged condition, shown in Figure 6-14b. It should also be noted that such streaking was also observed for 3 h of ageing, but is less apparent in the $\langle 11\bar{2}0\rangle$ zone axis SADP shown in Figure 6-14a. The SADP streaking suggests that the monolayer GP zones are present in this alloy even after extended ageing. However, this does not preclude the presence of the multi-layer GP zones, as observations of the ZEX400 alloy show that both of these precipitates can coincide in the microstructure.

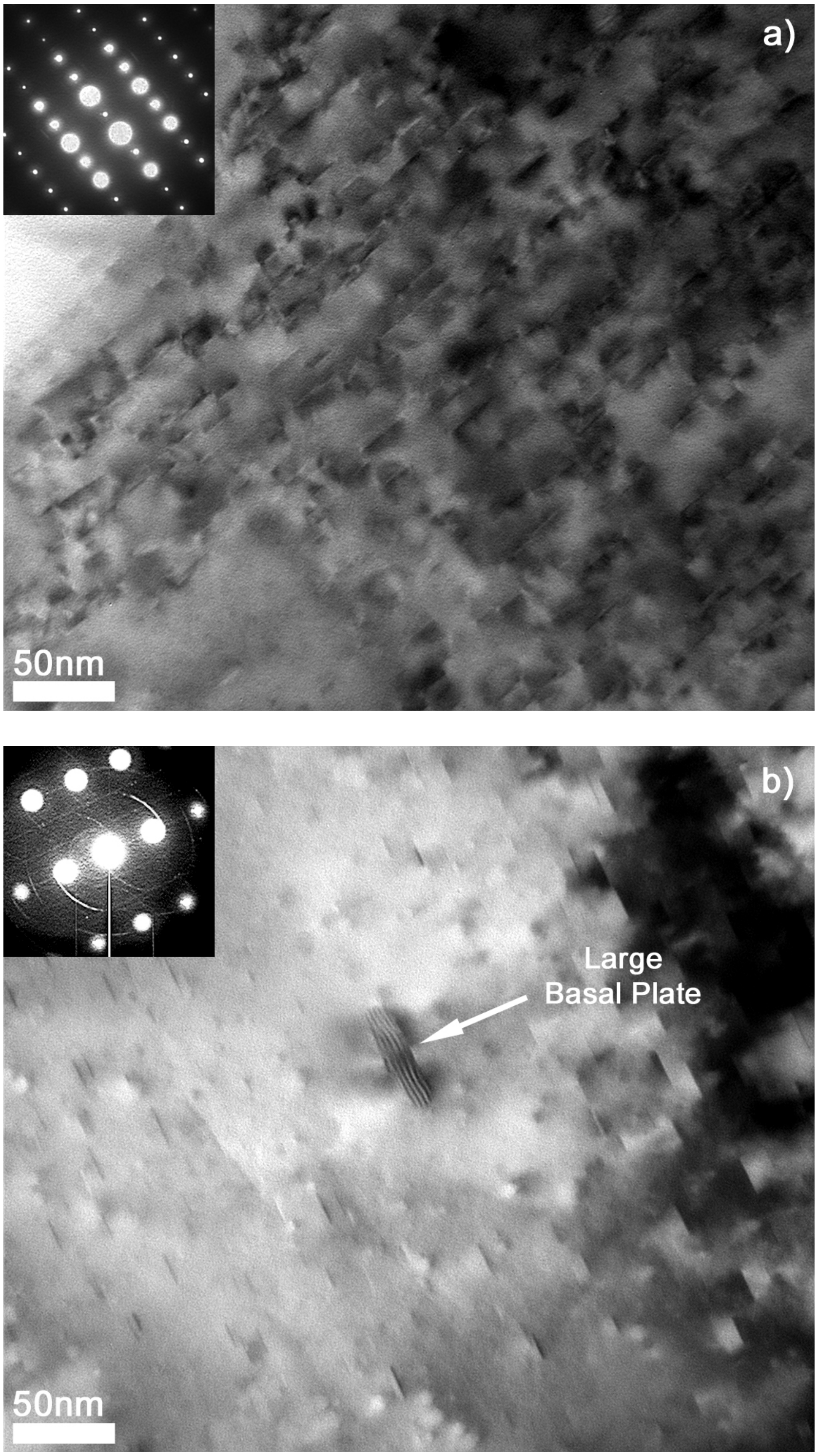

Figure 6-14: Bright-field TEM micrographs of ZEX200 alloy a) aged 3 h 180°C, $\langle 11\bar{2}0\rangle$ zone axis, b) aged 168 h 180°C, $\langle 10\bar{1}0\rangle$ zone axis, with streaking apparent in the SADP inserts. Observations performed by P. Donnadieu.

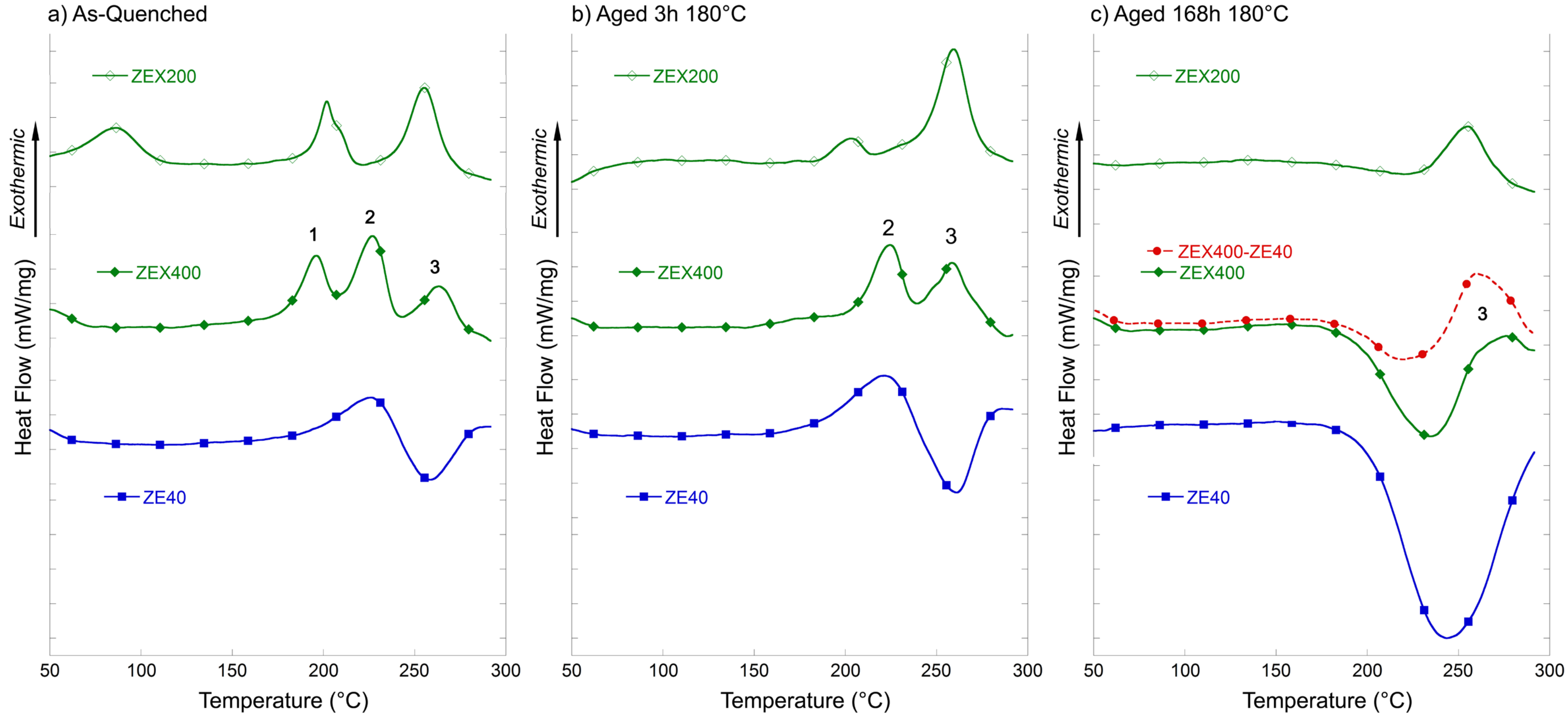

Figure 6-15: DSC curves for ZEX200, ZEX400, and ZE40 alloys a) in the as-quenched condition, b) after 3 h ageing at 180°C, c) after 168 h ageing at 180°C, exothermic peaks for ZEX400 alloy are labeled according to their descriptions in the text. c) also includes the results of subtracting the ZE40 result from the ZEX400 trace, as described in the text.

Combining the microstructural observations with DSC analysis can reveal the overall precipitate evolution in the ZEX400 alloy. In addition, the DSC results for the ZEX400 alloy are compared with those for the ZEX200 and ZE40 alloys in order to reveal the effects of Zn level and Ca content, respectively. It should also be noted that DSC analysis on the ZX40 and Z4 alloys (not shown) revealed very similar results to the ZEX400 and ZE40 alloys, respectively, which indicates that any potential effects of Ce on precipitation are not apparent from the DSC analysis conducted in this work.

Figure 6-15a shows the DSC result for the ZEX400 alloy, tested following quenching from the solutionizing temperature. The DSC curve shows three main peaks, centred at approximately 1) 200°C, 2) 225°C, and 3) 260°C. It is notable that peaks 1 and 3 appear in temperature ranges similar those for peaks which occur in the DSC result for the ZEX200 alloy, while peak 2 closely matches a peak found in the results for the ZE40 alloy. The DSC traces can also be compared for different ageing conditions. Figure 6-15b shows the DSC results for the ZEX400, ZEX200, and ZE40 alloys when tested after 3 h of ageing at 180°C, and the DSC results after 168 h of ageing (peak-ageing for ZEX400) are given in Figure 6-15c. For the ZEX400 alloy after 3 h of ageing, it is notable that the first peak is no longer present in the DSC results. This signifies that the precipitation transformation associated with peak 1 is complete after 3 h of ageing at 180°C. Based on the TEM observations of the ZEX400 microstructure for that ageing time, peak 1 therefore represents the formation of the fine basal precipitates (i.e. monolayer and multi-layer GP zones). This is consistent with observations that a similar peak exists for the ZEX200 alloy but not for the ZE40 alloy, as the ZEX200 alloy also forms these precipitates, while the ZE40 alloy does not.

A comparison between different alloys and ageing conditions also allows for peak 2 to be identified. As a peak at that temperature is not exhibited by the ZEX200 alloy, but is found in the as-quenched and 3 h aged DSC results for the ZE40 alloy, peak 2 can be attributed to β'_1 and potentially β'_2 phase precipitation, as those are the only precipitates observed to form in the ZE40 alloy during ageing at 180°C. It also follows that this peak is relatively identical in the DSC results of the ZEX400 alloy for both the as-quenched and 3 h aged conditions, as the β'_1 and β'_2 phases are not observed in the microstructure (i.e. have not formed yet) for the sample aged 3 h at 180°C.

Peak 3 is more ambiguous in its representation in the microstructure as it occurs at a significantly higher temperature than the current ageing temperature, and therefore the transformation it represents is less likely to take place even during 168 h of ageing at 180°C. This is supported by the DSC results for the alloys after that ageing time, as peak 3 is still observed for both the ZEX400 and ZEX200 alloys. It is worth noting however that for the ZEX400 alloy, this peak is partially obscured by an overlapping endothermic peak at 250°C, which is seen most clearly in the DSC trace for the ZE40 alloy. This endothermic peak is attributed to the dissolution of the β'_1 and β'_2 phases, as the temperature at which it starts is identical to the calculated MgZn phase solvus of 225.06°C [127]. To de-convolute peak 3 from the overlapping endothermic peak, the DSC result for the ZE40 alloy, which represents only MgZn phase evolution, is subtracted from the result for the ZEX400 alloy, after normalizing for the amount of MgZn phase predicted by thermodynamic calculations. The formula for obtaining the subtracted result is given as follows:

$$Q(T)_{Sub\ Result} = Q(T)_{ZEX400} - Q(T)_{ZE40}\left(\frac{\Delta X_{ZE40}}{\Delta X_{ZEX400}}\right)_{MgZn}$$

where $Q(T)$ is the recorded heat flow, and ΔX is the amount of MgZn predicted to form during ageing at 180°C, given as a mol fraction of the total amount of alloy. The subtracted result is also plotted in Figure 6-15c, where it exhibits a clear exothermic peak, coincident with that of peak 3 from the results for the as-quenched and 3 h aged conditions, and with the corresponding peak in the ZEX200 alloy. It should be noted that the small endothermic peak prior to peak 3 in the subtracted result may indicate that the thermodynamic calculations underestimate the amount of MgZn phase in the ZEX400 alloy. The observation of peak 3 in the ZEX200 alloy DSC results but not in the ZE40 results indicates a transformation involving Ca. Thermodynamic calculations predict the $Mg_6Ca_2Zn_3$ equilibrium phase to form in both the ZEX200 and ZEX400 alloys, even at the temperature at which peak 3 is observed. In chapter 4, DSC analysis is presented on a sample of XZ21 alloy which is aged for 24 h at 370°C prior to DSC testing, in order for the DSC results to only represent $Mg_6Ca_2Zn_3$ phase formation. A comparison of this DSC analysis to the current results for the ZEX200 alloy in the as-quenched condition is presented in Figure 6-16. From this comparison, it can be seen that the ZEX200 DSC curve is nearly identical to that of the aged XZ21 alloy. This suggests that peak 3 represents the formation of the equilibrium $Mg_6Ca_2Zn_3$ phase. The results also provide additional evidence that the monolayer and multilayer GP zones that form in the ZEX400 alloy represent a transition phase in the precipitation sequence for the equilibrium $Mg_6Ca_2Zn_3$ phase. It is also notable that the size of the peak in the DSC result for the ZEX200 alloy is observed to decrease after 168 h of ageing, signifying that some $Mg_6Ca_2Zn_3$ phase may have formed in the over-aged condition. It is therefore likely that the large basal plate precipitates found in the over-aged microstructure (shown in Figure 6-14b) may be the $Mg_6Ca_2Zn_3$ phase. Peak 3 does not appear to change in size however for the ZEX400 alloy, which follows as the same large basal plate precipitates are not observed in that alloy.

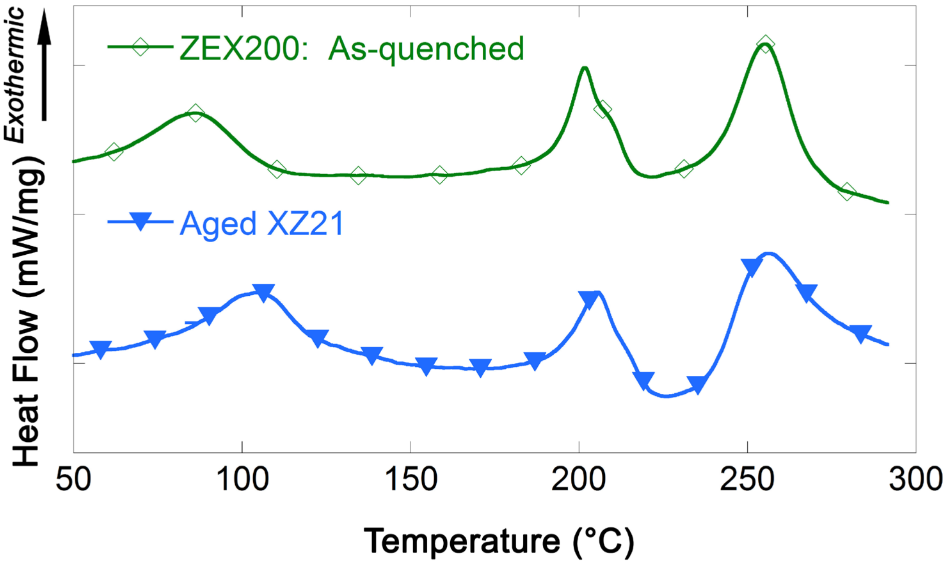

Figure 6-16: DSC results for the as-quenched ZEX200 alloy, and the XZ21 alloy aged 24 h at 370°C.

It should also be noted that while the GP zones are expected to be preceded by clustering, no evidence for this is seen in the DSC results for the ZEX400 alloy. However, an exothermic peak centered at 80°C is observed for the ZEX200 alloy, which can be attributed to clustering. Clustering is still expected as part of the precipitation sequence of the ZEX400 alloy, as indicated by the APT results shown in Figure 6-13. That no DSC peak is recorded for clustering in ZEX400 alloy, but is for the ZEX200 alloy, can be attributed to a greater degree of clustering in ZEX200, due to its higher Ca:Zn ratio.

The sequence of precipitation in the ZEX400 alloy during ageing at 180°C up to the peak-aged condition is therefore proposed to be:

$$\text{Clusters} \rightarrow \text{Monolayer GP Zones} + \text{Multi-layer GP Zones} \rightarrow$$
$$\beta'_1 \text{ Rods} + \beta'_2 \text{ Plates} + \text{Multi-layer GP Zones}$$

Another important consideration in the precipitate evolution of the ZEX400 alloy is the refinement in the precipitation of the β'_1 rods. Bhattacharjee et al. [40] have reported the possibility of a refined β'_1 phase distribution by heterogeneous nucleation on GP zones, which later evolve into β'_1 and β'_2, for Mg-Zn microalloyed with Ag, Ca, and Ag-Ca. In the current work the multi-layer GP zones are noted to persist throughout β'_1 and β'_2 phase formation (i.e. into the peak-aged condition) and therefore do not transition into those phases. However, the presence of the fine basal precipitates in the matrix could still facilitate heterogeneous precipitation of β'_1 through lattice strain effects. Preferential nucleation at the uniformly-distributed fine basal precipitates could therefore lead to a refinement of the β'_1 phase distribution as well.

As a final note on the role of Ce during precipitation hardening, while the clustering, TEM, and DSC analysis do not identify a direct role for Ce in promoting hardening, a slightly increased hardness is measured for the ZEX400 alloy compared to the ZX40 alloy. It appears that this hardening occurs mostly during the early stages of ageing (< 1 h at 180°C). The exact method by which Ce produces this slight hardening increase is difficult to directly determine due to the very low Ce solute content in the alloys, and remains unclear. It is possible that the Ce solute does produce some clustering or precipitation, but so non-uniformly as to remain undetected by TEM or APT investigations. In particular, Ce may form some small secondary phase particles, as observed in chapter 5, or Ce solute may be incorporated into the GP zones or fine basal plates as an oversized solute similar to Ca. Thermodynamic calculations also suggest that the presence of Ce may slightly alter the solubility limits of Ca and Zn, and thus indirectly affect precipitation. However, regardless of origin, the overall effect is small compared to the effects of Zn and Ca.

6.4 Summary

The effect of Ce-Ca microalloying additions on the precipitation hardening behaviour of Mg-Zn alloys is studied by analyzing the age-hardening response, microstructures, and precipitate evolution. It is found that:

- Higher Zn content increases the age-hardening response, primarily due to precipitation of the β'_1 phase, which forms rods oriented along the c-axis.
- Ce does not significantly affect hardening, although a very small increase in the age-hardening response of the ZEX400 alloy compared to the ZX40 alloy is observed. The exact role of Ce in producing this effect remains ambiguous.
- Ca additions greatly improve the hardening by promoting a refinement of the β'_1 precipitates and their distribution, and the formation of fine-scale basal precipitates.

The most enhanced precipitation hardening response during ageing at 180°C, was observed for the ZEX400 alloy, which contained higher Zn content and the Ce-Ca microalloying additions. In that alloy, analysis of the precipitates reveals:

- The main hardening precipitates are determined to be the β'_1 precipitate rods, and fine precipitates on the basal planes, due to the high numbers and low inter-particle spacings observed for these phases.

- The composition of the β'_1 rods was close to that of MgZn, and contained no significant levels of the Ce or Ca microalloying elements.

- The fine basal plates in the peak-aged condition are revealed to be several atomic layers thick along the $[0001]_{Mg}$ direction. The structure of these precipitates remains undetermined, but is observed to be fully coherent with the matrix and very similar to that of monolayer GP zones, but built up over several basal planes. These precipitates are therefore identified as multi-layer GP zones.

- The monolayer GP zones, found only in the under-aged condition, are suggested to contain both Zn and Ca, due to their relative atomic sizes. It is proposed that the multi-layer GP zones form from the monolayer GP zones in order to incorporate additional Zn solute.

Analysis of the precipitation sequence and phase evolution in the ZEX400 alloy shows that:

- Precipitation commences with the clustering of both Zn, and Ca-Zn during the early stages of ageing. These two cluster types are indicative of the two hardening precipitate types (Ca-containing fine basal plates and Zn-rich β'_1 rods) that form at later stages of ageing.

- As ageing progresses, monolayer and multi-layer GP zones form, which causes early hardening of the alloy. With continued ageing, increased formation of the multi-layer

GP zones leads to the eventual disappearance of the monolayer GP zones from the microstructure.

- As the peak-aged condition is achieved, the β'_1 rods and β'_2 plates form in the alloy. It is suggested that the β'_1 rods form with a refined distribution due to heterogeneous nucleation at the finely-distributed basal plate precipitates already in the matrix.
- Evidence is found that the fine basal precipitates in the ZEX400 alloy may be a transition phase in the precipitation sequence for the $Mg_6Ca_2Zn_3$ equilibrium phase.

As seen by the results of this chapter, the enhanced precipitation hardening capabilities of the ZEX400 alloy highlight the potential of Ce-Ca microalloying elements added to Mg-Zn in high-strength magnesium alloy development.

7 Evaluation of Grain Boundary Precipitation and Solute Segregation in an Mg-Zn Alloy with Ce-Ca Microalloying Element Additions

While the preceding chapter details the general precipitation characteristics of Mg-Zn microalloyed with Ce-Ca, the following chapter focuses on the effects of the Ce-Ca microalloying elements on the behaviour of solutes and the evolution of precipitates at and near grain boundaries in the ZEX400 alloy during ageing.

7.1 Introduction

The precipitation hardening of magnesium alloys is of significant interest for increasing alloy strength [147]. However, precipitation at and around grain boundaries in these alloys requires study, as grain boundary precipitation and the formation of corresponding precipitate-free zones (PFZ) can be detrimental to strength, ductility, and fracture toughness [152,153]. Mg-Zn based alloys, particularly those with microalloying additions (< 0.5 wt%), exhibit significant age-hardening responses [20,41,48,90]. It has also been observed that after aging, these alloys can form coarse grain boundary precipitates and associated PFZ [20,90]. Despite reports on grain boundary precipitation in Mg alloys, there is a lack of knowledge on the effects of alloying elements and composition on this phenomenon. The current research is the first focused effort to analyze this behaviour in a microalloyed magnesium alloy.

Segregation of solute atoms to grain boundaries has usually been studied in understanding solute drag effects related to annealing [154,155]. However, the knowledge of grain boundary segregation in relation to grain boundary precipitation during aging is not as well developed. In this chapter, solute segregation and precipitation both at grain boundaries and within grains are examined using APT and TEM. The focus of this study is on the ZEX400 alloy, which is a newly developed Mg-Zn based alloy with Ce-Ca microalloying additions. This alloy, as presented in chapter 6, shows a significant precipitation hardening response, as well as enhanced ductility and texture (see chapter 8) [156]. The roles of alloy chemistry, grain boundary segregation and early-stage decomposition of the solid solution on subsequent precipitate distributions are analyzed.

7.2 Experimental Methodology

The alloys examined in this work were prepared and solutionized given the parameters described in sections 3.1 and 3.2 respectively. TEM analysis is carried out according to the method described in section 3.4.3, and APT testing is performed as outlined in section 3.4.6. To quantify segregation from the APT results, Gibbs solute excess values were calculated from the integrated ion profiles according to references [124,157]. The Gibbs interfacial excess of solute *i* (Γ^i) is a function of the angle between the interface normal and the analysis volume axis (Φ), the cross-sectional area (A), the detector efficiency (η), the total number of ions (n_T), and the concentration of solute *i* in the total volume and in the matrix (C^i_{vol} and C^i_{matrix}), and is given by Equation 1 [124,157,158]. The detection efficiency of the LEAP 3000 Si is known to be ~55% [159].

$$\Gamma^i = \frac{\cos\Phi}{\eta A} n_T \left(C^i_{vol} - C^i_{matrix}\right) \qquad (7\text{-}1)$$

Cluster analysis was performed using the maximum separation method, with Ce and Ca selected as target solutes, the minimum cluster size of 6 solute atoms, the maximum 6-nearest-neighbour separation distance of 2.6 nm and an envelope distance of 2 nm to include all other surrounding atoms.

7.3 Results

The overall precipitation characteristics of the ZEX400 alloy at the grain boundaries and within the grains are examined by TEM analysis of samples aged at 180°C for 168 h (peak-aging), as presented in Figure 7-1. The microstructure contains the three major types of precipitates described in detail in chapter 6: 1) rod-like precipitates parallel to $[0001]_{\mathrm{Mg}}$, 2) large, thick plate precipitates on $(0001)_{\mathrm{Mg}}$ basal planes, 3) fine plates also on $(0001)_{\mathrm{Mg}}$ basal planes. Observations at the grain boundaries reveal an additional precipitate type: 4) coarse grain boundary precipitates. The rod-like precipitates are approximately 10-20 nm in diameter, and 100 nm to several hundred nanometers in length. These precipitates are present in high numbers. However, large plate precipitates, approximately 75-100 nm in diameter and 20 nm in thickness, are observed only occasionally. The morphologies of the rod-like precipitates and large plate precipitates are consistent with the b_1' and b_2' precipitates respectively, reported for binary Mg-Zn and Mg-Zn based alloys [42]. The fine basal plates are found in high numbers, as well. These plates range from 10-30 nm in diameter, with an apparent thickness of < 5 nm. Within the grains, the b_1' and b_2' precipitates and the fine plate precipitates all appear to be uniformly-distributed. The grain boundary precipitates, are generally oblate in shape, with their long axes along the direction of the grain boundary. EDS analysis of these precipitates, demonstrating only Zn peaks, suggest that they are Mg-Zn type phases (Figure 7-1d-f).

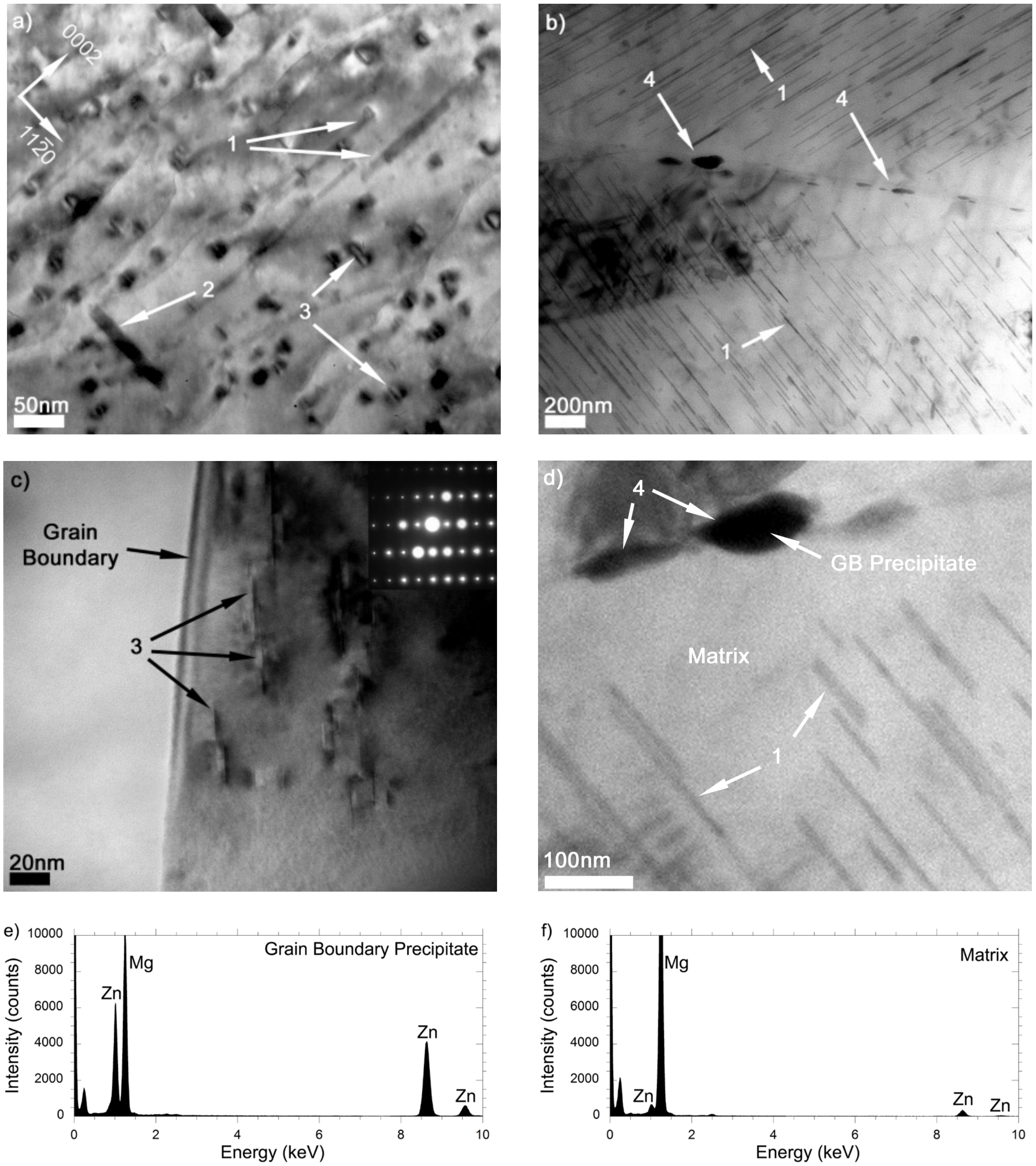

Figure 7-1: a-d) Bright-field TEM micrographs of ZEX400 alloy aged 168h at 180°C a) $\langle 10\bar{1}0\rangle$ zone axis showing general precipitate microstructure, b) grain boundary with apparent PFZ, c) $\langle 11\bar{2}0\rangle$ zone axis image showing fine basal precipitates adjacent to a grain boundary, d) PFZ and grain boundary precipitates. Precipitates are marked with numbers as listed in the text. EDS spectra for e) a grain boundary precipitate and f) the matrix, correspond to the locations identified in d). Observations for b,c performed by P. Donnadieu.

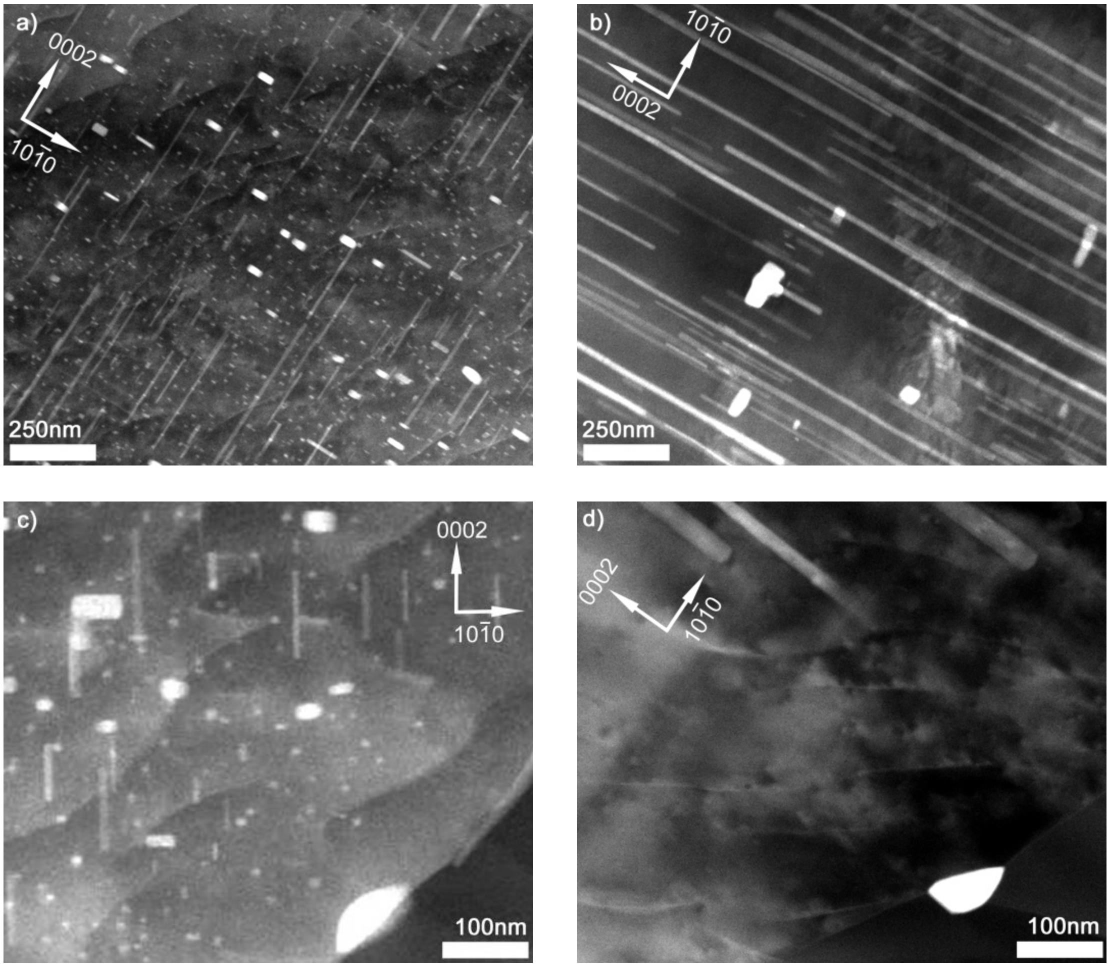

Figure 7-2: HAADF-STEM images comparing a) ZEX400 and b) Z4 alloys aged 168 h at 180°C, $\langle 11\bar{2}0 \rangle$ zone axis, with details of grain boundaries and PFZ presented in c) ZEX400 and d) Z4.

The grain boundaries are also accompanied by apparent PFZ, noticeable by a lack of rod-like precipitates. The origin of such PFZ is attributed to solute depletion, caused by the observed grain boundary precipitation [160]. However, detailed examinations of grain boundaries reveals these zones to not be entirely precipitate-free. The fine precipitate plates are observed to persist to within < 20 nm of the boundary (Figure 7-1c). Note that the fine basal plates are only clearly resolved with the electron beam close to parallel with the basal plane, which explains their apparent absence in Figure 7-1b,d. As the fine plates are homogeneously distributed throughout the material, the PFZ for the ZEX400 refers only to the lack of b_1' and b_2' precipitates.

Comparison of the precipitate distributions near the grain boundaries between the ZEX400 alloy and the binary Z4 alloy, both aged 168h at 180°C, clearly indicates that the microalloying additions serve to refine the precipitate distributions and reduce the size of the PFZ. This is shown by HAADF-STEM images in Figure 7-2, which reveal the precipitates in bright contrast to the matrix due to their relatively high solute content. It should be mentioned that the fine dotted and wavy contrast in Figures 4c and 4d is generated by surface artefacts produced during ion milling. The observed reduction in the PFZ for the ZEX400 alloy is due to a refinement in the b_1'precipitate rods and their distribution, and the high numbers of fine plate precipitates. As seen in Figure 7-2b, the b_1' precipitate rods in the binary alloy appear thicker and longer, and in a lower number density than in ZEX400 (Figure 7-2a). This results in a larger average distance from the grain boundary (i.e. width of the PFZ) of 250-750 nm in the Z4 alloy, compared to 100-200 nm as observed for the ZEX400. The absence of the fine basal precipitates in the Z4 alloy also leads the PFZ due to the rod precipitates to be truly devoid of precipitates, whereas the apparent PFZ in the ZEX400 alloy is mostly filled by the fine basal plates (Figure 7-2c and d).

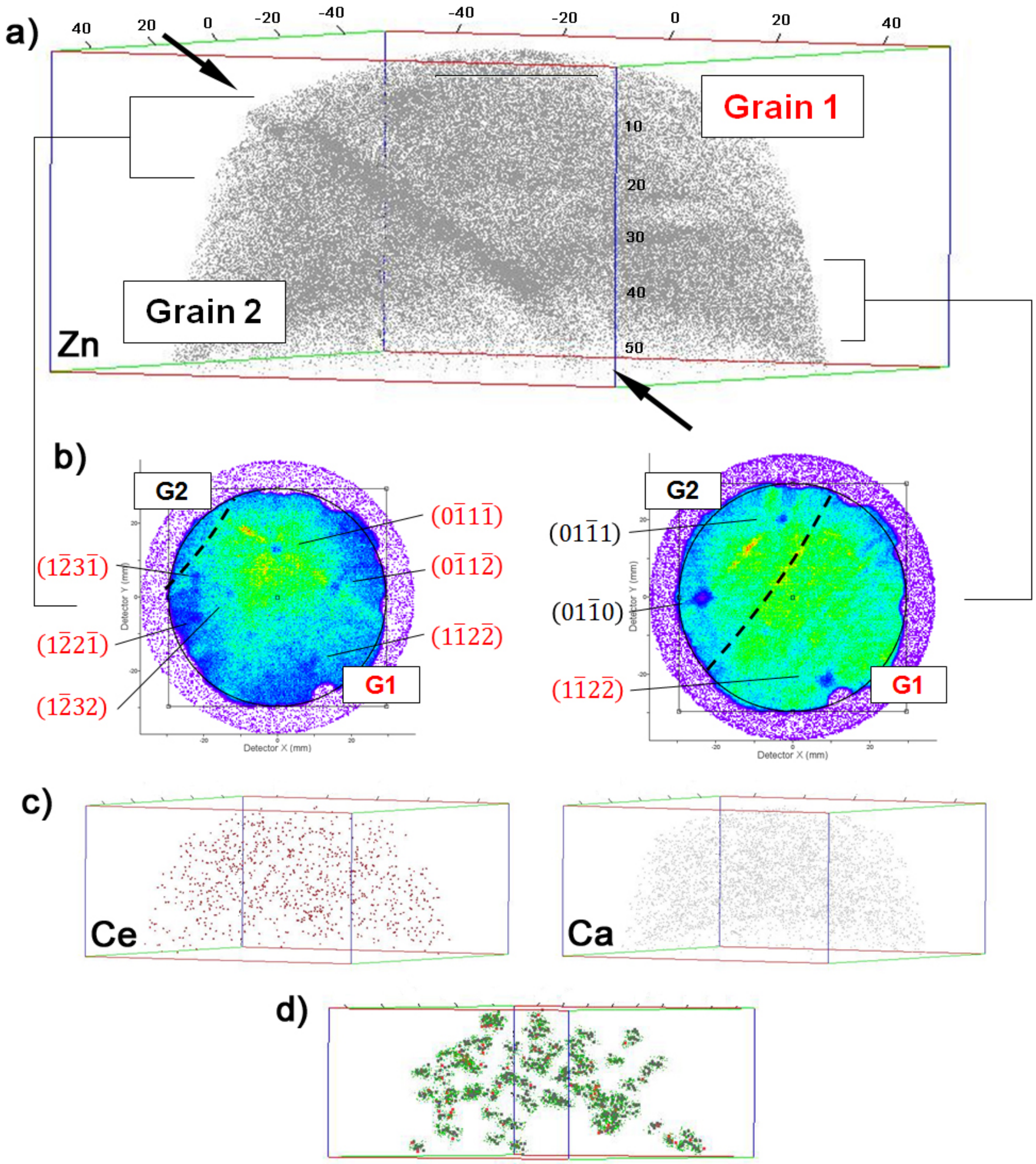

Figure 7-3: a) APT solute distributions for Zn in ZEX400 alloy, aged 168h at 100°C showing a grain boundary with Zn segregation (indicated by arrows). b) Detector desorption maps for different sections of the APT volume, showing indexed pole figures for each grain with the grain boundary indicated by a dashed line. c) Ce and Ca atom maps, d) Ca-containing solute clusters. APT reconstruction and analysis performed by G. Sha.

The solute behaviour at and near grain boundaries in the ZEX400 alloy is further investigated by APT analysis of a sample aged 168 h at 100°C, representing an under-aged condition. Figure 7-3a shows the Zn atom map for a sample of ZEX400 aged for 168h at 100°C. Due to the wide field of view of the LEAP instrument, crystallographic information is obtained from poles in the detector desorption maps to determine grain orientation and detect the presence of grain boundaries [125,161]. Select detector desorption maps from upper and lower sub-sets of the sample volume are shown in Figure 7-3b. Indexing the poles in these desorption maps as shown in Figure 7-3b confirms that the analysed volume contains two grains in different orientations. The grain boundary separating the two grains is observed exhibiting significant Zn segregation in the Zn atom map (Figure 7-3a). In contrast, the Ce and Ca maps (Figure 7-3c) show no clear segregation of those elements at the boundary. However, analysis of the APT data shows the presence of Ca-containing solute clusters present in the sample volume, as shown in Figure 7-3d.

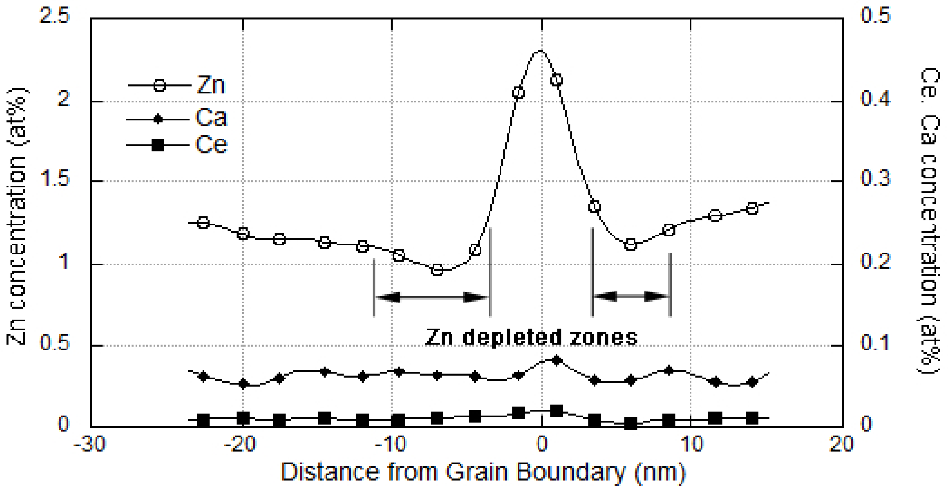

Figure 7-4: Solute concentration profiles normal to the grain boundary from APT analysis. Zn depleted zones are estimated based on points of inflection adjacent to the grain boundary.

The solute segregation behaviour to the grain boundary is measured using concentration profiles crossing the boundary, as shown in Figure 7-4. These profiles are obtained from a cylindrical volume normal to the boundary of 40 nm length and 15 nm radius. The Zn concentration at the grain boundary is noticeably enriched, and Zn-depleted zones, about 5-10 nm wide, are observed on either side of the boundary. It is noted here that the spread of Zn at the GB is likely due to the local magnification effect of the GB during field evaporation [124]. In contrast, Ce and Ca do not show clear segregation to the grain boundary and instead remain at relatively constant matrix-level concentrations, which is consistent with observations from the solute distribution maps in Figure 7-3c. It should be noted that TEM analysis performed on samples aged for 168h at 100°C detected no resolvable grain boundary precipitates, suggesting that the APT results represent solute segregation rather than well-developed grain boundary precipitation.

Table 7-1: Calculated element concentrations in the APT analysis volume, and resultant Gibbs interfacial excess values.

	Zn (at%)	Ca (at%)	Ce (at%)
Grain boundary	2.18 ± 0.178	0.073 ± 0.033	0.019 ± 0.017
Matrix C^{i}_{matrix}	1.16 ± 0.046	0.062 ± 0.011	0.010 ± 0.004
Gibbs Excess G^{i} (atoms / cm^2)	2.01 x 10^{13}	8.30 x 10^{10}	2.84 x 10^{11}

Gibbs solute excess values at the grain boundary are calculated to quantify the solute segregation. These are again taken using the cylindrical analysis volume normal to the boundary, which has a cross-sectional area of 706.9nm^2, and contains approximately 6.1 x 10^4 ions in total. The matrix and grain boundary compositions, and the calculation results, are listed in Table 7-1. These results confirm that Zn exhibits clear grain boundary segregation, relative to Ce and Ca. It is notable that in the calculation for Ce, the very low solute content leads to a high level of uncertainty.

7.4 Discussion

The refinement of the PFZ (i.e. compared to the binary Z4 alloy) due to the microalloying additions in the ZEX400 alloy can be understood by considering the differing solute segregation behaviours of the elements present in the matrix during ageing. However, to fully comprehend how the refined microstructure near the grain boundaries is produced by the microalloying additions, it is important to first examine how these differences in solute segregation originate. It is well known that for solute atoms with different atomic sizes from the solvent, segregation to grain boundaries can decrease the system free energy by reducing matrix lattice strain [162]. However in the current alloy, only Zn, with an atomic radius smaller than Mg (1.379Å and 1.598Å [151]), segregates to grain boundaries, while there is no observed segregation for oversized Ca and Ce (atomic radii of 1.970Å and 1.818Å [151]). This indicates that atomic size difference is not the only factor controlling the segregation of solutes to grain boundaries. We propose that two other factors: (a) supersaturation level and (b) clustering during early-stage bulk decomposition, also contribute to the observed segregation behaviour.

The grain boundary concentration of a solute is considered to be proportional to its bulk concentration [154]. The APT results in Table 7-1 show that Zn is at a much higher level in the matrix than the microalloying elements. The free energy considerations further suggest that a high supersaturation will increase the driving force to reject solute from the matrix. While this may increase the driving force for precipitation, when homogeneous precipitation is limited by a high energy barrier for nucleation, a high supersaturation may promote segregation/precipitation on grain boundaries. As shown in Table 7-2, the calculated supersaturation for Zn in ZEX400 at 100°C is about 10 and 10^4 times larger than those for Ca, and Ce, respectively, thus dictating a higher level of grain boundary segregation for Zn.

Table 7-2: Solute supersaturation levels in HCP-Mg for ZEX400, calculated according to methodology described in section 3.6.

Solute	Supersaturation (ΔX in at%)	
	100°C	100°C
Zn	0.891	0.891
Ce	1.99×10^{-5}	1.99×10^{-5}
Ca	0.097	0.097

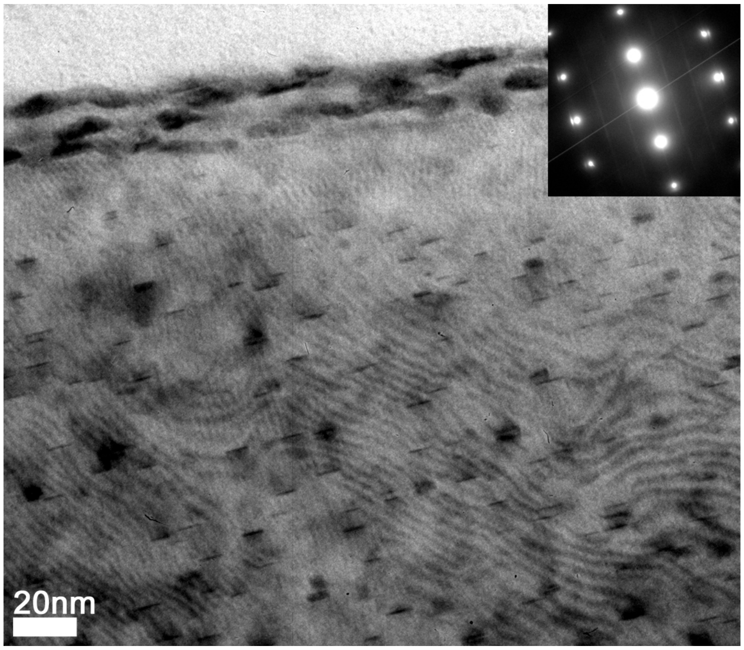

Figure 7-5: Bright-field TEM image of ZEX400 alloy aged 3 h at 180°C showing fine basal plates adjacent to the grain boundary, and small grain boundary precipitates, $\langle 10\bar{1}0 \rangle$ zone axis.

Analysis of the APT data also suggests that clusters of Ca and/or Ca-Zn have formed across the grains of the sample aged 168h at 100°C (Figure 7-3d). This result indicates that unlike for Zn, homogeneous nucleation may be favourable for the majority of the Ca solute, compared to grain boundary segregation/precipitation. Considering the fine spacing between clusters, migration of Ca to growing clusters may be preferable over longer-range diffusion to the grain boundary during this ageing treatment. It should be noted that no evidence from APT is found for Ce clustering, suggesting that Ce remains in solid solution, and the lack of Ce grain boundary segregation is due to its low concentration/supersaturation.

The different behaviours of Zn and Ca solute observed in the APT results give rise to the precipitate and precipitate distributions found by TEM analysis of the alloy when aged at 180°C. The high tendency of Zn to segregate to the boundaries while depleting the adjacent matrix of Zn solute leads to the observed Zn-rich grain boundary precipitates, and the apparent PFZ. On the other hand, as the Ca solute more readily forms clusters than segregates to the boundary, this can lead to the homogeneous distribution of fine precipitate plates observed in the ZEX400 alloy. TEM observations of the ZEX400 alloy aged 3 h at 180°C reveal that at this early stage of ageing, the fine basal precipitates have already formed, as shown in Figure 7-5. It can also be seen that at this ageing time, small grain boundary precipitates have formed, while no b_1' and b_2' precipitates are yet observed in the matrix. These observations are indicative of the higher nucleation rate for Zn-rich precipitation at the grain boundaries. Furthermore, the presence of the fine basal precipitates, which are uniformly-distributed in the grain and near the grain boundary, also suggest a higher nucleation rate for these phases compared to the b_1' and b_2' precipitates, which can be linked to the clustering tendencies of Ca. As discussed in detail in chapter 6, the presence of the fine basal plate precipitates in the matrix may positively influence subsequent nucleation of the b_1' rods through coherency strains on the matrix lattice, and thereby refine the b_1' distribution. It is further proposed here that this refinement of the b_1' distribution also serves to reduce the apparent PFZ for the b_1' in the peak-aged condition, compared to the binary Mg-Zn alloy.

Further details on the nature of the fine basal plate precipitates observed in the current work are provided in chapter 6. The current TEM evidence suggests that the current fine basal plates originate as monolayer GP zones, such as is consistent with the observed streaking parallel to the [0001] direction at $1/3\{11\bar{2}0\}$ and $2/3\{11\bar{2}0\}$ in the $\langle 10\bar{1}0\rangle$ zone axis SADP shown in Figure 7-5. These GP zones were reported by Ping et al. [97] and later by Oh-ishi et al. [53] to consist of a combination of undersized and oversized atoms with a negative enthalpy of mixing, which together promote nucleation by reducing misfit lattice strain. A similar solute size effect, with Ca/Ce having larger atomic diameters compared to Zn [151], is identified as an important factor in nucleation of the current monolayer GP zones. By extension, this factor is also important for the fine basal precipitates found in the peak-aged condition, as HR-TEM observations (see chapter 6) reveal the fine basal plate precipitates to be multi-layer GP zones, with a structure that is generally similar to that of the monolayer GP zones, but repeated over multiple basal planes.

In addition to the potential atomic size effects on formation of the fine basal precipitates (i.e. monolayer and multi-layer GP zones), we propose that quenched-in defects, as commonly reported in as-quenched Al alloys [163], significantly reduce the energy barrier for clustering and formation of these precipitates in ZEX400. Recent modelling of the earliest stage of clustering has shown that the formation of subcritical-size clusters in Al-Cu is triggered by the stress relaxation effect of quenched-in defects in the matrix [164]. Fallah et al. [164] have also shown that defect-mediated local reduction in the energy barrier for nucleation causes growth of these clusters to overcritical-size precipitates. Fallah and co-workers [165] have further demonstrated that the addition of a ternary microalloying element (Mg in the case of Al-Cu system) leads to an increased cluster nucleation rate, due to both energetic effects from the quenched-in defects and the alloy chemistry. Considering the common theoretical basis, it is proposed that the mechanisms mentioned above explain how the microalloying addition of Ca, which has a higher affinity to vacancies compared to Zn [141,142], can lead to the formation and uniform distribution of the Ca-containing clusters and fine basal precipitates observed in the current system.

The ability of such clustering to reduce PFZ behaviour has been recently been reported for aluminum alloys by Ogura et al. [166]. Those researchers suggested that for Al-Zn-Mg microalloyed with Ag, the enhanced binding of Ag to vacancies and alloying elements promoted clustering near the grain boundaries, and reduced the PFZ. In the current work, enhanced clustering due to Ca microalloying additions results in the fine precipitates forming directly up to grain boundaries. This homogeneous precipitation behaviour effectively prevents the formation of zones free from these precipitates in the ZEX400 alloy.

7.5 Summary

During ageing of an Mg-Zn alloy microalloyed with Ca-Ce at 180°C, coarse Zn-rich precipitates are observed to form on the grain boundaries. This grain boundary precipitation locally depletes Zn in the adjacent matrix, and leads to the formation of zones free of Mg-Zn type b_1' and b_2' precipitates. However, fine basal plate precipitates are also observed, which are uniformly-distributed, even in the apparent PFZ. These precipitates and their distributions result from the different segregation tendencies of the solutes, with only Zn found to significantly segregate to grain boundaries. The differences in segregation behaviour are mainly attributed to solute supersaturations, and enhanced early-stage bulk decomposition involving Ca. The tendency for Zn to segregate to grain boundaries results in the coarse grain boundary precipitate and subsequent PFZ formation, while the formation of Ca-containing clusters leads to the homogeneous precipitation of fine basal precipitates. It is also proposed that the fine basal precipitates act to refine the distribution of the b_1' precipitates, which reduces the apparent PFZ compared to the binary alloy. The enhanced nucleation rate and homogeneous distribution of the fine basal precipitates, even in regions near the grain boundaries, is further proposed to be positively influenced by quenched-in defects.

8 Improving Microstructure and Mechanical Properties of Mg-Zn Alloys by Ce-Ca Microalloying Element Additions

The following chapter details investigations into the effect of Ce-Ca microalloying additions on Mg-Zn alloy ductility, by examining the microstructure (i.e. grain size, secondary phase particles, and texture) and tensile properties of the alloys.

8.1 Introduction

The application of magnesium alloys is of high interest due to the potential weight savings offered by this low density material [6,7]. However, many current Mg-based alloys suffer from poor mechanical properties which limits their utilization [13,14]. Notably for the case of wrought magnesium, its use in application is hindered by the generally low room-temperature ductility and strength exhibited by many commercial alloys.

The lack of sufficient ductility for room-temperature forming of wrought magnesium is rooted in two causes: limited slip systems due to the HCP crystal structure, and strong alloy deformation texture [14,167]. The lack of available slip systems in magnesium at room-temperature is due to the dominance of basal $\langle a \rangle$ slip, which only gives two of the five independent slip modes required by the Taylor criterion for generalized ductile deformation, and does not produce any deformation along the $\langle c \rangle$ axis [61]. This lack of general formability is then exacerbated in wrought magnesium alloys by the strong textures typically produced in extruded or rolled material. This strong texture occurs as basal poles tend to align either normal to the extrusion axis or normal to the sheet plane during rolling. The focus of much current wrought magnesium alloy development is on alleviating these ductility and texture issues through the use of rare earth (RE) alloying element additions [69,70,72,111]. RE element additions to magnesium have been reported to increase the relative activity of other slip modes, i.e. non-basal [71,110,112,113,168], as well as weaken the basal deformation textures and promote one that is more randomized [3,69,70,72,74,111,169]. Such effects are pronounced, even when RE elements are added at low (microalloying) levels, with particular potency as a texture modifier demonstrated by Ce [69,70].

Implementing RE elements as microalloying additions to a base Mg alloy system, such as Mg-Al-Zn [107,170] or Mg-Zn [73,118] offers opportunities to improve alloy strength as well as ductility. In particular, the Mg-Zn system shows potential for the development of high-strength wrought magnesium alloys, as it exhibits significant strength enhancements from grain size refinement [171], solid solution strengthening [172], and precipitation hardening [18,19,42]. It is also notable that grain size refinement and precipitation hardening have been reported to be enhanced in Mg-Zn alloys by the additions of microalloying elements to the base binary systems [21,43,51] (see chapter 6).

The Mg-Zn-Ce system has been the subject of a number of recent studies, as alloys of this system can exhibit improvements in ductility over Mg-Zn [118] and in strength (due to grain size and solute strengthening) compared to binary Mg-Ce [66,73]. Improvements in texture have been reported for these alloys with both microalloying [66,73,105,117,118] and alloying [108,119] levels of Ce. However, for higher, alloying levels of Ce, these improvements in texture have not always corresponded to improvements in ductility due to the formation of secondary phase particles containing Ce [108].

Among elements other than RE, Ca microalloying additions have demonstrated evidence for texture improvement when added to Mg [59], AZ31 [170] and Mg-Zn based [121,173,174] alloys, although their effect on ductility has so far shown mixed results. However, additions of Ca to Mg-Zn are also reported to effectively refine grain size [121,173], and produce a significant precipitation hardening response (added in both low and high levels relative to Zn) [41,53,149,156,175], both of which have the potential to greatly improve alloy strength.

The Mg-Zn based alloys with Ce-Ca microalloying additions studied in this work were designed to yield improvements in texture and ductility with minimized amount of Ce, as well as high strengthening capability due to precipitation hardening. Furthermore, as these alloys are also designed to provide enhanced strengthening, the Zn content is studied at two different levels. The investigation into the effects of Ce-Ca microalloying additions on the precipitation hardening response of these alloys has been covered in chapters 6 and 7. In this chapter, the effects of this double microalloying of the Mg-Zn system on the microstructure and texture characteristics of the hot rolled and annealed sheet samples, and the effect of these characteristics on alloy ductility are presented.

8.2 Experimental Methodology

A list of the alloys examined in this chapter is presented in Table 8-1, as well as the testing methods used for each alloy. Although the examination is mainly focused on the Mg-Zn-Ce-Ca alloys (ZEX200 and ZEX400), tests on the binary alloys or alloys with the single microalloying additions of Ce are conducted for the purposes of comparison. Preparation of the alloys used in this work is described in section 3.1. All alloys are homogenized, rolled, and annealed according to the method outlined in section 3.2. All analysis of the annealed alloys, including optical microscopy, grain size measurement, SEM, TEM, EBSD, neutron diffraction, tensile testing, and thermodynamic calculation is performed according to the procedures outlined in chapter 3.

Table 8-1: List of experimental alloys investigated and test conducted related to chapter 8.

Alloy Designation	Optical Microscopy	SEM	TEM	EBSD	Neutron Diffraction	Tensile Testing
Z2	x	x	-	x	x	x
ZE20	x	x	x	x	x	x
ZEX200	x	x	x	x	x	x
Z4	x	x	-	-	-	x
ZE40	x	x	x	x	x	x
ZEX400	x	x	x	x	x	x

8.3 Results

8.3.1 Microstructure

Optical micrographs of the alloy microstructures, taken from the rolling plane, are shown in Figure 8-1. For all alloys following rolling and annealing, the grain size is relatively uniform. The grains themselves also appear equiaxed. Observations of specimen surfaces prepared along the rolling plane showed no distinct grain elongation with regard to the rolling, or transverse directions. Examination of the specimens prepared in the normal-transverse plane further showed no difference in the average grain diameter along the sheet normal direction.

Results of the grain size measurements are given in Figure 8-2. It is found that the largest grain sizes are for the binary alloys, and all the microalloying additions used in these alloys appear to produce a grain-refining effect. In particular, the alloys with the Ce-Ca double microalloying additions have the finest grain sizes. The ZEX200 alloy exhibits a slightly smaller average grain size than the ZEX400 alloy, although a higher amount of variability is also observed for the ZEX200 samples. Note that the twins present in the optical micrographs in Figure 8-2 are artefacts induced by mechanical polishing, as evident by the lack of twins found be EBSD in Figure 8-5.

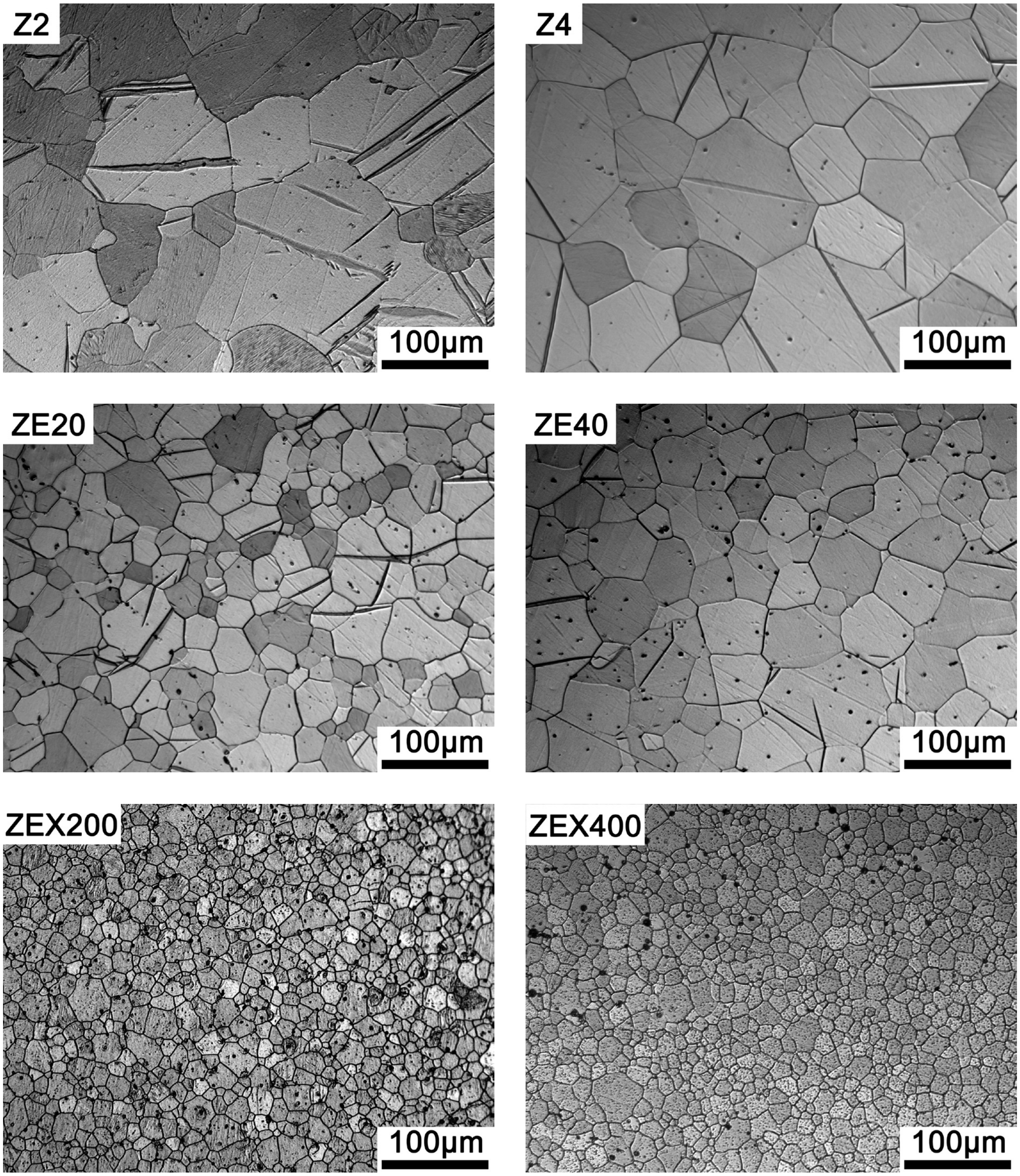

Figure 8-1: Optical micrographs of experimental alloys in the rolling plane.

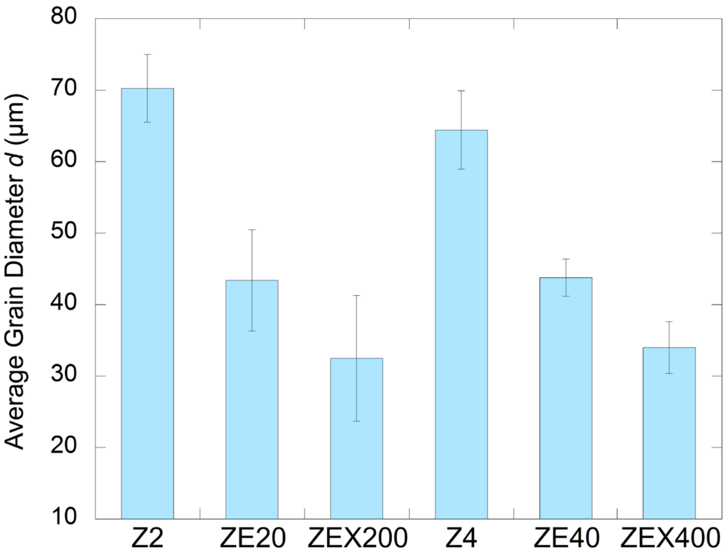

Figure 8-2: Average grain diameters for experimental alloys, taken from measurements in the rolling plane.

From SEM analysis, no observable secondary phase particles are found in the binary alloys, but all microalloyed samples exhibit secondary phases in the form of particles. SEM images of the microstructures for the microalloyed samples are shown in Figure 8-3. EDS measurements (spectra shown for typical particles in Figure 8-3) are used to identify the component elements present in the secondary phase particles. In all the microalloyed samples, particles are identified that are enriched in Ce and/or Ce+Zn. For the Ca-containing ZEX200 and ZEX400 alloys, particles are also found which contain Ca+Zn. In all cases when measuring the matrix concentrations, the levels of microalloying elements are too low to be detected by EDS. Area fraction analysis conducted on the SEM images for the secondary phases shows that the ZE20 and ZE40 alloys exhibit the lowest secondary phase fractions, followed closely by ZEX200. In these alloys, the average particle diameter observed by SEM appears to be approximately 1.0-1.5 µm. The ZEX400 alloy is observed to have a much higher fraction of secondary phase

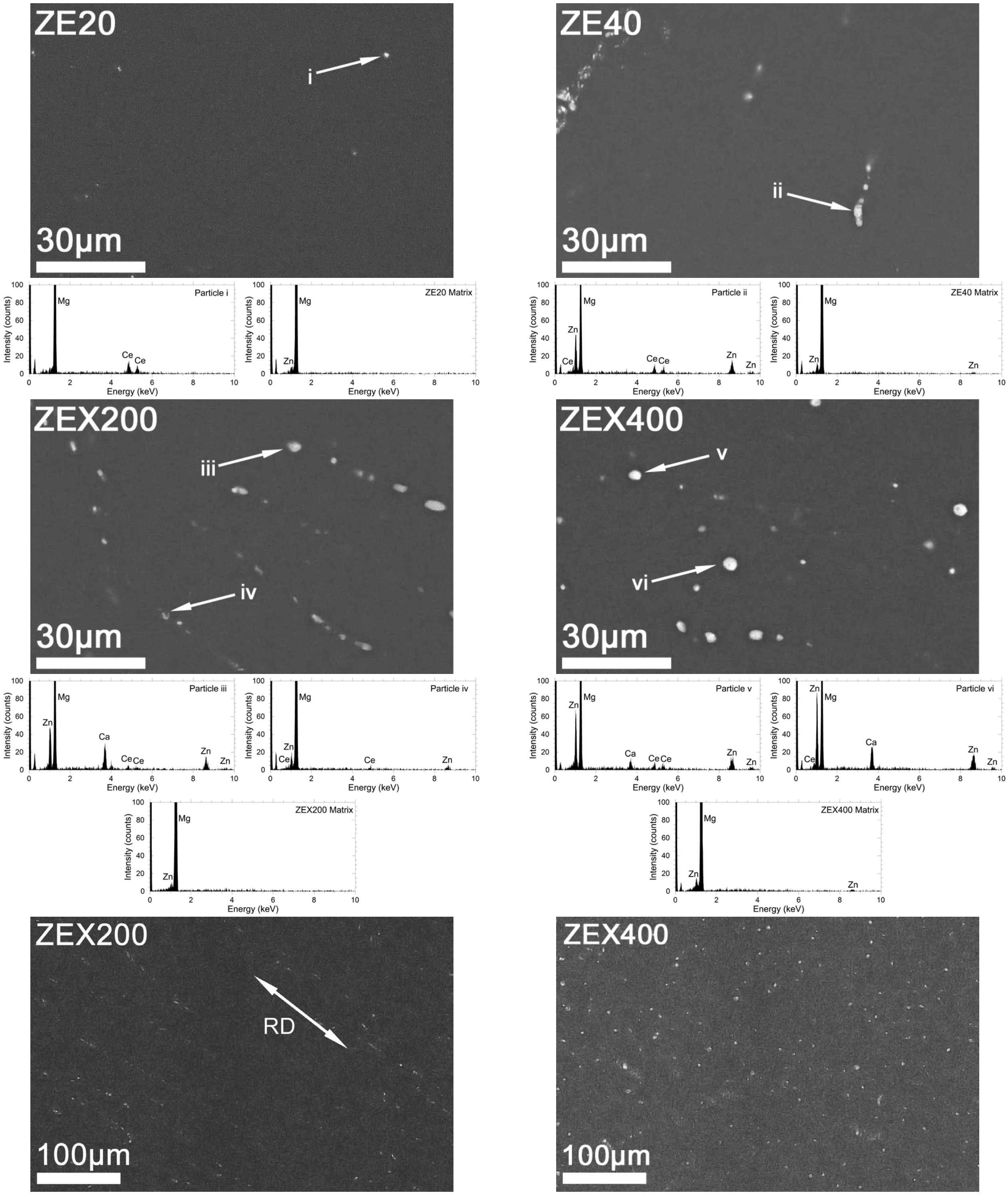

Figure 8-3: SEM backscatter images showing secondary phases for ZE20, ZE40, ZEX200, and ZEX400 alloys, and corresponding EDS spectra for select secondary phase particles, as well as the matrix phase. Low-magnification images show particle distributions in ZEX200, ZEX400. View is normal to the sheet plane of the rolled material.

particles, and a slightly higher particle diameter of approximately 1.5-2.0 µm. All the secondary phases appear circular or slightly elongated in the SEM imaging, and are therefore assumed to be roughly spherical or ellipsoidal. In general, the particle distribution is found to be uniform, but in some cases the secondary phase particles are found aligned in bands along the rolling direction. This is observed in all the microalloyed samples, but is most significant for the ZEX200 alloy. The alignment of particles along the rolling direction in the ZEX200 alloy is shown in Figure 8-3.

TEM investigations revealed further details about the secondary phases present in the alloys, and their distributions. Secondary phases observed in the Mg-Zn-Ce alloys are generally irregular in shape, with diameters ranging from 300-500 nm. They are often found accumulated in the form of colonies. These micron-sized particle colonies are found within the grains, and are occasionally dispersed throughout the alloy. A typical TEM image of such a particle colony is presented in Figure 8-4b for the ZE20 alloy. EDS results, also shown in Figure 8-4, indicate that the particles are enriched in Ce. These particle colonies are therefore consistent with the SEM/EDS observations (Figure 8-3).

TEM analysis of the alloys with double microalloying additions of Ce-Ca however reveals other, finer particles than just those detected by SEM. Overall, for the ZEX200 and ZEX400 alloys secondary phases are identified as generally present in three general size categories: 1) large particles (also seen by SEM observation), 2) medium-sized particles, and 3) fine particles. These medium-sized particles and fine particles are not notably observed for the Mg-Zn-Ce alloys. The particles and their distributions can be seen for the ZEX200 alloy in Figure 8-4a,c. The large particles are observed to be approximately 1.0-2.0 µm in size, and are most

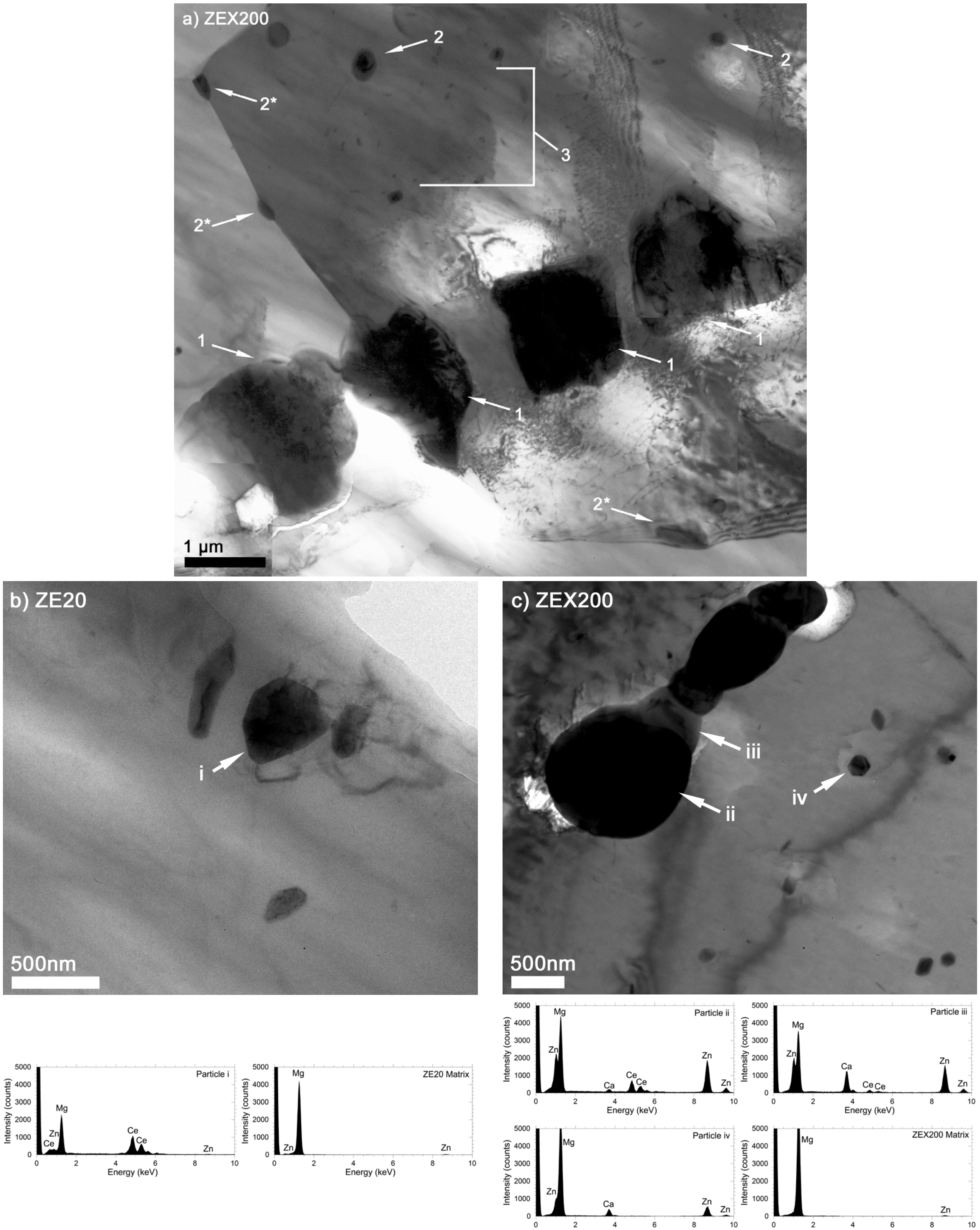

Figure 8-4: Bright field TEM micrographs for a) ZEX200 alloy showing: (1) large particles, (2) medium-sized particles (2*) medium-sized particles at grain boundaries, (3) fine particles, b) ZE20 alloy, c) ZEX200 alloy. EDS spectra are also presented which correspond to the precipitates and matrices shown in b) and c).

often found in the grain interiors, and only occasionally on grain boundaries or triple points. EDS measurements of these particles during TEM analysis (Figure 8-4c) correspond to the SEM/EDS data, indicating a relatively high concentration of Ce, with some particles/areas showing Ca enrichment. Comparing the composition information obtained by EDS with the particle morphologies shows that the regions of high Ce content are relatively spherical (e.g. particle ii in Figure 8-4c), with the areas of Ca-enrichment (particle iii in Figure 8-4c) found in between the Ce-rich particles. This particle characteristic suggests that the Ca-rich areas may have formed at a later time, with their growth assisted by the presence of the pre-existing Ce particles. The number of these large particles is found to be relatively higher in the ZEX400 alloy. The medium-sized particles are observed to have an irregular shape, with an approximate size of 150-500 nm. While the distribution of these medium-sized particles appears uniform, many are found to be located at grain boundaries and triple points, as seen for the ZEX200 alloy in Figure 8-4a. The numbers of these medium-sized particles are also slightly higher in the ZEX200 alloy. EDS analysis of these medium-sized particles did not detect significant levels of Ce, but did indicate Ca-Zn enrichment (Figure 8-4c). The fine particles are also irregularly-shaped, and appear evenly distributed within the grain interiors, as shown in Figure 8-4a,c. The sizes of these fine particles varies between the two Ce-Ca alloys, being approximately 40-100 nm in the ZEX200 alloy and 20-40 nm in the ZEX400 alloy. These particles were also observed in higher numbers for the ZEX400 alloy than the ZEX200 alloy.

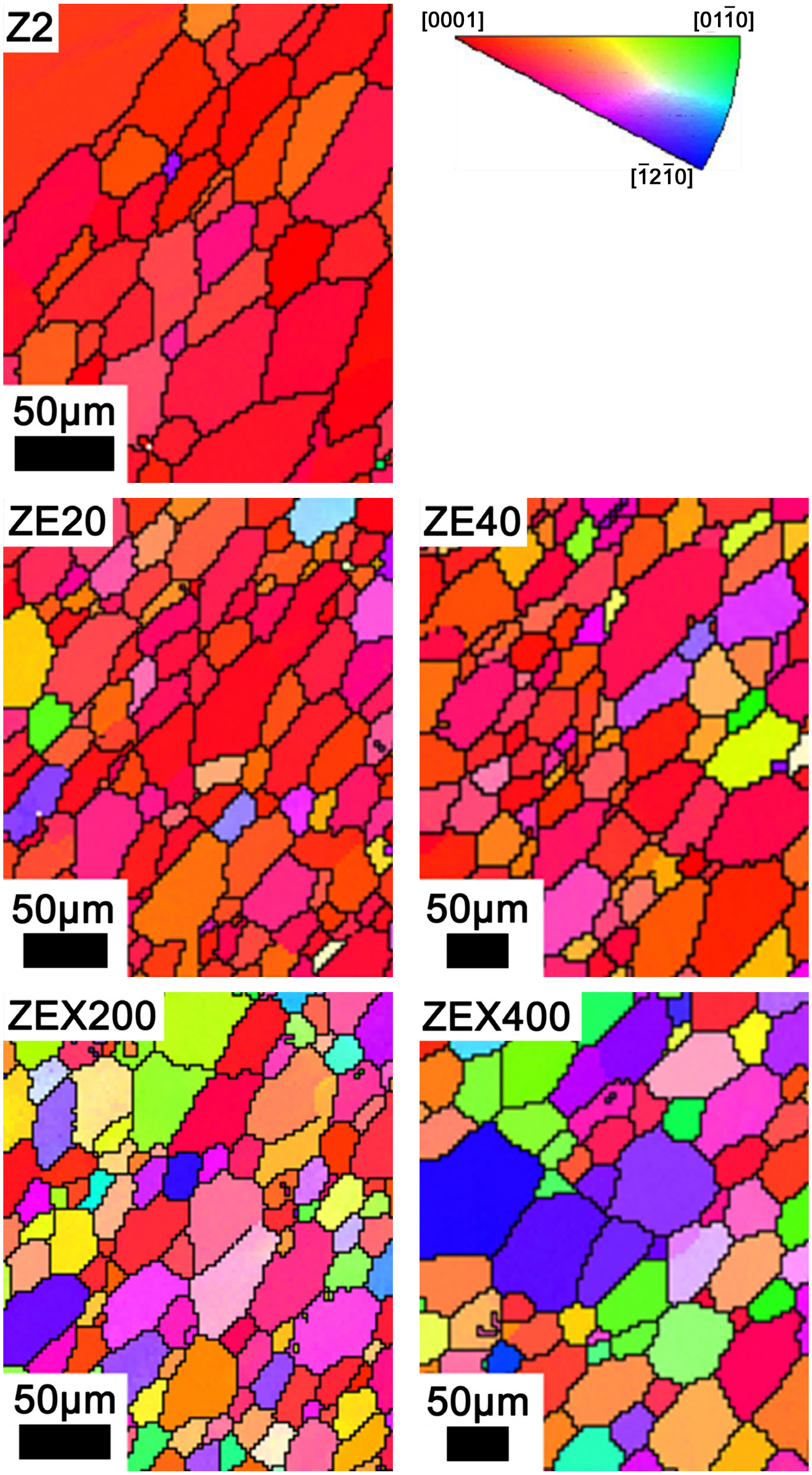

Figure 8-5: Inverse pole figure maps of Z2, ZE20, ZEX200, ZE40, ZEX400 along the rolling plane, measured by EBSD. Analysis performed by G. Nayyeri.

The results of alloy texture measurements obtained by EBSD are shown in the inverse pole figure maps in Figure 8-5 for the microalloyed samples, with the data for Z2 also presented for comparison. Note that while the grain sizes for Z2 and ZEX400 appear to deviate from the calculated averages from optical microscopy measurements in Figure 8-2, this may be due to the small area sampled by EBSD not being representative of the bulk. Additionally, a plot of the basal pole intensity in the direction normal to the rolling plane is given for comparison in Figure 8-6. The binary alloy Z2 is observed to exhibit a strong basal texture, typical of standard Mg-based alloys. However, the results for the microalloyed samples indicate that the microalloying additions have affected the texture compared to binary Mg-Zn. The alloys with just Ce additions (ZE20, ZE40) are observed to have a moderately altered texture. For these alloys, the intensity of the basal texture is lower than the binary alloy, but the microalloying elements have not produced a significantly randomized texture. The alloys with Ce-Ca additions however exhibit a further reduction in basal texture intensity and a much more randomized texture in general.

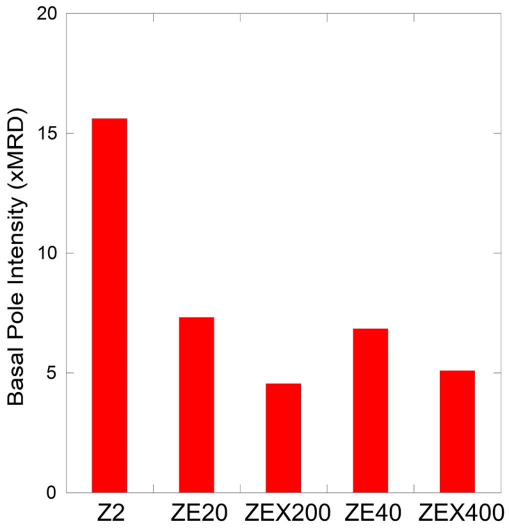

Figure 8-6: Basal pole intensities in the normal direction, as measured by EBSD. Analysis performed by G. Nayyeri.

To evaluate the bulk alloy textures following hot rolling and annealing more closely, and using sample sizes larger than for EBSD, neutron diffraction measurements are performed. The pole figures produced by these measurements are shown in Figure 8-7 for the microalloyed samples, and for the binary Z2 alloy. From these pole figures, the binary alloy can again be seen to show a strong basal texture, i.e. the basal poles are oriented strongly along the normal direction (Figure 8-7a). It is noted that there is a slight spread in the basal pole distribution along the rolling direction observed in this alloy. From the prismatic pole distribution for the binary alloy (Figure 8-7b) there appears to be no preferred orientation for the prismatic poles, as they are spread relatively uniformly, parallel to the sheet plane. The microalloying additions of just Ce, again exhibit a slight reduction in the basal pole intensity, as seen in Figure 8-7c and g. However, the texture remains predominantly basal, and is not largely altered from that of the binary alloy. Similarly, the prismatic poles are still distributed close to parallel with the sheet plane in the ZE20 and ZE40 alloys (Figure 8-7d and h). The significant texture modification observed for the double microalloying additions of Ce-Ca in the EBSD results is again seen in the neutron diffraction pole figures. It can be seen from the basal pole figures for ZEX200 and ZEX400 alloys (Figure 8-7e and i), that the basal pole distributions begin to split along the transverse directions. Consequently, the prismatic pole distributions (Figure 8-7f and j) are weakened along the transverse-normal plane.

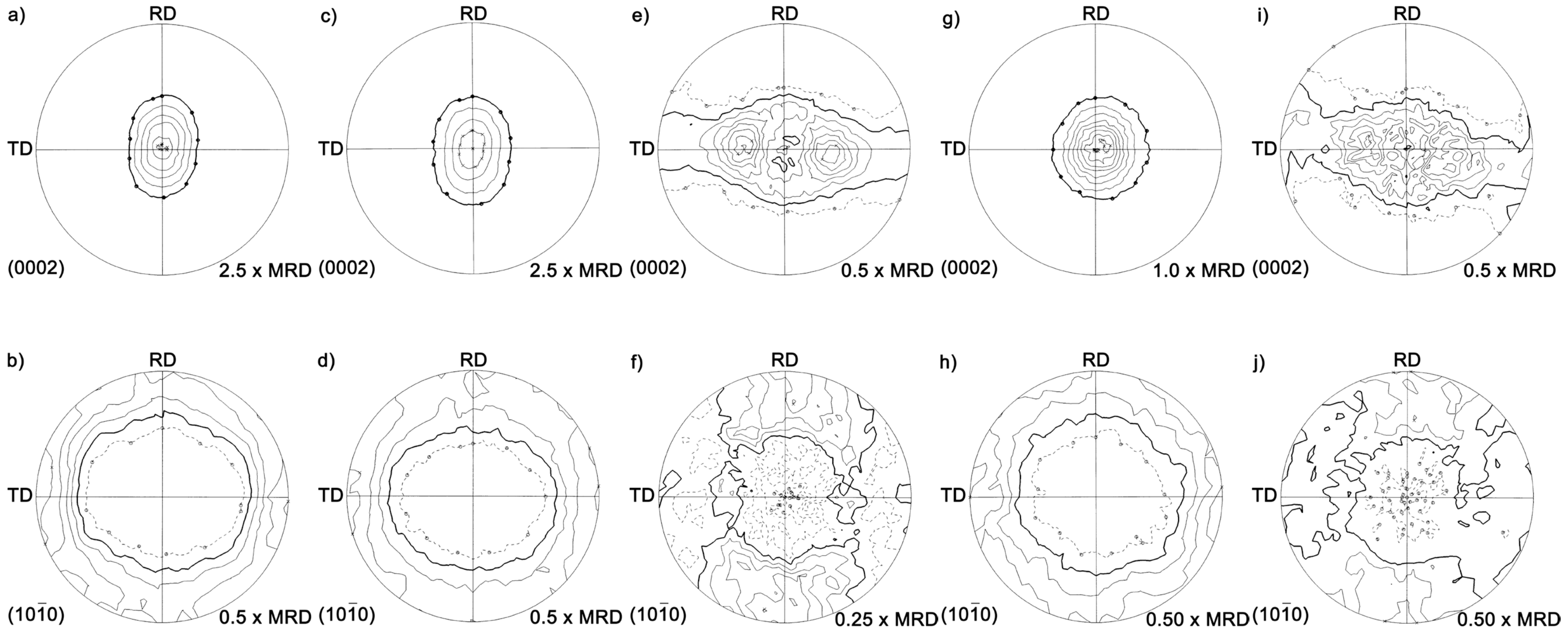

Figure 8-7: Pole figures obtained by neutron diffraction measurement for rolled and annealed a,b) Z2, c,d) ZE20, e,f) ZEX200, g,h) ZE40, and i,j) ZEX400 for a,c,e,g,i) basal, and b,d,f,h,j) prismatic poles. Contour lines represent multiples of a random distribution (MRD), as indicated for each pole figure. Bold contour lines are equal to 1 MRD. The rolling direction (RD) and transverse direction (TD) are labelled on the pole figures. Neutron diffraction measurements performed by S.Y. Lee and M. Gharghouri.

8.3.2 Mechanical Properties

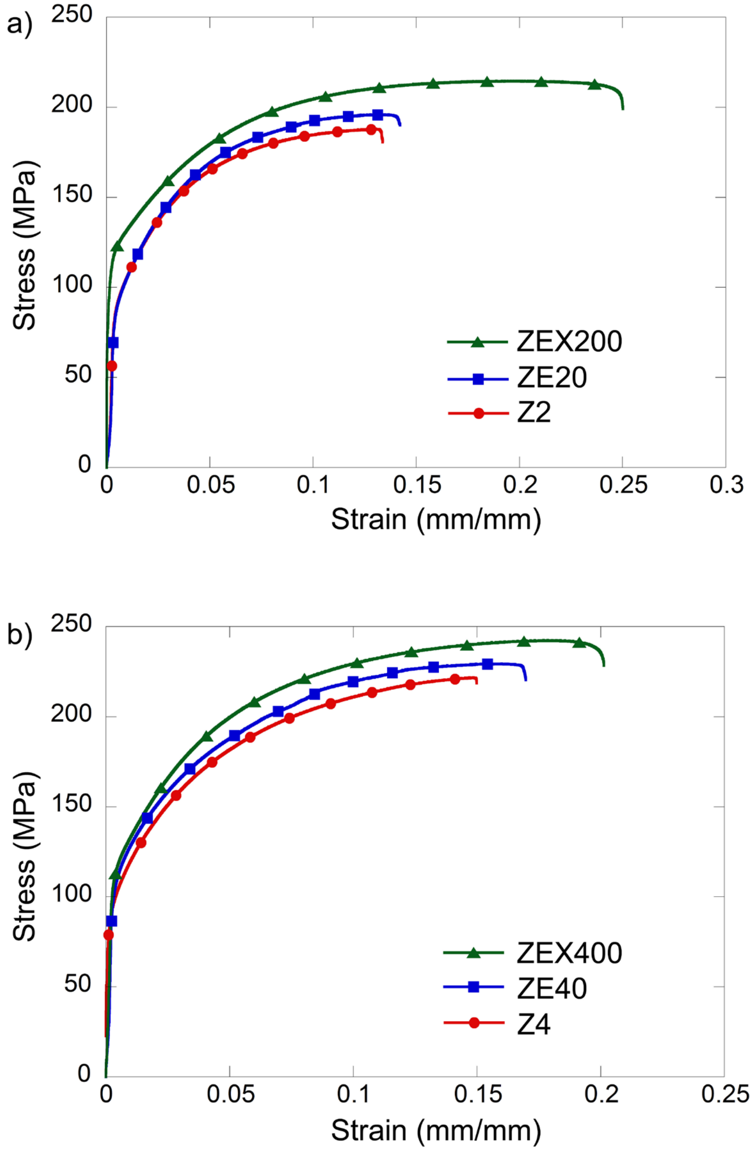

Figure 8-8: Typical engineering stress-strain curves obtained by tensile testing for a) 2 wt% Zn based alloys, b) 4 wt% Zn based alloys.

Data on the mechanical properties of the experimental alloys are obtained by tensile testing. Typical stress-strain curves of the alloys are shown in Figure 8-8, with full results given in Table 8-2. These results show that the alloys all deform plastically while strain-hardening to their ultimate tensile stress (UTS). For the Ce-Ca microalloyed samples, there is a very short period of non-uniform deformation followed quickly by fracture, whereas the UTS and fracture coincide for the Mg-Zn and Mg-Zn-Ce alloys. In general, the UTS is observed to increase with alloying/microalloying content. All alloys with 4 wt% Zn show higher UTS values than the 2 wt% Zn alloys, and the alloys with Ce-Ca microalloying additions exhibit higher UTS values than any other alloy variant of equivalent Zn concentration. The yield stress is found to be lowest for the binary alloys, and generally increase with microalloying additions. The alloys with the Ce-Ca double microalloying additions (ZEX200, ZEX400) exhibit the highest yield stress values among the experimental alloys studied in this work. Increasing Zn content also appears overall to increase the yield stress, but generally this effect is small, not highly significant given the measured variability.

Table 8-2: Tensile properties of experimental alloys obtained from tensile test results.

Alloy	Yield Stress (MPa)	UTS (MPa)	Elongation (%)
Z2	93 ±8	189 ±9	13.8 ±0.8
ZE20	96 ±17	187 ±10	14.4 ±5.4
ZEX200	131 ±12	222 ±7	23.9 ±0.3
Z4	100 ±1	221 ±1	14.5 ±0.0
ZE40	109 ±3	234 ±4	17.3 ±0.9
ZEX400	119 ±2	240 ±2	18.3 ±1.3

The ductility of the binary alloys is observed to be fairly low (<15% elongation). However, the microalloying additions are observed to positively influence ductility. Microalloying additions of Ce alone appear to result in a slight ductility improvement over binary Mg-Zn, as seen for the ZE40 alloy. However, the high variability of the ductility results for the ZE20 alloy makes it hard to assess the significance of any improvement for that alloy. The double microalloying addition of Ce-Ca produces an increase in elongation of approximately 1% for the ZEX400 alloy over the ZE40 (i.e. single addition of Ce) alloy. However, the elongation of the ZEX200 alloy is, at approximately 24%, significantly higher than any binary or other microalloyed alloys tested in this work.

8.4 Discussion

Alloying and microalloying elements have the potential to positively alter the microstructural characteristics of base alloys for tailored or optimal properties. The various experimental alloys studied in this work are seen to exhibit significantly different microstructures, and resultant tensile properties. As the processing and analysis parameters used for all alloys are identical, the observed changes in microstructure and properties between alloys can be attributed to alloy chemistry, i.e. differences in both the levels of Zn content (2, 4 wt%) and the microalloying variants (binary, Ce addition, Ce-Ca double addition). From the results on grain size refinement, texture modification, and tensile properties, it can be seen that the largest improvements over the binary alloys are achieved in every case by the Ce-Ca microalloying additions, compared to the alloys with just the single Ce microalloying additions. As the alloying/microalloying elements are able to affect the alloy microstructures and properties through a) solutes in the HCP-Mg solid solution, and b) particles dispersed in the matrix, the improved behaviour of the alloys with Ce-Ca additions can be understood to originate from either or both of these factors. The SEM and TEM observations of the microstructures (shown in Figure 8-3 and Figure 8-4 respectively) indicate that the highest secondary phase fractions are found in the ZEX200 and ZEX400 alloys. To assist in gaining an understanding of the solute levels in the alloys and determining the source of the observed differences in secondary phases, thermodynamic calculations are performed using FactSage 6.3 and the VLGM database [127].

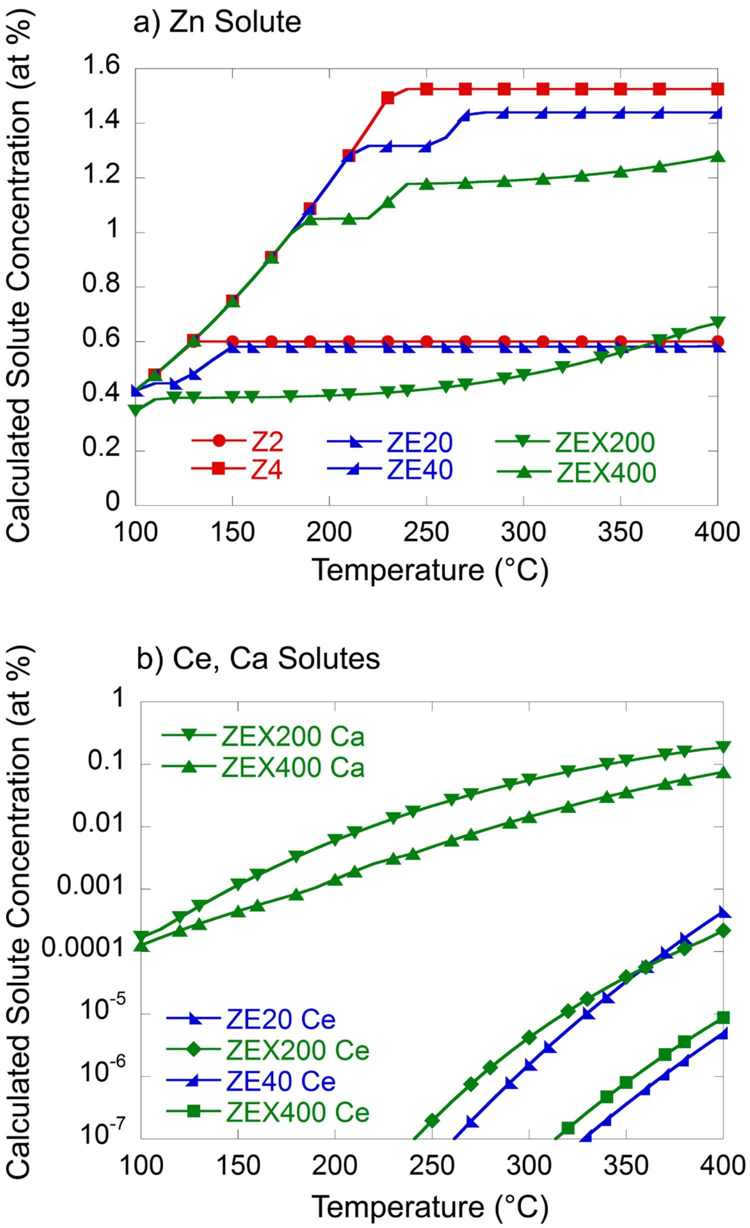

Figure 8-9: Equilibrium solute element concentration profiles for the experimental alloys from 400°C to 100°C for a) Zn, b) Ce and Ca in HCP-Mg, calculated using Factsage [127]. Note the logarithmic scale for b).

The calculated solute contents in the alloys as a function of temperature are presented in Figure 8-9. The solute contents are shown for temperatures below the annealing temperature of 400°C in order to assess how the solid solubility changes in the alloys with any cooling they may undergo during the rolling operation. The calculated equilibrium secondary phase fractions are also calculated over the same temperature range, and are shown in Figure 8-10. These equilibrium phases are predicted to be the $Mg_6Ca_2Zn_3$ phase, as well as the Mg_3Zn_5Ce and $Mg_7Zn_{12}Ce$ phases (the latter two phases collectively treated in this work as an MgZnCe-type phase), which are stable at or near the annealing temperature of 400°C, and also the $Mg_{12}Zn_{13}$ phase, which becomes stable at low temperatures.

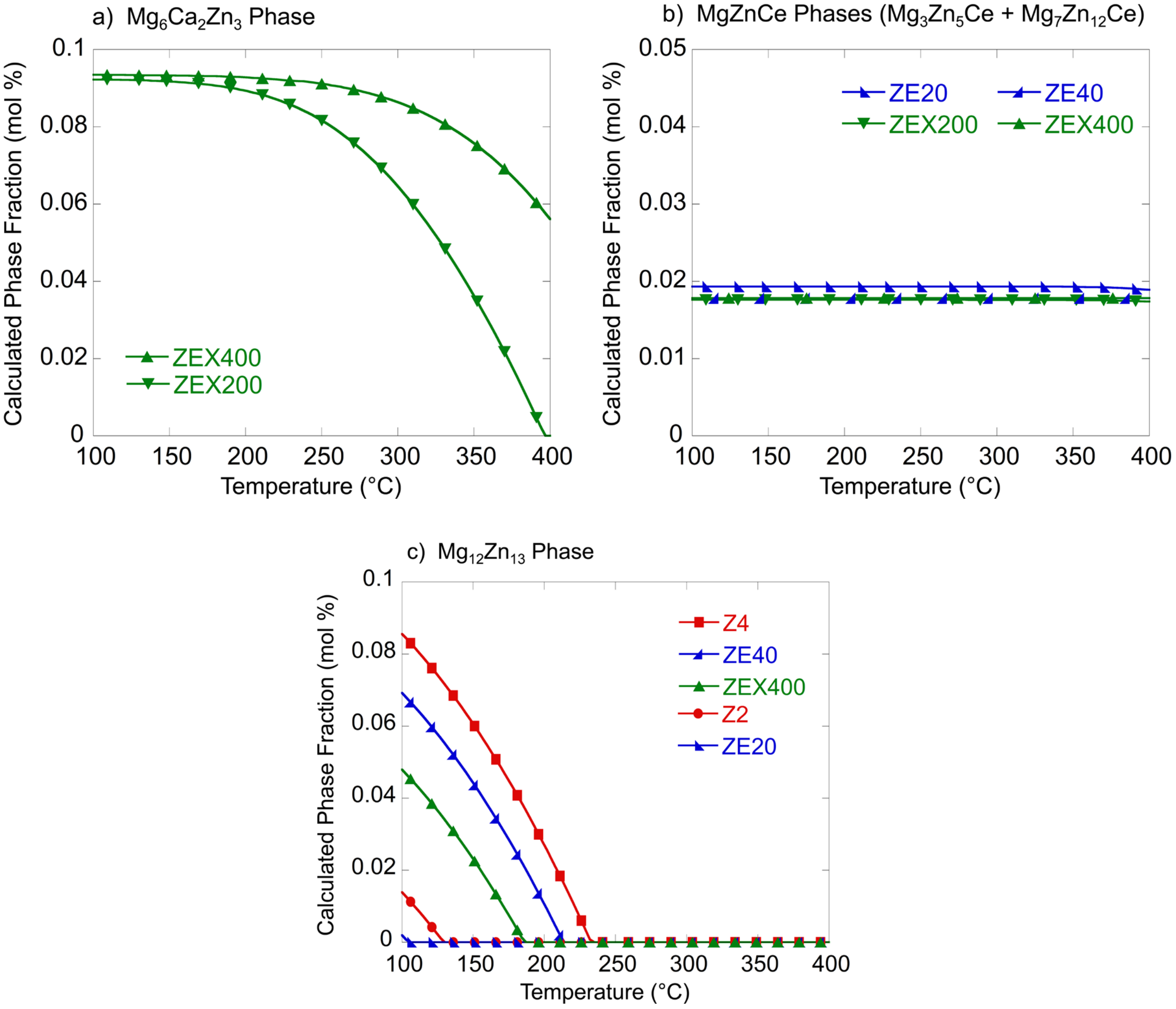

a) $Mg_6Ca_2Zn_3$ Phase

b) MgZnCe Phases (Mg_3Zn_5Ce + $Mg_7Zn_{12}Ce$)

c) $Mg_{12}Zn_{13}$ Phase

Figure 8-10: Equilibrium secondary phase profiles for experimental alloys from 400°C to 100°C, calculated using Factsage [127]. The plots are generated for the equilibrium phases of a) $Mg_6Ca_2Zn_3$, b) MgZnCe-type phases, c) $Mg_{12}Zn_{13}$.

In comparing the predicted solute and secondary phase fractions for the experimental alloys, it can be seen that the predicted amount of Zn content in these experimental alloys does not correlate to the observations of grain size, texture, or ductility. This indicates that Zn content is not able to significantly influence these properties on its own, and does so only by affecting the relative solubilities of the microalloying elements, and the amount of secondary phase produced when combined with those elements. When focusing on the effects of the microalloying elements however, it is seen that both the amount of total microalloying solute and the overall secondary phase fraction at/near the annealing temperature are highest for the alloys with the Ce-Ca double microalloying additions. For the solutes, the microalloying additions of Ca lead to concentrations of that element that are orders of magnitude higher than those for Ce, due to the higher solubility of Ca over the temperature range studied. The higher secondary phase fractions observed in the Ce-Ca containing alloys can also be attributed to the Ca element additions. This can be seen from Figure 8-10b, which shows the differences in the amount of MgZnCe-type phases between the alloys to be relatively small. Furthermore, comparison of Figure 8-10a and b also shows that the levels of MgZnCe-type phases are relatively low compared to those of the $Mg_6Ca_2Zn_3$ phase for temperatures near the annealing temperature. The improved microstructure of the alloys with Ce-Ca microalloying additions can therefore be attributed to having both higher microalloying solute content and secondary phase fractions in those alloys, and in particular to the significant contribution of Ca to both of those quantities.

Grain refinement may be promoted through solute drag effects. It is notable that comparison of the predicted solute content (Figure 8-9), with the alloy grain size (Figure 8-2) shows a much stronger correlation with the microalloying element solutes than the Zn solute, despite the latter being present in much higher levels. The efficacy of these microalloying elements in promoting solute drag compared to Zn may be related to their relative atomic size. The metallic radii of Ce (1.818 Å) and Ca (1.970 Å) show that both of these solutes are over-sized compared to Mg (1.598 Å), and differ by a larger amount from Mg than the undersized Zn (1.379 Å) [151]. By exerting a larger solute drag compared to the main Zn alloy element, the microalloying additions could enhance grain size refinement in each of the microalloyed samples.

Grain refinement can also be produced by secondary phase particles through their potential role in the recrystallization behaviour of the alloy. One method by which secondary phases can promote grain refinement is by particle stimulated nucleation (PSN) [67]. As PSN is generally associated with the presence of large particles [67] such effect in the current alloys would be expected to originate from the large particles found in all the microalloyed samples. In that case, given that all the alloys were deformed equally, the ZEX400 alloy would be expected as being most affected by PSN, as the highest number of large particles were found in that alloy (i.e. the SEM-resolvable particles shown in Figure 8-3). For grain refinement by PSN, the ZEX400 alloy would therefore be expected to exhibit the finest grain size. However, the results suggest that ZEX400 and ZEX200 alloys have similar grain sizes. Additionally, grains formed by the PSN mechanism would normally be expected to exhibit a random orientation [109], and not have the basal poles aligned parallel to the normal direction (for Ce microalloying) or normal-transverse plane (for Ce-Ca microalloying) as observed for these alloys. Both of these observations suggest that PSN does not play a significant role in grain refinement for these alloys. This finding is consistent with the recent report of Robson et al. [109], who studied the impact of PSN on recrystallization of an Mg-Mn alloy with micron-sized particles and found

PSN grains to make up only a small fraction of the total recrystallized grains following annealing. However, determining the precise role (if any) of PSN in the current case requires further investigation.

The enhanced grain refinement in the Ce-Ca alloys may also be positively-influenced by the secondary phases through Zener drag effects during recrystallization [67]. For Zener drag, this effect is reported to scale with the volume fraction of particles, but is also inversely-proportional particle size (radius) [67]. This is consistent with observations of the secondary phases in the current alloys, as well as the calculated phase fractions. The largest particles and particle colonies in the alloys microalloyed with Ce-Ca and Ce do not appear to influence the grain boundary movement during recrystallization as most are found contained within large grains. Their size, i.e. radius, may therefore be too large to produce a significant Zener drag effect. On the other hand, the medium-sized particles in the ZEX200 and ZEX400 alloys, which are found in higher numbers than the large particles, are commonly observed at grain boundaries and triple points, with the boundaries bowing around them (as seen in Figure 8-4a). This appearance of the grain boundaries interacting with the medium-sized particles indicates that they successfully pin the grain boundaries during annealing. The fine particles, observed only for the ZEX200 and ZEX400 alloys (shown for ZEX200 in Figure 8-4a) may also aid in refining the alloy grain size as their radii are small and they are present in high numbers, provided that they exist prior to annealing or form concurrent with recrystallization. However, as the sequence of such diffusional processes has not been identified in this work, the role of the fine particles on grain refinement cannot currently be unambiguously determined.

As the highest impact on grain refinement due to secondary phases in the Ce-Ca containing alloys appears to be from the medium-sized particles, it is worth commenting on their origin.

The secondary phases that are present in the alloys at the beginning of rolling are assumed to be those phases that are present at equilibrium during the homogenizing heat treatment (24 h at 400°C). The amounts of these phases are calculated, and found for most alloys to be roughly proportional to the area fractions of the secondary phases in the annealed alloys, as measured by SEM imaging (comparison shown in Figure 8-11). This relation suggests that the calculated secondary phases at the homogenizing/annealing temperature primarily correspond to the large particles, as these were the only particles observable by SEM imaging. The relatively large size and coarse distribution of those particles is also consistent with their formation at the high temperature, and over the long time associated with the homogenization heat treatment. It therefore follows that the medium-sized particles form during the rolling and annealing operations, at temperatures between that of the annealing furnace (400°C) and that of the rolls (150-180°C). Based on the calculated results shown in Figure 8-10a, the medium-sized particles can be identified as the $Mg_6Ca_2Zn_3$ phase (or a metastable precursor) as it exhibits the largest increase in phase fraction over the temperature range in question. The $Mg_6Ca_2Zn_3$ phase is also consistent with the Ca-enrichment measured for the medium-sized particles by EDS (Figure 8-4c). This finding also suggests that a key parameter for refining the microstructures of these Mg-Zn based alloys by Ca addition may be that the Ca content and processing route allows for a significant secondary phase fraction to precipitate during rolling or subsequent cooling. This behaviour is contrasted by the Mg-Zn-Ce alloys, where the secondary phase fraction does not change significantly with reduction in temperature below 400°C, as seen in Figure 8-10b. As a result, the only secondary phases present in those alloys are large particles or particle colonies, which do not significantly refine the grains.

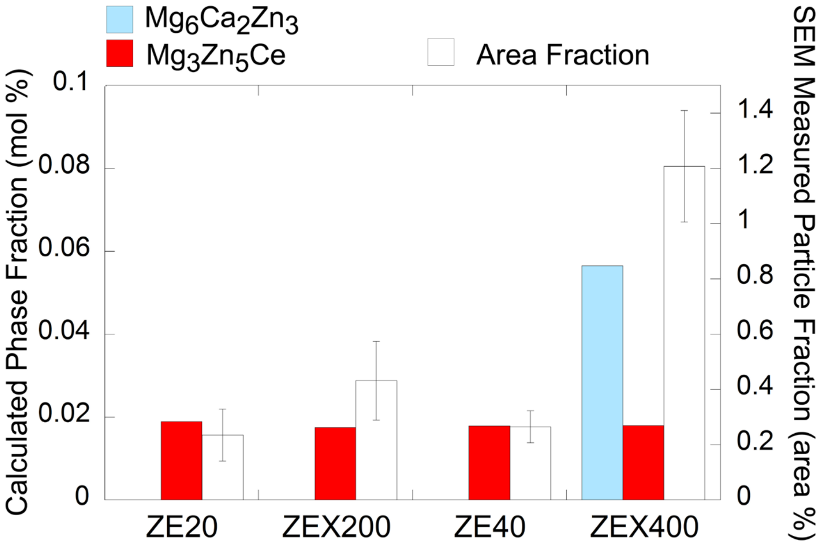

Figure 8-11: Calculated phase fractions at the homogenizing temperature of 400°C (mol%) and particle area fractions measured by SEM imaging of annealed alloys.

Since the most significant improvements in texture and ductility are observed for the double microalloying additions of Ce-Ca, the ZEX200 and ZEX400 alloys will be the focus of the remaining discussion. The exact origins of the texture weakening effect due to alloying/microalloying elements are still a subject of continued research, but have been reported to arise due to the influence of both solute content and secondary phase particles on slip, twinning, and recrystallization. For elements that can cause texture modification in Mg alloys, particularly rare earth elements, the change in texture has been explained in literature as partially a result of promoting non-basal slip modes, such as prismatic $\langle a \rangle$ slip, and pyramidal $\langle c + a \rangle$ slip [71,110,113]. In the current case, it is suggested that the spread of the basal poles towards the transverse directions is observed for the ZEX200 and ZEX400 alloys is due to the activation of prismatic $\langle a \rangle$ slip, as also reported for Mg-Zn-Ce alloys [66]. In studies of Mg-Y and Mg-Nd alloys, similar enhanced activation of prismatic $\langle a \rangle$ slip has been attributed to solute effects on both basal slip and cross-slip [71,110]. The Ce-Ca additions can also positively-influence activation of prismatic $\langle a \rangle$ slip as they are the most potent at refining grain size. Such an effect of refining grain size on reducing the CRSS for prismatic $\langle a \rangle$ slip, relative to basal slip, has been recently noted in a report by Stanford and Barnett [176]. In addition to effecting slip mode activity, the Ce-Ca solutes in the current alloys may also affect twinning. Activation of $\{10\bar{1}1\}\langle 10\bar{1}2 \rangle$ compression twins and $\{10\bar{1}1\}\{10\bar{1}2\}$ double twins have been identified as potentially important factors in reducing basal textures [112,113,119], and Ca solutes have been reported to potentially promote these twinning modes during rolling [174]. However, characterization of the exact twinning behaviour in the current alloys requires further investigation.

The recrystallization behaviour can also play a key role in producing the weakened textures observed for the ZEX200 and ZEX400 alloys. The aforementioned effects of both solutes and secondary phases on mobile grain boundaries may inhibit the growth of basal-oriented grains compared to non-basal-oriented grains, and stop the former of these from making up the majority in the alloy. Such a growth advantage for non-basal-oriented grains has been suggested as a major factor in texture weakening observed for Mg-Zn-Ce alloys [117]. It has also been recently suggested in reports by Hadorn et al. [71,110] that reducing grain boundary mobility, due to both solute and particle drag effects, may change the recrystallization behaviour discontinuous dynamic recrystallization, with new grains nucleating on grain boundaries, to one involving shear band nucleation or possibly continuous dynamic recrystallization. Additional study is necessary however to assess if such a change in recrystallization mode occurs in these alloys.

The enhancement in ductility observed from the Ce-Ca microalloying additions can be understood as resulting from improvement in grain size and texture, as well as possible effects on slip modes. The weakened textures of the microalloyed samples can positively affect ductility, as altering the distribution of the basal poles away from the sheet normal direction can increase the number of grains oriented for easy slip modes (i.e. basal slip) along the loading direction. Having more grains well-oriented for $\{10\bar{1}2\}\langle 10\bar{1}1\rangle$ extension twinning during tensile testing could also contribute to a ductility increase [111,169]. Furthermore, a ductility improvement can be expected if the activity of non-basal slip modes, such as prismatic $\langle a\rangle$ slip, is enhanced by the solute and grain size effects previously mentioned. In particular, the activation of non-basal slip near the grain boundaries, where compatibility stresses can arise due to the dominance of basal slip, may contribute to the observed ductility enhancement in the current alloys [62,177].

Further insight into the differences in ductility among the alloys can be gained by observations of the fracture surfaces, as shown in SEM images in Figure 8-12 for the Z2, ZEX200 and ZEX400 alloys. It is clear that while the binary Z2 alloy shows a fracture surface that is relatively smooth, the ZEX200 alloy has a rough, dimpled fracture surface. This is indicative of change in fracture from quasi-cleavage trans-granular fracture, typical of many common Mg-based alloys, to ductile fracture due to the Ce-Ca microalloying additions. This change in fracture behaviour also corresponds to changes in alloy ductility, as the Z2 exhibits the lowest elongation while ZEX200 shows the highest. It is also notable that micro-cracks, found throughout the fractured material surface for the Z2 alloy and suggestive of sub-surface damage prior to the onset of total material fracture, were observed only rarely in the ZEX200 alloy.

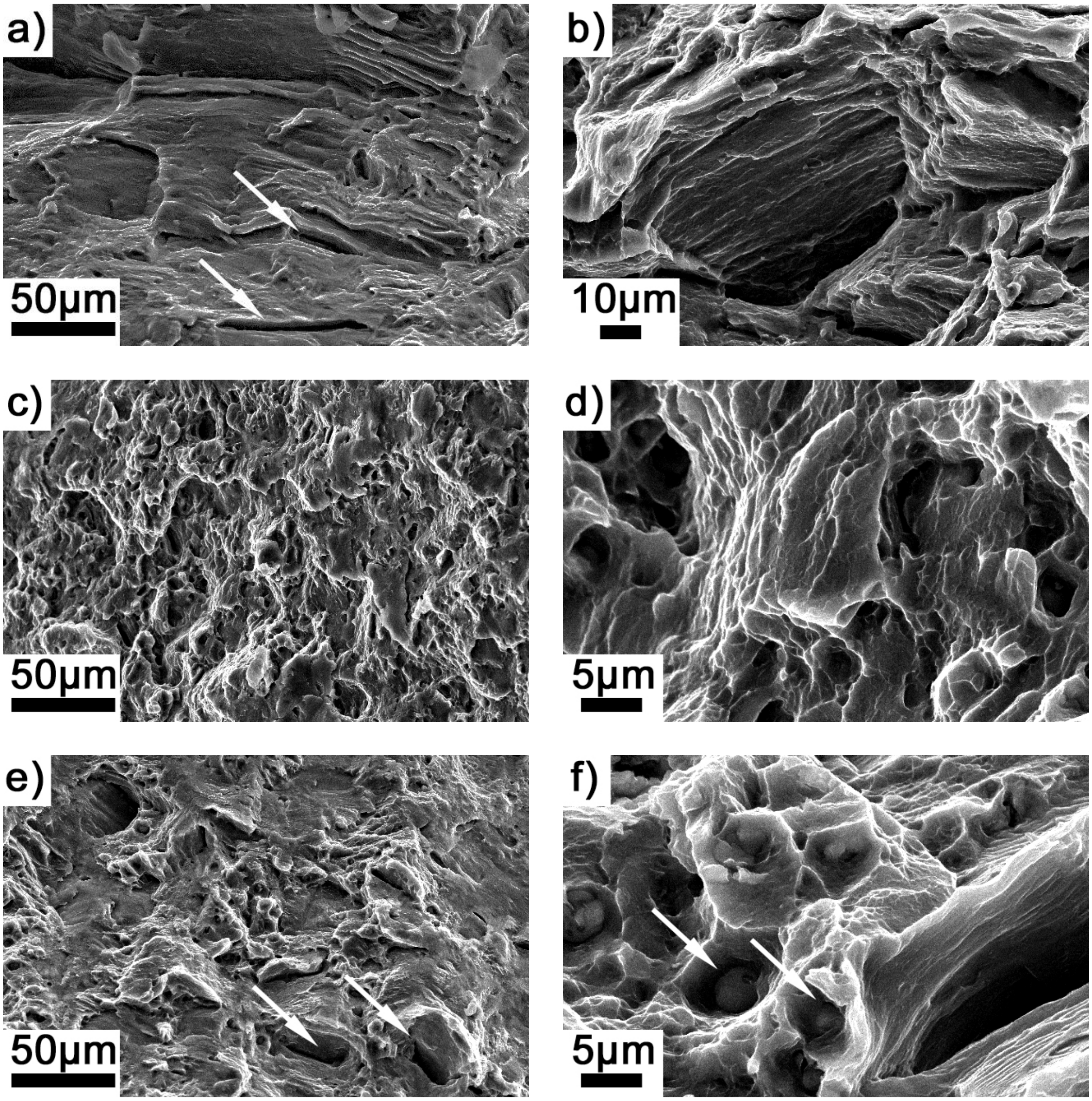

Figure 8-12: SEM secondary-electron micrographs showing the fracture surfaces of a,b) Z2, c,d) ZEX200, e,f) ZEX400 alloys following tensile testing. Micro-cracks in a) and e) are indicated by arrows. The arrows in f) show secondary phase particles at micro-void sites in ZEX400.

A comparison of the fracture surfaces for ZEX200 and ZEX400 also helps explain the observed differences in ductility between the two alloys. The ZEX400 alloy shows a higher level of micro-cracks in the material surface than the ZEX200 alloy. Additionally, secondary phase particles are found to lie at the root of dimples on the ZEX400 alloy fracture surface

(Figure 8-12f) which are again only occasionally observed in the case of the ZEX200 alloy. These particles are of similar scale and morphology to the large particles in that alloy (seen in Figure 8-3), which are attributed to the secondary phases stable at the homogenizing/annealing temperature. Due to the relatively large size of these particles, it is possible that strain incompatibilities between these particles and the matrix leads to the nucleation or growth of micro-voids at high strains, leading to specimen fracture. The higher presence of these secondary phase particles in the surface dimples of the ZEX400 alloy compared to the ZEX200 alloy is consistent with the observations of a higher number of large particles in ZEX400. This key difference between the two alloys explains the lower ductility exhibited by the ZEX400 alloy compared to the ZEX200 alloy, despite having a similar grain size and texture. Such a reduction in elongation caused by large secondary phase particles highlights the benefits of using Ca at microalloying levels for optimum texture and ductility, as higher levels of Ca content may produce greater amounts of large secondary phase particles. The potential for a high amount of Ca-containing secondary phase particles to promote fracture was also found in the work of Stanford [59] who found that when normalized for refined grain size, Ca microalloying additions to Mg and Mg-Mn alloys effectively reduced ductility.

From the results presented in this chapter, it is concluded that the ductility of the ZEX200 alloy is enhanced more than in the case of the ZEX400 alloy. However, the results from chapter 6 show that the precipitation hardening potential is greater for the ZEX400 alloy, due to the additional Zn solute [156]. A comparison of these two properties between the ZEX200 and ZEX400 alloys is presented in Table 8-3. Although both of these alloys possess advantages over conventional Mg and Mg-Zn alloys, the preference of either alloy will depend on the combined requirements of ductility and strengthening potential. Additionally, there exists the opportunity to further enhance the final properties of these Mg-Zn alloys with Ce-Ca microalloying additions by continued alloy design to adjust compositions within this system, as well as by process optimization.

Table 8-3: Comparison of ZEX200 and ZEX400 alloy ductility and precipitation hardening ability during 180°C ageing.

Alloy	Elongation (%)	Age-Hardening Response (ΔHVN)
ZEX200	23.9 ±0.3	8.8 ±1.9
ZEX400	18.3 ±1.3	24.8 ±1.5

8.5 Summary

The results presented in this work show that augmenting a low-level RE element addition (in this case Ce) with the non-RE microalloying element Ca, can yield improvements in mechanical properties and microstructure. The additional Ca refines the grain size and improves the texture of the alloys. These changes in microstructure are proposed to be achieved through both solute effects, and by producing a uniform dispersion of sub-micron sized particles. Combined SEM/EDS and thermodynamic analysis indicate that the formation of the particle dispersion occurs during the rolling/annealing process, and is due to the microalloying element Ca. Large particles enriched in Zn, as well as Ce and/or Ca, are also found in all microalloyed samples which form prior to rolling/annealing. However, the large size and coarse distributions of these particles limit their significance in affecting the microstructure. The enhanced microstructural characteristics of the alloys with Ce-Ca additions result in improvements in tensile properties over both binary Mg-Zn and Mg-Zn alloys with single microalloying additions of Ce. Comparing the Ce-Ca microalloyed samples of both high (4 wt%) and low (2 wt%) Zn content reveals a greater ductility for the low-Zn alloy. Analysis of the tensile specimen fracture surfaces indicates that this difference in ductility is due to a greater amount of the large secondary phase particles in the high-Zn alloy, which promote fracture. The results of this chapter demonstrate the potential of this alloy system for practical application, and highlight it as an excellent candidate for future alloy design and development efforts.

9 Conclusions, and Recommendations for Future Work

The following chapter summarizes the main conclusions of the reported research. Recommendations for future work are made based on these conclusions.

9.1 Conclusions

- The combination of Zn and Ca in magnesium alloys with high Ca content is shown to be beneficial for the age-hardening response, due to the formation of both large basal plates and fine basal precipitate phases. These latter precipitates are identified as GP zones, which evolve into fine basal plates with continued ageing.

- For the alloys with high Ca content, increasing the level of Zn from 1 wt% to 2 wt% did not increase the age-hardening response, as this was in excess of solid solubility. For all other Mg-Zn alloys studied in this work, particularly those with only microalloying additions, increasing the Zn content (i.e. from 2 wt% to 4 wt%) resulted in an increase in the age-hardening response.

- No significant benefit to the precipitation capabilities of Mg-Zn is found by the single addition of Ce in microalloying or alloying levels, with the presence of Ce in solution having a slightly negative effect. This negative effect on hardening is hypothesized to be due to preferential interactions between Ce solutes and vacancies, which hinder the nucleation of Mg-Zn phases and produces a lower number density of precipitates, and a greater fraction of precipitates formed with a non-uniform distribution on dislocations.

- It is shown that a high-temperature pre-ageing heat treatment conducted to precipitate Ce from solution is effective in retaining the maximum precipitation hardening capability of the selected Mg-Zn-Ce alloy.

- Double microalloying additions of Ce-Ca are found to be the most effective at enhancing the precipitation hardening response of Mg-Zn, due to a combination of refined distribution of β'_1 precipitate rods and the formation of fine basal plate precipitates. The increased precipitation hardening capabilities due to Ce-Ca additions are primarily attributed to the Ca element, with Ce having little effect.

- The fine basal precipitate phases are found to multi-layered GP zones, several atomic layers thick, which evolve from monolayer GP zones. The formation of the GP zones is attributed to differences in the respective sizes of the Ca (and possibly Ce) and Zn solute atoms, as well as the tendency of Ca and Zn to co-cluster. It is suggested that these precipitates represent a transition phase, which acts as a metastable precursor to the $Mg_6Ca_2Zn_3$ equilibrium phase.

- The β'_1 phase is observed to form after the fine basal plate precipitates, and contain only Mg and Zn, with no significant microalloying content. Refinement of the β'_1 phase distribution is suggested to be positively-influenced by the presence of the fine basal plate precipitates in the matrix. The combined hardening effects from the β'_1 phase and the fine basal plates produce the peak-aged condition in the ZEX400 alloy.

- The tendency of Ca solutes to homogeneously form clusters also inhibits the level of grain boundary segregation for that element, while a high level of Zn solute segregates to the grain boundaries. This difference in solute segregation behaviours for Ca and Zn leads to the formation of Zn-rich grain boundary precipitates, and a zone near the grain boundaries which is free of β'_1 and β'_2 precipitates, while the Ca-containing fine basal plate precipitates are uniformly-distributed throughout the grain boundary-grain regions. It is also noted that the precipitate-free zone for the β'_1 and β'_2 precipitates is significantly smaller than in the binary alloy, due to refinement in the distribution of those phases.

- Compared to both binary Mg-Zn alloys and alloys with Ce microalloying additions, alloys with Ce-Ca additions are observed to have the finest grain sizes in the rolled and annealed condition, with textures that are considerably weakened compared to the strong basal textures typical of rolled magnesium alloy sheet. These properties result in a significant increase in alloy ductility, as measured during tensile testing.

- Based on SEM and TEM observations, as well as thermodynamic calculations, the improved microstructural characteristics and ductility of the alloys containing Ce-Ca are attributed to (a) a high number of fine secondary phase particles, and (b) potential solute effects on both recrystallization and slip.

- Alloys with both high and low Zn content exhibit refined grain size, enhanced texture, and improved ductility due to the Ce-Ca additions. However, the ductility is notably higher for the low-Zn ZEX200 alloy than for the high-Zn ZEX400 alloy. Analysis of the fracture surfaces of the alloys highlights a possible role of large secondary phase particles in promoting fracture in the ZEX400 alloy. This finding also suggests limits on the ductility increases possible through the addition of Ce-Ca to Mg-Zn.

- Considering precipitation hardening capability, microstructure, and tensile properties, it is found that the combined microalloying additions of Ce-Ca are able to simultaneously produce significant improvements in properties. The Mg-Zn system with Ce-Ca microalloying additions is therefore recommended for development of a high-strength wrought magnesium alloy with enhanced microstructural and ductility characteristics.

9.2 Recommendations for Future Work

The following section introduces ideas for future work related to the current research, which are arrived at based on the results of this study.

Alloy Composition and Process Optimization

As the findings of the current in-depth study can be applied to understand the behaviour of Mg-Zn alloys with Ce-Ca microalloying additions, changes in Zn, Ce, and Ca composition, as well as ageing times and temperatures can be effectively optimized. It is recommended for such a study that the Ce content be kept at low levels, as it does not largely effect precipitation, while Zn and Ca solute content be optimized. It should be noted that adding Zn and Ca at levels such that a high volume fraction of secondary phase particles form during solutionizing should be avoided, as it may negatively impact ductility. Analysis of different ageing heat treatments may also produce an optimum balance between strengthening in the peak-aged condition, and the ageing time necessary to reach that condition. By optimizing these compositions and processing parameters for the Mg-Zn-Ce-Ca alloys, further improvements in both precipitation hardening capability and ductility may be achieved.

The Effect of Deformation prior to Ageing on ZEX400 Alloy Precipitation

Observations in the current work of Mg-Zn type precipitates forming at grain boundaries and aligned along dislocations suggests that nucleation of those phases occurs heterogeneously; therefore, their formation may be enhanced by an increased dislocation density. By deforming the solutionized alloy to increase the dislocation density prior to ageing, the distribution of the β'_1 phase may be refined, and its nucleation and growth rates increased. This effect has been reported in literature for binary Mg-Zn alloys, and may therefore also apply to ZEX400, as the β'_1 precipitate rods are a main strengthening phase in that alloy. It is also notable that a reduced ageing time for achieving peak hardening from β'_1 precipitation, will coincide more with the short ageing times for GP zone formation. Alternatively, ageing may be interrupted to perform the deformation before the formation of β'_1 , but after Ca-Zn clustering or GP zone nucleation has occurred. Producing a microstructure containing highly-refined distributions of both β'_1 precipitates and GP zones may maximize the precipitation hardening capabilities of the ZEX400 alloy, while reducing the overall ageing time required to reach the peak-aged condition.

Microalloying Mg-Zn-Ca with Different Rare Earth Elements

The current research has focused on the use of Ce as a RE element addition due to its potency as a texture modifier, which therefore allows it to be added in a very low level to the alloys. This strategy is effective at reducing the requirement for RE element addition; however, it is observed that the low solute content and supersaturation lead to minimal benefit from Ce on the precipitation hardening responses of the alloys. It is therefore proposed that RE elements with higher solubility in magnesium (such as Gd, Y, or Nd), which are also proven to modify texture, be studied as microalloying additions to the Mg-Zn-Ca system. By increased solute/supersaturation effects, these RE elements may be able to better enhance precipitation hardening. Furthermore, while it is expected that these RE elements may be required in higher levels than Ce in order to achieve a modified texture, Ca may again augment the texture weakening capabilities of the RE elements, to allow for minimal overall RE content. The potential of these Mg-Zn-Ca-RE systems to maintain the microstructure and ductility characteristics of the current Mg-Zn-Ce-Ca alloys, while further enhancing the precipitation hardening effect, makes them of high value for future research.

Deformation and Recrystallization Behaviour of Mg-Zn-Ce-Ca Alloys

The results in this report indicate that the combined microalloying additions of Ce-Ca significantly weaken the texture of Mg-Zn alloys. However, a comprehensive study on the deformation and recrystallization behaviour of the alloys could further elucidate the origins of this modified texture. In particular, analysis can be expanded to include not only the annealed condition, but the as-deformed condition as well. By examining the microstructures in these conditions, additional insight into the texture evolution and recrystallization mechanisms can be obtained. As suggested by the findings of the current study, the role of precipitation during the rolling/annealing process should be assessed. Increased understanding of the deformation and recrystallization behaviour in these alloys could facilitate further progress in alloy development.

References

[1] A. Stalmann, W. Sebastian, H. Friedrich, S. Schumann, K. Dröder, Advanced Engineering Materials 3 (2001) 969.

[2] F. Froes, D. Eliezer, E. Aghion, JOM Journal of the Minerals, Metals and Materials Society 50 (1998) 30–34.

[3] A. Luo, JOM Journal of the Minerals, Metals and Materials Society 54 (2002) 42–48.

[4] G. Hanko, H. Antrekowitsch, P. Ebner, JOM Journal of the Minerals, Metals and Materials Society 54 (2002) 51–54.

[5] A. Gesing, R. Wolanski, JOM Journal of the Minerals, Metals and Materials Society 53 (2001) 21–23.

[6] M. Easton, A. Beer, M. Barnett, C. Davies, G. Dunlop, Y. Durandet, S. Blacket, T. Hilditch, P. Beggs, JOM 60 (2008) 57–62.

[7] C.H. Caceres, Metallurgical and Materials Transactions A 38 (2007) 1649–1662.

[8] B. Mordike, T. Ebert, Materials Science and Engineering A 302 (2001) 37–45.

[9] D. Eliezer, E. Aghion, F. Froes, Advanced Performance Materials 5 (1998) 201–212.

[10] M.K. Kulekci, The International Journal of Advanced Manufacturing Technology 39 (2007) 851–865.

[11] M. Sakamoto, S. Akiyama, K. Ogi, Journal of Materials Science Letters 16 (1997) 1048–1050.

[12] N.R. Kumar, J. Blandin, M. Suery, E. Grosjean, Scripta Materialia 49 (2003) 225–230.

[13] C. Bettles, M. Gibson, JOM Journal of the Minerals, Metals and Materials Society 57 (2005) 46–49.

[14] J. Hirsch, T. Al-Samman, Acta Materialia 61 (2013) 818–843.

[15] S. Celotto, Acta Materialia 48 (2000) 1775–1787.

[16] J. Clark, Acta Metallurgica 16 (1968) 141–152.

[17] C.R. Hutchinson, J.F. Nie, S. Gorsse, Metallurgical and Materials Transactions A 36 (2005) 2093–2105.

[18] J. Buha, Materials Science and Engineering: A 492 (2008) 11–19.

[19] G. Mima, Y. Tanaka, Trans. Jpn. Inst. Met. 12 (1971) 76–81.

[20] J. Clark, Acta Metallurgica 13 (1965) 1281–1289.

[21] J.-F. Nie, Metallurgical and Materials Transactions A 43 (2012) 3891–3939.

[22] M. Yamasaki, M. Sasaki, M. Nishijima, K. Hiraga, Y. Kawamura, Acta Materialia 55 (2007) 6798–6805.

[23] J. Nie, K. Ohishi, X. Gao, K. Hono, Acta Materialia 56 (2008) 6061–6076.

[24] C. Antion, P. Donnadieu, F. Perrard, A. Deschamps, C. Tassin, A. Pisch, Acta Materialia 51 (2003) 5335–5348.

[25] T. Bhattacharjee, C.L. Mendis, T.T. Sasaki, T. Ohkubo, K. Hono, Scripta Materialia 67 (2012) 967–970.

[26] S. Ringer, K. Hono, I. Polmear, Applied Surface Science 94-95 (1996) 253–260.

[27] S. Ringer, K. Hono, I. Polmear, T. Sakurai, Acta Materialia 44 (1996) 1883–1898.

[28] S. Esmaeili, D. Lloyd, W. Poole, Acta Materialia 51 (2003) 3467–3481.

[29] S. Esmaeili, D.J. Lloyd, W.J. Poole, Acta Materialia 51 (2003) 2243–2257.

[30] S. Esmaeili, X. Wang, D.J. Lloyd, W.J. Poole, Metallurgical and Materials Transactions A 34 (2003) 751–763.

[31] X. Wang, J.D. Embury, W.J. Poole, S. Esmaeili, D.J. Lloyd, Metallurgical and Materials Transactions A 34 (2003) 2913–2924.

[32] W.F. Miao, D.E. Laughlin, Metallurgical and Materials Transactions A 31 (2000) 361–371.

[33] D. Dumont, a Deschamps, Y. Brechet, Materials Science and Engineering A 356 (2003) 326–336.

[34] A. Deschamps, F. Livet, Y. Brechet, Acta Materialia 47 (1998) 281–292.

[35] P. Sepehrband, S. Esmaeili, Materials Science and Engineering: A 487 (2008) 309–315.

[36] W.J. Poole, J. a. Sæter, S. Skjervold, G. Waterloo, Metallurgical and Materials Transactions A 31 (2000) 2327–2338.

[37] J. Buha, Materials Science and Engineering: A 491 (2008) 70–79.

[38] C.L. Mendis, C.J. Bettles, M. a. Gibson, S. Gorsse, C.R. Hutchinson, Philosophical Magazine Letters 86 (2006) 443–456.

[39] J. Buha, Journal of Materials Science 43 (2007) 1220–1227.

[40] T. Bhattacharjee, C.L. Mendis, K. Oh-ishi, T. Ohkubo, K. Hono, Materials Science and Engineering: A (2013).

[41] C. Bettles, M.A. Gibson, K. Venkatesan, Scripta Materialia 51 (2004) 193–197.

[42] X. Gao, J. Nie, Scripta Materialia 56 (2007) 645–648.

[43] C. Mendis, K. Ohishi, Y. Kawamura, T. Honma, S. Kamado, K. Hono, Acta Materialia 57 (2009) 749–760.

[44] J. Geng, X. Gao, X.Y. Fang, J.F. Nie, Scripta Materialia 64 (2011) 506–509.

[45] J. Buha, Materials Science and Engineering: A 492 (2008) 293–299.

[46] J. Buha, T. Ohkubo, Metallurgical and Materials Transactions A 39 (2008) 2259–2273.

[47] J. Buha, Materials Science and Engineering: A 489 (2008) 127–137.

[48] H.M. Zhu, G. Sha, J.W. Liu, C.L. Wu, C.P. Luo, Z.W. Liu, R.K. Zheng, S.P. Ringer, Journal of Alloys and Compounds 509 (2011) 3526–3531.

[49] J. Buha, Journal of Materials Science 43 (2007) 1220–1227.

[50] J. Buha, Journal of Alloys and Compounds 472 (2009) 171–177.

[51] J. Buha, Acta Materialia 56 (2008) 3533–3542.

[52] J.C. Oh, T. Ohkubo, T. Mukai, K. Hono, Scripta Materialia 53 (2005) 675–679.

[53] K. Oh-ishi, R. Watanabe, C.L. Mendis, K. Hono, Materials Science and Engineering: A 526 (2009) 177–184.

[54] X. Gao, S. Zhu, B. Muddle, J. Nie, Scripta Materialia 53 (2005) 1321–1326.

[55] A.A. Luo, B.R. Powell, M.P. Balogh, Metallurgical and Materials Transactions A 33 (2002) 567–574.

[56] B. You, W. Park, I. Chung, Scripta Materialia 42 (2000) 1089–1094.

[57] H. Du, Z. Wei, X. Liu, E. Zhang, Materials Chemistry and Physics 125 (2011) 568–575.

[58] Y. Wan, G. Xiong, H. Luo, F. He, Y. Huang, X. Zhou, Materials & Design 29 (2008) 2034–2037.

[59] N. Stanford, Materials Science and Engineering: A 528 (2010) 314–322.

[60] F.O. Riemelmoser, M. Kühlein, H. Kilian, M. Kettner, A.C. Hänzi, P.J. Uggowitzer, Advanced Engineering Materials 9 (2007) 799–802.

[61] S. Agnew, O. Duygulu, International Journal of Plasticity 21 (2005) 1161–1193.

[62] J. Koike, Metallurgical and Materials Transactions A 36 (2005) 1689–1696.

[63] G.I. Taylor, Journal of the Institute of Metals 62 (1938) 307–338.

[64] M. Barnett, Materials Science and Engineering: A 464 (2007) 1–7.

[65] M. Barnett, Materials Science and Engineering: A 464 (2007) 8–16.

[66] Y. Chino, X. Huang, K. Suzuki, K. Sassa, M. Mabuchi, Materials Science and Engineering: A 528 (2010) 566–572.

[67] F. Humphreys, M. Hatherly, Recrystallization and Related Annealing Phenomena, 2nd ed., Pergamon Press, 2004.

[68] N. Stanford, Materials Science and Engineering: A 565 (2013) 469–475.

[69] K. Hantzsche, J. Bohlen, J. Wendt, K. Kainer, S. Yi, Scripta Materialia (2010).

[70] N. Stanford, Materials Science and Engineering: A 527 (2010) 2669–2677.

[71] J.P. Hadorn, K. Hantzsche, S. Yi, J. Bohlen, D. Letzig, J. Wollmershauser, S.R. Agnew, Metallurgical and Materials Transactions A 43A (2012) 1347–1362.

[72] N. Stanford, D. Atwell, a. Beer, C. Davies, M.R. Barnett, Scripta Materialia 59 (2008) 772–775.

[73] A.A. Luo, R.K. Mishra, A.K. Sachdev, Scripta Materialia 64 (2011) 410–413.

[74] R. Mishra, A. Gupta, P. Rao, A. Sachdev, A. Kumar, A. Luo, Scripta Materialia 59 (2008) 562–565.

[75] T. Gladman, Materials Science and Technology 15 (1999) 30–36.

[76] A.J. Ardell, Metallurgical Transactions A 16A (1985) 2131–2165.

[77] E. Nembach, Particle Strengthening of Metals and Alloys, John Wiley & Sons, Inc., New York, 1997.

[78] V. Gerold, H. Haberkorn, Physica Status Solidi (b) 16 (1966) 675–684.

[79] D.N. Seidman, E.A. Marquis, D.C. Dunand, Acta Materialia 50 (2002) 4021–4035.

[80] E. Sjolander, S. Seifeddine, I.L. Svensson, International Journal of Cast Metals Research 24 (2011) 338–346.

[81] J. Nie, Scripta Materialia 48 (2003) 1009–1015.

[82] J.D. Robson, N. Stanford, M.R. Barnett, Metallurgical and Materials Transactions A 44 (2013) 2984–2995.

[83] S. Agnew, D. Brown, C. Tome, Acta Materialia 54 (2006) 4841–4852.

[84] S.R. Agnew, R.P. Mulay, F.J. Polesak, C. a. Calhoun, J.J. Bhattacharyya, B. Clausen, Acta Materialia 61 (2013) 3769–3780.

[85] M.A. Gharghouri, G.C. Weatherly, J.D. Embury, Philosophical Magazine A 78 (1998) 1137–1149.

[86] J.D. Robson, N. Stanford, M.R. Barnett, Acta Materialia 59 (2011) 1945–1956.

[87] N. Stanford, M.R. Barnett, Materials Science and Engineering: A 516 (2009) 226–234.

[88] N. Stanford, J. Geng, Y.B. Chun, C.H.J. Davies, J.F. Nie, M.R. Barnett, Acta Materialia 60 (2012) 218–228.

[89] J.D. Robson, N. Stanford, M.R. Barnett, Scripta Materialia 63 (2010) 823–826.

[90] G. Mima, Y. Tanaka, Trans. Jpn. Inst. Met. 12 (1971) 71–75.

[91] J. Chun, J. Byrne, Journal of Materials Science 4 (1969) 861–872.

[92] C.L. Mendis, K. Oh-ishi, K. Hono, Materials Science and Engineering: A 527 (2010) 973–980.

[93] J. Rosalie, H. Somekawa, A. Singh, T. Mukai, Philosophical Magazine 90 (2010) 3355–3374.

[94] J. Jain, P. Cizek, W.J. Poole, M.R. Barnett, Acta Materialia (2013).

[95] J.F. Nie, B.C. Muddle, Scripta Materialia 37 (1997) 1475–81.

[96] Y. Ortega, M.A. Monge, R. Pareja, Journal of Alloys and Compounds 463 (2008) 62–66.

[97] D.H. Ping, K. Hono, J.F. Nie, Scripta Materialia 48 (2003) 1017–1022.

[98] G. Levi, S. Avraham, a Zilberov, M. Bamberger, Acta Materialia 54 (2006) 523–530.

[99] P.M. Jardim, G. Solórzano, J.B.V. Sande, Materials Science and Engineering: A 381 (2004) 196–205.

[100] P.M. Jardim, G. Solórzano, J.B. Vander Sande, Microscopy and Microanalysis 8 (2002) 487–96.

[101] C. Mendis, K. Ohishi, Y. Kawamura, T. Honma, S. Kamado, K. Hono, Acta Materialia 57 (2009) 749–760.

[102] J.H. Li, G. Sha, T.Y. Wang, W.Q. Jie, S.P. Ringer, Materials Science and Engineering: A 534 (2012) 1–6.

[103] L.Y. Wei, G.L. Dunlop, H. Westengen, Metallurgical and Materials Transactions A 26 (1995) 1705–1716.

[104] M. Nishijima, K. Hiraga, M. Yamasaki, Y. Kawamura, Materials Transactions 48 (2007) 476–480.

[105] L. Gao, A.A. Luo, Materials Science and Engineering: A 560 (2013) 492–499.

[106] E.A. Ball, P.B. Prangnell, Scripta Metallurgica et Materialia 31 (1994) 111–116.

[107] A. Sadeghi, M. Hoseini, M. Pekguleryuz, Materials Science and Engineering: A 528 (2011) 3096–3104.

[108] H. Yu, Y.M. Kim, B.S. You, H.S. Yu, S.H. Park, Materials Science and Engineering: A 559 (2013) 798–807.

[109] J.D. Robson, D.T. Henry, B. Davis, Acta Materialia 57 (2009) 2739–2747.

[110] J.P. Hadorn, K. Hantzsche, S. Yi, J. Bohlen, D. Letzig, S.R. Agnew, Metallurgical and Materials Transactions A 43A (2012) 1363–1375.

[111] N. Stanford, M. Barnett, Materials Science and Engineering: A 496 (2008) 399–408.

[112] S. Agnew, M. Yoo, C. Tome, Acta Materialia 49 (2001) 4277–4289.

[113] S. Sandlöbes, S. Zaefferer, I. Schestakow, S. Yi, R. Gonzalez-Martinez, Acta Materialia 59 (2011) 429–439.

[114] N. Stanford, G. Sha, J.H. Xia, S.P. Ringer, M.R. Barnett, Scripta Materialia 65 (2011) 919–921.

[115] N. Stanford, I. Sabirov, G. Sha, a. La Fontaine, S.P. Ringer, M.R. Barnett, Metallurgical and Materials Transactions A 41 (2010) 734–743.

[116] R. Cottam, J. Robson, G. Lorimer, B. Davis, Materials Science and Engineering: A 485 (2008) 375–382.

[117] L. Mackenzie, M. Pekguleryuz, Scripta Materialia 59 (2008) 665–668.

[118] J. Bohlen, M.R. Nürnberg, J.W. Senn, D. Letzig, S.R. Agnew, Acta Materialia 55 (2007) 2101–2112.

[119] M. Sanjari, S.F. Farzadfar, T. Sakai, H. Utsunomiya, E. Essadiqi, I.-H. Jung, S. Yue, Materials Science and Engineering: A 561 (2013) 191–202.

[120] S.H. Park, H. Yu, J.H. Bae, C.D. Yim, B.S. You, Journal of Alloys and Compounds 545 (2012) 139–143.

[121] B. Zhang, Y. Wang, L. Geng, C. Lu, Materials Science and Engineering: A 539 (2012) 56–60.

[122] T.V. Padfield, in:, ASM Handbook Vol 9, ASM International, 2004, pp. 801–815.

[123] M. Mendelson, Journal of the American Ceramic Society 52 (1969) 443–446.

[124] M.K. Miller, Atom Probe Tomography: Analysis at the Atomic Level, Kluwer Academic/Plenum Publishers, New York, 2000.

[125] B. Gault, M.P. Moody, J.M. Cairney, S.P. Ringer, Atom Probe Microscopy, Springer Science, New York, 2012.

[126] J.H. Li, G. Sha, W.Q. Jie, S.P. Ringer, Materials Science and Engineering: A 538 (2012) 272–280.

[127] www.factsage.com, FactSage 6.3 (2012).

[128] D. Porter, K. Easterling, Phase Transformations in Metals and Alloys, 2nd ed., Taylor and Francis Ltd, Boca Raton, FL, 1992.

[129] A. a. Luo, B.R. Powell, M.P. Balogh, Metallurgical and Materials Transactions A 33 (2002) 567–574.

[130] Z. Li, X. Gu, S. Lou, Y. Zheng, Biomaterials 29 (2008) 1329–44.

[131] N.T. Kirkland, N. Birbilis, J. Walker, T. Woodfield, G.J. Dias, M.P. Staiger, Journal of Biomedical Materials Research. Part B, Applied Biomaterials 95 (2010) 91–100.

[132] V.Y. Gertsman, Unpublished Results, 2008.

[133] C. Mendis, K. Ohishi, K. Hono, Scripta Materialia 57 (2007) 485–488.

[134] J. Embury, R. Nicholson, Acta Metallurgica 13 (1965) 403–417.

[135] R. Wilson, P. Partridge, Acta Metallurgica 13 (1965) 1321–1327.

[136] R.W. Siegel, Journal of Nuclear Materials 69-70 (1978) 117–146.

[137] J. Wert, Acta Metallurgica 28 (1980) 1361–1373.

[138] R.K.W. Marceau, G. Sha, R.N. Lumley, S.P. Ringer, Acta Materialia 58 (2010) 1795–1805.

[139] S. Esmaeili, D. Vaumousse, M.W. Zandbergen, W.J. Poole, a. Cerezo, D.J. Lloyd, Philosophical Magazine 87 (2007) 3797–3816.

[140] R.D. Doherty, in:, R.W. Cahn, P. Haasen (Eds.), Physical Metallurgy (Fourth Edition), North-holland, Amsterdam, 1996, pp. 1363–1505.

[141] D. Shin, C. Wolverton, Acta Materialia 58 (2010) 531–540.

[142] J.E. Saal, C. Wolverton, Acta Materialia 60 (2012) 5151–5159.

[143] J. Silcock, Philosophical Magazine 4 (1959) 1187–1194.

[144] H. Kimura, R. Hasiguti, Acta Metallurgica 7 (1961) 1076–1078.

[145] S.P. Ringer, K. Hono, T. Sakurai, Metallurgical and Materials Transactions A 26A (1995) 2207–2217.

[146] B. Klobes, O. Balarisi, M. Liu, T.E.M. Staab, K. Maier, Acta Materialia 58 (2010) 6379–6384.

[147] K. Hono, C.L. Mendis, T.T. Sasaki, K. Oh-ishi, Scripta Materialia 63 (2010) 710–715.

[148] B. Langelier, S. Esmaeili, in:, Magnesium Technology 2010, TMS (The Minerals, Metals & Materials Society), 2010, pp. 505–509.

[149] B. Langelier, X. Wang, S. Esmaeili, Materials Science and Engineering: A 538 (2012) 246–251.

[150] S. Celotto, Acta Materialia 48 (2000) 1775–1787.

[151] L. Pauling, Journal of the American Chemical Society 69 (1947) 542–553.

[152] K.Y. Zheng, J. Dong, X.Q. Zeng, W.J. Ding, Materials Characterization 59 (2008) 857–862.

[153] A.K. Vasudevan, R.D. Doherty, Acta Metallurgica 35 (1987) 1193–1219.

[154] J. Cahn, Acta Metallurgica 10 (1962) 789–798.

[155] K. Grönhagen, J. Ågren, Acta Materialia 55 (2007) 955–960.

[156] B. Langelier, P. Donnadieu, S. Esmaeili, in:, W.J. Poole, K.U. Kainer (Eds.), 9th International Conference on Magnesium Alloys and Their Applications, Vancouver, BC, 2012, pp. 485–491.

[157] B.W. Krakauer, D.N. Seidman, Physical Review. B, Condensed Matter 48 (1993) 6724–6727.

[158] D.N. Seidman, B.W. Krakauer, D. Udler, J. Phys. Chem. Solids 55 (1994) 1035–1057.

[159] B. Gault, M.P. Moody, F. de Geuser, G. Tsafnat, A. La Fontaine, L.T. Stephenson, D. Haley, S.P. Ringer, Journal of Applied Physics 105 (2009) 034913.

[160] S.C. Jha, T.H. Sanders, M.A. Dayananda, Acta Metallurgica 35 (1987) 473–482.

[161] G. Sha, L. Yao, X. Liao, S.P. Ringer, Z. Chao Duan, T.G. Langdon, Ultramicroscopy 111 (2011) 500–5.

[162] T.W. Heo, S. Bhattacharyya, L.-Q. Chen, Acta Materialia 59 (2011) 7800–7815.

[163] R.K.W. Marceau, G. Sha, R. Ferragut, a. Dupasquier, S.P. Ringer, Acta Materialia 58 (2010) 4923–4939.

[164] V. Fallah, J. Stolle, N. Ofori-Opoku, S. Esmaeili, N. Provatas, Physical Review B 86 (2012) 134112.

[165] V. Fallah, N. Ofori-Opoku, J. Stolle, N. Provatas, S. Esmaeili, Acta Materialia 61 (2013) 3653–3666.

[166] T. Ogura, S. Hirosawa, A. Cerezo, T. Sato, Acta Materialia 58 (2010) 5714–5723.

[167] M.R. Barnett, A. Sullivan, N. Stanford, N. Ross, A. Beer, Scripta Materialia 63 (2010) 721–724.

[168] S. Sandlöbes, M. Friák, S. Zaefferer, a. Dick, S. Yi, D. Letzig, Z. Pei, L.-F. Zhu, J. Neugebauer, D. Raabe, Acta Materialia 60 (2012) 3011–3021.

[169] N. Stanford, M. Barnett, Scripta Materialia 58 (2008) 179–182.

[170] T. Laser, C. Hartig, M.R. Nürnberg, D. Letzig, R. Bormann, Acta Materialia 56 (2008) 2791–2798.

[171] C.H. Caceres, G.E. Mann, J.R. Griffiths, Metallurgical and Materials Transactions A 42 (2011) 1950–1959.

[172] A.H. Blake, C.H. Cáceres, Materials Science and Engineering: A 483-484 (2008) 161–163.

[173] J. Wei, J. Chen, H. Yan, B. Su, X. Pan, Journal of Alloys and Compounds 548 (2013) 52–59.

[174] D.-W. Kim, B.-C. Suh, M.-S. Shim, J.H. Bae, D.H. Kim, N.J. Kim, Metallurgical and Materials Transactions A (2013).

[175] C.L. Mendis, K. Oh-Ishi, K. Hono, Metallurgical and Materials Transactions A (2012) 2–11.

[176] N. Stanford, M.R. Barnett, International Journal of Plasticity (2013) 1–17.

[177] J. Koike, T. Kobayashi, T. Mukai, H. Watanabe, M. Suzuki, K. Maruyama, K. Higashi, Acta Materialia 51 (2003) 2055–2065.